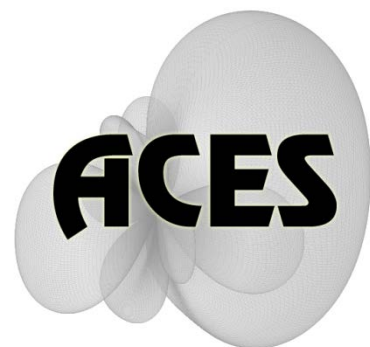


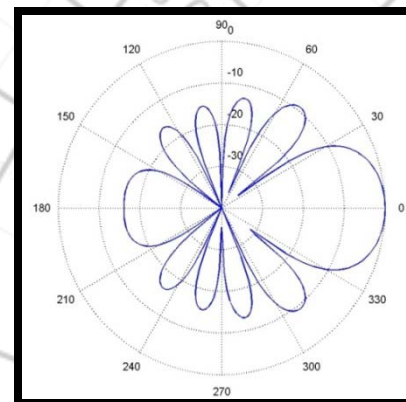
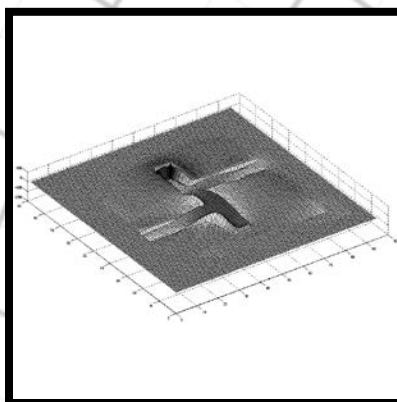
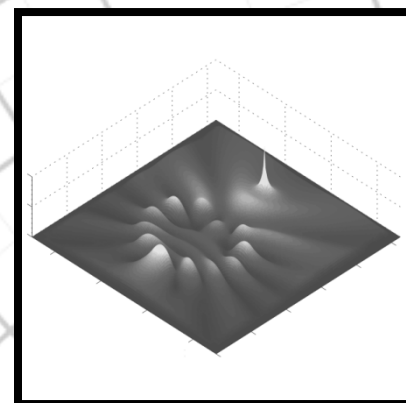
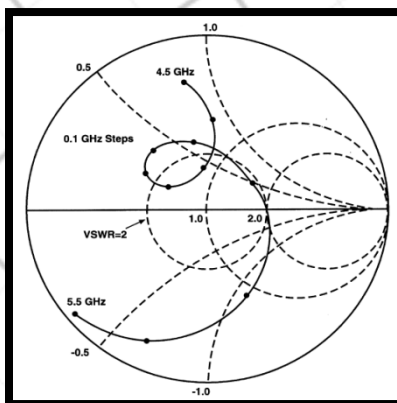
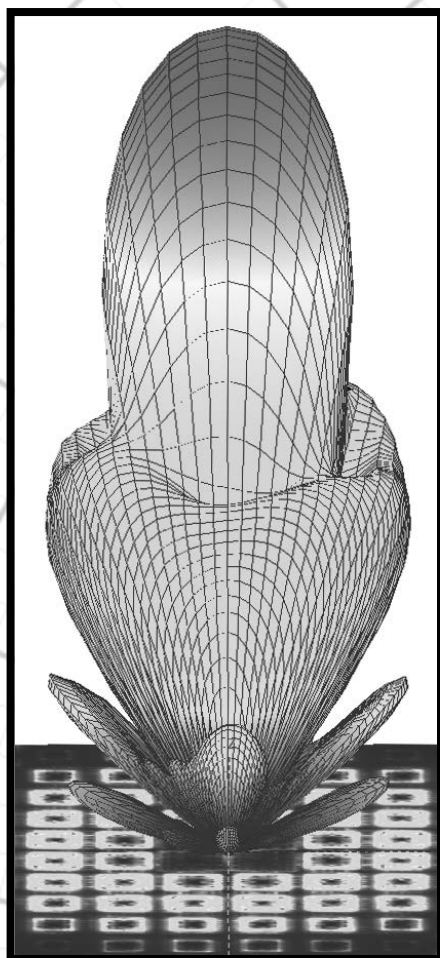
Applied Computational Electromagnetics Society

Journal



May 2012

Vol. 27 No. 5



ISSN 1054-4887

GENERAL PURPOSE AND SCOPE: The Applied Computational Electromagnetics Society (*ACES*) Journal hereinafter known as the *ACES Journal* is devoted to the exchange of information in computational electromagnetics, to the advancement of the state-of-the art, and the promotion of related technical activities. The primary objective of the information exchange is to inform the scientific community on the developments of new computational electromagnetics tools and their use in electrical engineering, physics, or related areas. The technical activities promoted by this publication include code validation, performance analysis, and input/output standardization; code or technique optimization and error minimization; innovations in solution technique or in data input/output; identification of new applications for electromagnetics modeling codes and techniques; integration of computational electromagnetics techniques with new computer architectures; and correlation of computational parameters with physical mechanisms.

SUBMISSIONS: The *ACES Journal* welcomes original, previously unpublished papers, relating to applied computational electromagnetics. Typical papers will represent the computational electromagnetics aspects of research in electrical engineering, physics, or related disciplines. However, papers which represent research in applied computational electromagnetics itself are equally acceptable.

Manuscripts are to be submitted through the upload system of *ACES* web site <http://aces.ee.olemiss.edu> See "Information for Authors" on inside of back cover and at *ACES* web site. For additional information contact the Editor-in-Chief:

Dr. Atef Elsherbeni
Department of Electrical Engineering
The University of Mississippi
University, MS 386377 USA
Phone: 662-915-5382
Email: atef@olemiss.edu

SUBSCRIPTIONS: All members of the Applied Computational Electromagnetics Society are entitled to access and download the *ACES Journal* any published journal article available at <http://aces.ee.olemiss.edu>. Printed issues of the *ACES Journal* are delivered to institutional members. Each author of published papers receives a printed issue of the *ACES Journal* in which the paper is published.

Back issues, when available, are \$50 each. Subscription to *ACES* is through the web site. Orders for back issues of the *ACES Journal* and change of address requests should be sent directly to *ACES* office at:

Department of Electrical Engineering
The University of Mississippi
University, MS 386377 USA
Phone: 662-915-7231
Email: aglisson@olemiss.edu

Allow four weeks advance notice for change of address. Claims for missing issues will not be honored because of insufficient notice, or address change, or loss in the mail unless the *ACES* office is notified within 60 days for USA and Canadian subscribers, or 90 days for subscribers in other countries, from the last day of the month of publication. For information regarding reprints of individual papers or other materials, see "Information for Authors".

LIABILITY. Neither *ACES*, nor the *ACES Journal* editors, are responsible for any consequence of misinformation or claims, express or implied, in any published material in an *ACES Journal* issue. This also applies to advertising, for which only camera-ready copies are accepted. Authors are responsible for information contained in their papers. If any material submitted for publication includes material which has already been published elsewhere, it is the author's responsibility to obtain written permission to reproduce such material.

**APPLIED
COMPUTATIONAL
ELECTROMAGNETICS
SOCIETY
JOURNAL**

May 2012
Vol. 27 No. 5
ISSN 1054-4887

The ACES Journal is abstracted in INSPEC, in Engineering Index, DTIC, Science Citation Index Expanded, the Research Alert, and to Current Contents/Engineering, Computing & Technology.

The illustrations on the front cover have been obtained from the research groups at the Department of Electrical Engineering, The University of Mississippi.

THE APPLIED COMPUTATIONAL ELECTROMAGNETICS SOCIETY

<http://aces.ee.olemiss.edu>

EDITOR-IN-CHIEF

Atef Elsherbeni

University of Mississippi, EE Dept.
University, MS 38677, USA

ASSOCIATE EDITORS-IN-CHIEF

Sami Barmada

University of Pisa, EE Dept.
Pisa, Italy, 56126

Fan Yang

University of Mississippi, EE Dept.
University, MS 38677, USA

Mohamed Bakr

McMaster University, ECE Dept.
Hamilton, ON, L8S 4K1, Canada

Yasushi Kanai

Niigata Inst. of Technology
Kashiwazaki, Japan

Mohammed Hadi

Kuwait University, EE Dept.
Safat, Kuwait

Mohamed Abouzahra

MIT Lincoln Laboratory
Lexington, MA, USA

EDITORIAL ASSISTANTS

Matthew J. Inman

University of Mississippi, EE Dept.
University, MS 38677, USA

Anne Graham

University of Mississippi, EE Dept.
University, MS 38677, USA

EMERITUS EDITORS-IN-CHIEF

Duncan C. Baker

EE Dept. U. of Pretoria
0002 Pretoria, South Africa

Allen Glisson

University of Mississippi, EE Dept.
University, MS 38677, USA

David E. Stein

USAF Scientific Advisory Board
Washington, DC 20330, USA

Robert M. Bevensee

Box 812
Alamo, CA 94507-0516, USA

Ahmed Kishk

University of Mississippi, EE Dept.
University, MS 38677, USA

EMERITUS ASSOCIATE EDITORS-IN-CHIEF

Alexander Yakovlev

University of Mississippi, EE Dept.
University, MS 38677, USA

Erdem Topsakal

Mississippi State University, EE Dept.
Mississippi State, MS 39762, USA

EMERITUS EDITORIAL ASSISTANTS

Khaled ElMaghoub

University of Mississippi, EE Dept.
University, MS 38677, USA

Mohamed Al Sharkawy

Arab Academy for Science and
Technology, ECE Dept.
Alexandria, Egypt

Christina Bonnington

University of Mississippi, EE Dept.
University, MS 38677, USA

MAY 2012 REVIEWERS

**Ahmed Abdelrahman
Shirook Ali
Saad Alhossin
Abdul Ali Babar
Mohamed Bakr
Sami Barmada
Toni Bjorninen
Deb Chatterjee
Alistar Duffy
Mohammed Hadi
Amir Hajiaboli**

**Bassem Henien
Ashraf Islam
Yasushi Kanai
Nikolaos Kantartzis
Fadi Khalil
Zhiwei Liu
Francisco Medina
Ivor Morrow
Abbas Omar
Fan Yang
Theodoros Zygidis**

THE APPLIED COMPUTATIONAL ELECTROMAGNETICS SOCIETY
JOURNAL

Vol. 27 No. 5

May 2012

TABLE OF CONTENTS

“Comparative Study of Analytical and Numerical Techniques in Modeling Electromagnetic Scattering from Single and Double Knife-Edge in 2D Ground Wave Propagation Problems” O. Ozgun and L. Sevgi.....	376
“Numerical Prepackaging with PMC Lid - Efficient and Simple Design Procedure for Microstrip Circuits Including the Packaging” A. A. Kishk, A. U. Zaman, and P. S. Kildal.....	389
“Generalized Formulation for the Scattering from a Ferromagnetic Microwire” A. M. Attiya and M. A. Alkanhal.....	399
“An Equivalent Dipole-Moment Method Based Multilevel Fast Multipole Algorithm for Dielectric Objects” X. Chen, C. Gu, J. Ding, X. Deng, Z. Niu, and Z. Li.....	408
“Improved Weakly Conditionally Stable Finite-Difference Time-Domain Method” J. Chen.....	413
“Dual Band-Notch Small Square Monopole Antenna with Enhanced Bandwidth Characteristics for UWB Applications” M. Ojaroudi, N. Ojaroudi, and Y. Ebazadeh.....	420
“Optimal Design of an Ultra-Wideband Antenna with the Irregular Shape on Radiator using Particle Swarm Optimization” W. C. Weng.....	427
“A Novel Harmonic Suppression Antenna with Both Compact Size and Wide Bandwidth” Z. L. Zhou, L. Li, J. S. Hong, and B. Z. Wang.....	435
“A Novel Circular Disc Monopole Antenna for Dual-Band WLAN Applications” B. Li, J. S. Hong, and B. Z. Wang.....	441
“Electric Field Distribution in a Biological Cell for Various Electrode Configurations-A Simulation Study M. O. Goni.....	449

Comparative Study of Analytical and Numerical Techniques in Modeling Electromagnetic Scattering from Single and Double Knife-Edge in 2D Ground Wave Propagation Problems

Ozlem Ozgun ¹, and Levent Sevgi ²

¹ TED University
Department of Electrical and Electronics Engineering, Ankara, Turkey
ozlem.ozgun@tedu.edu.tr

² Dogus University
Department of Electronics and Communications Engineering, 34722, Istanbul, Turkey
lsevgi@dogus.edu.tr

Abstract — This paper presents a comparative study of some analytical and numerical techniques in the solution of a classical problem of electromagnetic scattering from single and double knife edge above ground. The results of the analytical exact and asymptotic techniques (such as uniform theory of diffraction, parabolic equation diffraction method) are compared with the two-way split-step parabolic equation method (SSPE), through several numerical simulations. Salutary discussions on their capabilities and limitations are presented. Codes used in the simulations are provided in the end.

Index Terms — Diffraction, electromagnetic scattering, geometric optics (GO), ground wave propagation, two-way split-step parabolic equation method, uniform theory of diffraction (UTD).

I. INTRODUCTION

Electromagnetic ground wave propagation over the Earth's surface is affected by several scattering phenomena, such as reflection, refraction, and diffraction. Developing a rigorous method for understanding the effects of varying conditions on ground wave propagation is usually a challenging task because of the vast variability of the medium parameters and also the complexity of the surfaces and obstacles that re-direct the propagating energy. Initially, the prediction of the ground wave propagation problem has been

achieved by means of some analytical exact or analytical asymptotic techniques [1-17], which require the geometry to be represented as a member of a set of some canonical geometries. The exact techniques express the solution in the form of infinite series or integral and may serve as reference but might be poorly convergent at high frequencies when the dimensions of the objects are much larger than the wavelength. Asymptotic techniques have been widely used for decades to solve problems at high (usually optical) frequencies. These high-frequency asymptotic (HFA) approaches employ simplified models of electromagnetic wave reflection, refraction and diffraction such as geometric optics (GO), physical optics (PO), geometric theory of diffraction (GTD) [8-9], uniform theory of diffraction (UTD) [10-11], physical theory of diffraction (PTD) [12-13]. The GO model describes only the incident, reflected and refracted waves on the illuminated side of the scatterers. The GTD model is complementary to the GO model, in the sense that it overcomes some limitations of GO by including the diffraction mechanism. However, the GTD model exhibits singularities along the incident and reflection shadow boundaries (ISB and RSB). The uniform theory of diffraction (UTD) model achieves smooth wave behavior along these boundaries. This family (GO, GTD, UTD) is also known as ray tracing techniques in the literature. The PO

and PTD models, on the other hand, are based on induced currents on the surfaces of the scatterers. The PTD model supplements PO by introducing non-uniform ("fringe") edge currents to incorporate the effect of diffraction into the solution. In spite of simplicity, the asymptotic techniques suffer from two major drawbacks: (i) Solutions are available only for certain canonical objects, such as wedge (or knife-edge), cylinder. (ii) (Unless ray-shooting is not used) vertically-varying refractivity profiles in the troposphere cannot be handled.

With the advances in computers, some numerical techniques have been devised to solve the ground wave propagation problem involving complex geometries and inhomogeneous environments. Split-step parabolic equation (SSPE) method [18-22] has been widely used in propagation modeling because of its capability in modeling both horizontally- and vertically-varying atmospheric refraction (especially ducting) effects. It solves an initial-value problem starting from a source (or an antenna), and marching out in range by computing the field along the vertical direction at each range by means of step-by-step Fourier transformations. The classical SSPE method deals only with forward propagating waves, and thus, it is a one-way model that is valid in the paraxial region. Recently, a two-way SSPE algorithm has been introduced [23, 24] to incorporate the backward propagating waves into the one-way SSPE by utilizing an iterative forward-backward scheme for modeling multipath effects. This algorithm has been served for the public's use via a novel, MATLAB[®] based software tool (PETOOL) [25]. In spite of several advantages, the SSPE method takes the diffraction effects into account within the paraxial approximation, degrading the accuracy of the approach in deep-shadow regions where the diffracted fields dominate.

The organization of this paper is as follows: In Sec. II, analytical exact and asymptotic methods are briefly formulated. In Sec. III, fundamentals of the two-way SSPE are outlined. In Sec. IV, the techniques are compared through several numerical simulations. In the Appendix, the codes used in the simulations are presented.

Except Sec. II C, the time dependence of the form $\exp(-i\omega t)$ is assumed.

II. ANALYTICAL EXACT AND ASYMPTOTIC MODELS

This section discusses various analytical approaches, belonging to the family of ray-based techniques. The problem of interest is the 2D electromagnetic ground wave propagation where single or multiple knife-edges are located on a flat conducting surface and illuminated by a line-source (see Fig. 1). The problem of single or multiple knife-edge (or wedge in general) suspended in a homogeneous medium is one of the classical, canonical problems, and plays a fundamental role in the construction of the high-frequency asymptotic techniques. If the edges are located on a conducting surface, the image theory can be employed to account for the multiple reflections from the ground or edges. The total field is then obtained by the sum of the direct ray, the reflected rays emanating from image sources, and the diffracted rays from the tip of the edges, by also checking the line-of-sight (LOS) conditions between the source and the observation point. The beauty of this model is that it yields physical insight, and contributions of every ray item can be observed separately.

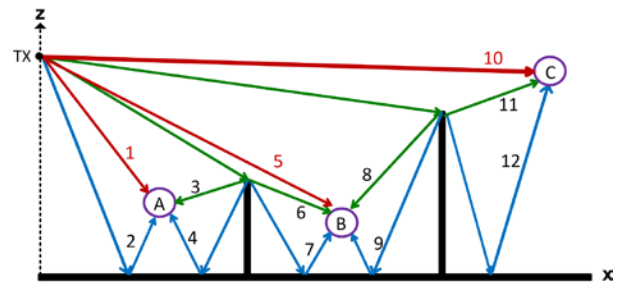


Fig. 1: Geometry of the problem, illustrating some possible ray contributions for different observation points (A, B, C). [Red: direct, Green: diffracted, Blue: reflected or diffracted/reflected].

The subsections below formulate various techniques to modeling of the diffracted field from the tip of a single wedge in the absence of ground (see Fig. 2). The more general problem in Fig. 1 involving multiple bouncing of the rays can be handled by a successive implementation of GO and diffraction algorithms depending on different LOS conditions (this is indeed just a coding issue). The wedge in Fig. 2 is illuminated by a cylindrically diverging line-source. The tip-to-source distance and the source angle are denoted

by r_0 and φ_0 , respectively; whereas the tip-to-observer distance and the observation angle are represented by r and φ , respectively. The wedge exterior angle α is set to 2π in the simulations to model the knife-edge. On the other hand, more realistic, hill-type obstacles may be modeled easily by setting $\alpha \neq 2\pi$. The wedge surface is assumed to be perfect electric conductor. As conventional in the diffraction theory, the polarization will be referred to as soft or hard polarizations, which are equivalent to horizontal or vertical polarizations, respectively.

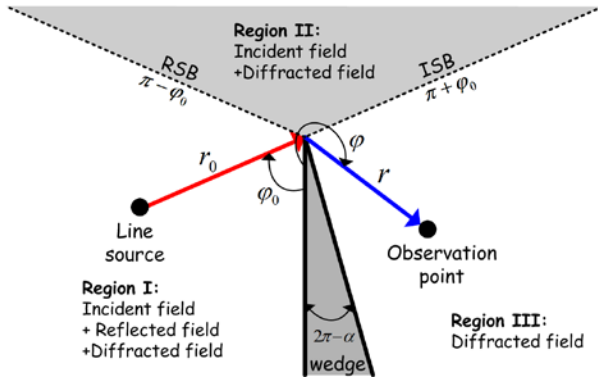


Fig. 2. Problem of scattering from a wedge.

A. Exact series model

Analytical exact solution of the problem in Fig. 2 can be obtained by using the separation of variables method, which reduces the 2D wave equation into two 1D wave equations; one in the angular domain, the other in the radial domain. Depending on the boundary conditions, the angular domain solutions are expressed in terms of sine or cosine functions, whereas the radial domain solutions are constructed by means of Bessel or Hankel functions. Bessel and Hankel functions are appropriate for $r \leq r_0$ and for $r > r_0$, respectively.

Assuming a line source of the form of $I_0\delta(r-r_0, \varphi-\varphi_0)$, the exact total field for soft and hard boundary conditions, respectively, are expressed in series as follows: [15]

$$u_s^t = \begin{cases} \frac{4\pi}{\alpha} \sum_{m=1}^{\infty} J_{\nu_m}(kr) H_{\nu_m}^{(1)}(kr_0) f_s(\varphi, \varphi_0) & \text{if } r \leq r_0 \\ \frac{4\pi}{\alpha} \sum_{m=1}^{\infty} J_{\nu_m}(kr_0) H_{\nu_m}^{(1)}(kr) f_s(\varphi, \varphi_0) & \text{if } r \geq r_0 \end{cases} \quad (1)$$

$$u_h^t = \begin{cases} \frac{4\pi}{\alpha} \sum_{m=0}^{\infty} \varepsilon_m J_{\nu_m}(kr) H_{\nu_m}^{(1)}(kr_0) f_h(\varphi, \varphi_0) & \text{if } r \leq r_0 \\ \frac{4\pi}{\alpha} \sum_{m=0}^{\infty} \varepsilon_m J_{\nu_m}(kr_0) H_{\nu_m}^{(1)}(kr) f_h(\varphi, \varphi_0) & \text{if } r \geq r_0 \end{cases} \quad (2)$$

Here, k is the wavenumber, $\nu_m = m\pi/\alpha$, $\varepsilon_m = 1/2$ if $m=0$ and $\varepsilon_m = 1$ otherwise; and $f_s = \sin(\nu_m\varphi_0)\sin(\nu_m\varphi)$, $f_h = \cos(\nu_m\varphi_0)\cos(\nu_m\varphi)$.

Since the total field is the sum of the diffracted field and the GO field (i.e., $u_{s,h}^t = u_{s,h}^d + u_{s,h}^{GO}$), the diffracted field $u_{s,h}^d$ can be obtained by subtracting the GO field from the total field. The GO field is the sum of the incident (direct) field and the reflected field emanating from the image source (i.e., $u_{s,h}^{GO} = u_{s,h}^{inc} + u_{s,h}^r$ where $u_{s,h}^r = u_{s,h}^{inc, image}$). The incident field is expressed in terms of Hankel function, i.e., $u_s^{inc} = H_0^{(1)}(kR)$, where R is the distance between the source (actual or image) and observation points (i.e., R_{actual} or R_{image}). Hence, the GO field can be expressed with respect to the LOS conditions, as follows:

$$u_{s,h}^{GO} = \varepsilon_1 H_0^{(1)}(kR_{actual}) \mp \varepsilon_2 H_0^{(1)}(kR_{image}), \quad (3)$$

where $(-)$ and $(+)$ are for soft and hard polarizations, respectively. Moreover,

$$\varepsilon_1 = \begin{cases} 1 & \text{for } \varphi \leq \pi + \varphi_0 \\ 0 & \text{for } \varphi > \pi + \varphi_0 \end{cases}, \quad (4)$$

$$\varepsilon_2 = \begin{cases} 1 & \text{for } \varphi \leq \pi - \varphi_0 \text{ (if } 0 \leq \varphi_0 \leq \alpha - \pi \text{)} \\ 0 & \text{for } \varphi > \pi - \varphi_0 \end{cases}, \quad (5)$$

$$\varepsilon_2 = \begin{cases} 1, & \text{for } 0 < \varphi < \pi - \varphi_0 \\ 0, & \text{for } \pi - \varphi_0 < \varphi < 2\alpha - \pi - \varphi_0 \text{ (if } \alpha - \pi \leq \varphi_0 \leq \pi \text{)} \\ 1, & \text{for } 2\alpha - \pi - \varphi_0 < \varphi < \alpha \end{cases} \quad (6)$$

Note that the case $0 \leq \varphi_0 \leq \alpha - \pi$ in (5) and $\alpha - \pi \leq \varphi_0 \leq \pi$ in (6) refer to Single-Side (only one face) and Double-Side illuminations, respectively.

Under the conditions where $kr_0 \gg 1$ and $kr \gg 1$, asymptotic forms of Hankel functions can be used. Hence, the diffracted field can be cast into the following form:

$$u_{s,h}^d = u_0 d_{s,h} \frac{e^{ikr}}{\sqrt{r}}, \quad (7)$$

where $u_0 = H_0^{(1)}(kr_0)$ is the incident field at the tip of the wedge, and $d_{s,h}$ is the *diffraction coefficient*.

Thus, (7) allows us to compute the diffraction coefficient approximately after the exact diffracted field is computed, i.e., $d_{s,h} = \sqrt{r} (u_{s,h}^d / u_0) e^{-ikr}$.

It is useful to note that the number of terms in the series expressions increases drastically as the frequency increases and/or the observation point moves away from the tip of the wedge. This might obviously place a bottleneck on the computation time during the numerical implementation.

B. Exact integral model

Analytical exact solution of the wedge diffraction problem can also be obtained by an integral representation presented by Bowman & Senior in a handbook [6]. The diffracted fields can be expressed as follows:

$$u_{s,h}^d = [V_d(-\pi - \varphi + \varphi_0) - V_d(\pi - \varphi + \varphi_0)] \mp [V_d(-\pi - \varphi - \varphi_0) - V_d(\pi - \varphi - \varphi_0)], \quad (8)$$

where (-) and (+) are for soft and hard polarizations, respectively. Here,

$$V_d(\beta) = \frac{1}{2\pi n} \int_0^\infty H_0^{(1)}[kR(i\kappa)] \frac{\sin(\beta/n)}{\cosh(\kappa/n) - \cos(\beta/n)} d\kappa \quad (9)$$

where $n = \alpha/\pi$ and $R(\eta) = \sqrt{r^2 + r_0^2 + 2rr_0 \cos(\eta)}$.

Note that the total fields can be determined by adding the GO fields to the diffracted fields in (8). Similarly, the diffracted field can be expressed in the form of (7), from which the diffraction coefficient is calculated. Away from the shadow boundaries, asymptotic form of the diffraction coefficient can be derived as follows:

$$d_{s,h}^{asympt} = \frac{\sin(\pi/n)}{n} [(\cos \frac{\pi}{n} - \cos \frac{\varphi - \varphi_0}{n})^{-1} \mp (\cos \frac{\pi}{n} - \cos \frac{\varphi + \varphi_0}{n})^{-1}] \frac{e^{i\pi/4}}{\sqrt{2\pi k}}, \quad (10)$$

where (-) and (+) are for soft and hard polarizations, respectively. Here, the complex exponential term $e^{i\pi/4}$ indicates that the wedge tip is the caustic of edge-diffracted rays. Note that the critical part of this representation is the numerical integration of the $V_d(\beta)$ integral in (9), which contains singularities on the complex β plane because of Hankel function and the denominator [26]. Since the direct numerical integration along positive real axis is very time consuming, a deformed contour can be used to accelerate the computations.

C. Uniform theory of diffraction (UTD) model

In this model, the diffracted field is also expressed in the same form in (7), except that $u_0 = H_0^{(2)}(kr_0)$ and $e^{i\pi/4}$ is replaced by $e^{-j\pi/4}$ due to the time dependence convention in UTD. The UTD diffraction coefficients are given as [10]:

$$d_{s,h} = \frac{-e^{-j\pi/4}}{2n\sqrt{2\pi k}} \{ [\cot\left(\frac{\pi - \xi^-}{2n}\right) F(kLg^+ \xi^-) + \cot\left(\frac{\pi + \xi^-}{2n}\right) F(kLg^- \xi^-)] \mp [\cot\left(\frac{\pi - \xi^+}{2n}\right) F(kLg^+ \xi^+) + \cot\left(\frac{\pi + \xi^+}{2n}\right) F(kLg^- \xi^+)] \}, \quad (11)$$

where (-) and (+) are for soft and hard polarizations, respectively. Furthermore, $\xi^+ = \varphi + \varphi_0$, $\xi^- = \varphi - \varphi_0$ and $F(X)$ is the Fresnel function given as follows:

$$F(X) = 2j\sqrt{X} e^{jX} \int_{\sqrt{X}}^\infty e^{-j\tau^2} d\tau, \quad (12)$$

and L , g^\pm are computed as follows:

$$L = \frac{rr_0}{r+r_0}, \quad g^\pm(\xi) = 2\cos^2\left(\frac{2n\pi N^\pm - \xi}{2}\right), \quad (13)$$

where $N^\pm = (\pm\pi + \xi)/2n\pi$ are the integers that most closely satisfy this expression.

Note that the cotangent functions in (11) possess singularities at the shadow boundaries, and hence, can be replaced by the following:

$$\cot\left(\frac{\pi \pm \beta}{2n}\right) F(kLg^\pm \xi) = n \left[\sqrt{2\pi kL} \operatorname{sgn}(\varepsilon) - 2kL\varepsilon e^{-j\pi/4} \right] e^{-j\pi/4}, \quad (14)$$

for small $\varepsilon \rightarrow 0$. Similarly, the total fields are obtained by adding the GO and the diffracted fields, according to the LOS conditions. Finally, note that the UTD diffraction coefficients are equivalent to (10) away from the shadow boundaries, by replacing $e^{i\pi/4}$ with $e^{-j\pi/4}$.

C. Parabolic equation (PE) model

The parabolic equation (PE) diffraction method provides a correct first-order approximation to the diffracted field in the case when $kr \gg 1$ and $kr_0 \gg 1$ [13]. Note that, in spite of the similarity of

name, this model is different from the split-step parabolic equation (SSPE) method, which is a numerical marching type algorithm described in Sec. III. The PE-based diffracted field can be determined as follows:

$$u_{s,h}^d = u_0 \sqrt{\frac{r_0}{r_0 + r}} W_{s,h}(k\rho, \varphi, \varphi_0) e^{ikr}, \quad \rho = \frac{rr_0}{r + r_0}, \quad (15)$$

where

$$W_{s,h}(k\rho, \varphi, \varphi_0) = w(k\rho, \varphi - \varphi_0) \mp w(k\rho, \varphi + \varphi_0), \quad (16)$$

where (-) and (+) are for soft and hard polarizations, respectively. Here,

$$w(k\rho, \psi) e^{ik\rho} = \frac{1}{\pi\sqrt{2}} e^{i(k\rho + \pi/4)} \int_{-\infty}^{\infty} e^{-k\rho s^2} \frac{\frac{1}{n} \frac{\sin \pi}{n}}{\cos \frac{\pi}{n} - \cos \frac{\eta(s) + \psi}{n}} ds, \quad (17)$$

which is equivalent to the following form:

$$\begin{aligned} w(k\rho, \psi) e^{ik\rho} &= \frac{1}{\pi\sqrt{2}} e^{i(k\rho + \pi/4)} \int_{-\infty}^{\infty} e^{-k\rho s^2} \left[\frac{1}{2n} \cot \frac{\eta(s) + \psi - \pi}{2n} \right. \\ &\quad \left. - \frac{1}{2} \csc \frac{\zeta(s) + \psi - \pi}{2} \sec \frac{\zeta(s)}{2} \right. \\ &\quad \left. - \frac{1}{2n} \cot \frac{\eta(s) + \psi + \pi}{2n} \right] ds \\ &\quad + e^{-ik\rho \cos \psi} \frac{e^{-i\pi/4}}{\sqrt{\pi}} \int_{\frac{\sqrt{2k\rho} \sin \frac{\psi - \pi}{2}}}{\frac{\sin \psi - \pi}{2}} e^{ix^2} dx \end{aligned} \quad (18)$$

where $\eta = \sqrt{2}s e^{-i\pi/4}$, $s = \sqrt{2} e^{-i\pi/4} \sin \zeta/2$ and $\zeta(s) = -i \ln(1 + is^2 + is\sqrt{s^2 - 2i})$. This form is convenient for numeric calculation and asymptotic evaluation [26]. In the vicinity of the saddle point ($|s| \ll 1$), the following approximations can be made:

$$\zeta(s) = s\sqrt{2} e^{-i\pi/4} + O(s^2) = \eta(s) + O(s^2), \quad (19a)$$

$$\sec \frac{\zeta(s)}{2} = 1 + O(s^2). \quad (19b)$$

Thus, the two first terms in the square brackets of (18), which are singular at the saddle point when $\psi = \varphi \pm \varphi_0 = \pi$, completely cancel each other and the standard saddle point technique can be applied to the integral over the variable s .

Finally, the diffraction coefficients are found as follows:

$$d_{s,h} = W(k\rho, \varphi, \varphi_0) \sqrt{\frac{rr_0}{r + r_0}}, \quad (20)$$

which reduces to (10) away from the shadow boundaries.

III. TWO-WAY SPLIT-STEP PARABOLIC EQUATION MODEL

The parabolic wave equation (PWE) is derived from the 2D Helmholtz wave equation by separating the rapidly varying phase term to obtain a reduced function varying slowly in range for propagating angles close to the paraxial (horizontal) direction. The PWE can be converted to an initial value problem and can be solved by a marching-type numerical algorithm. The Fourier split-step parabolic equation (SSPE) is a powerful algorithm which accepts the initial field at a reference range (e.g., at an antenna) and then advances in range by computing the field along longitudinal direction at each range step. The classical SSPE is known as one-way approach because it handles only the forward-propagating waves, and cannot account for the backscattered ones. The classical one-way SSPE determines the longitudinal field at range $x + \Delta x$ as follows [20]:

$$\begin{aligned} u(x + \Delta x, z) &= \exp\left[ik(n^2 - 1) \frac{\Delta x}{2} \right] \times \\ &\quad F^{-1} \left\{ \exp\left[-ip^2 \frac{\Delta x}{2k} \right] F\{u(x, z)\} \right\} \end{aligned} \quad (21)$$

where F denotes the Fourier Transform, $p = k_z$ is the transform variable (i.e., transverse wavenumber $p = k \sin \theta$ where θ is the propagation angle from the horizontal), and n is the refractive index. Eqn. (21) is valid for propagation angles up to 10° - 15° , and hence, it is known as narrow-angle SSPE. Long-range propagation can be accurately modeled with the narrow-angle SSPE because propagation angles encountered in such problems are usually less than a few degrees. However, short range propagation problems, as well as the problems involving multiple reflections and diffractions because of hills and valleys with steep slopes, can be modeled more accurately with the wide-angle SSPE, which is effective for propagation angles up to 40° - 45° [22, 25]. The wide-angle SSPE obtains the field at each range as follows:

$$\begin{aligned} u(x + \Delta x, z) &= \exp[ik(n-1)\Delta x] \times \\ &\quad F^{-1} \left\{ \exp\left[ik\Delta x \left(\sqrt{1 - \frac{p^2}{k^2}} - 1 \right) \right] F\{u(x, z)\} \right\} \end{aligned} \quad (22)$$

Although the one-way SSPE model is quite effective in modeling electromagnetic propagation above the Earth's irregular surface through inhomogeneous atmosphere, it suffers from the disability of handling backward-propagating waves. The forward waves might be sufficient for long-range propagation scenarios. However, the backward waves become significant in the presence of obstacles that re-direct the incoming wave, which renders a necessity of estimating the multipath effects accurately. Recently, a two-way SSPE algorithm was implemented in [23] to incorporate the backward-propagating waves into the solution, through a recursive forward-backward scheme to model the electromagnetic propagation over a staircase-approximated terrain (i.e., the terrain is modeled like a train of knife-edges). If the wave meets the terrain (or knife-edge), it is partially-reflected by imposing the appropriate boundary conditions on the terrain facet, and is marched out in the backward direction by reversing the paraxial direction in the PWE formulation. Note that the same form of (22) is used during the backward propagation. At each step where the wave hits the terrain, the wave is split into two components (forward and backward). Each wave component continues to march out in its own paraxial direction. The convergence of the algorithm is checked against a certain threshold criterion comparing the total fields at each iteration. The two-way SSPE algorithm was implemented in MATLAB and presented as a software tool (called PETOOL), which can be downloaded from [25].

IV. NUMERICAL SIMULATIONS

This section demonstrates the test results of the analytical and numerical techniques over different propagation scenarios. The first scenario involves a single knife-edge of height 150 m located at 3 km. The line-source is at 50 m height; the frequency is 300 MHz; and the polarization is soft. The 3D maps of the propagation factor¹ within the entire domain are plotted in Fig. 3. Note that the exact models are not included in this figure because they are extremely time-consuming.

A good agreement is observed among the results of the analytical techniques. When the two-

way SSPE is compared with the analytical techniques, a good conformity is obtained in the region before 3 km that is in the interference region, but a slight discrepancy is observed in the region after 3 km that is in the deep-shadow / diffraction region. This discrepancy might be due to ignoring some of the less contributing ray components, and/or due to the limitation of SSPE within the paraxial regions. It is also observed that artificial effects around the shadow boundaries are clearly apparent on the maps of the analytical methods. However, SSPE model provides smoother wave behavior around the transition regions.

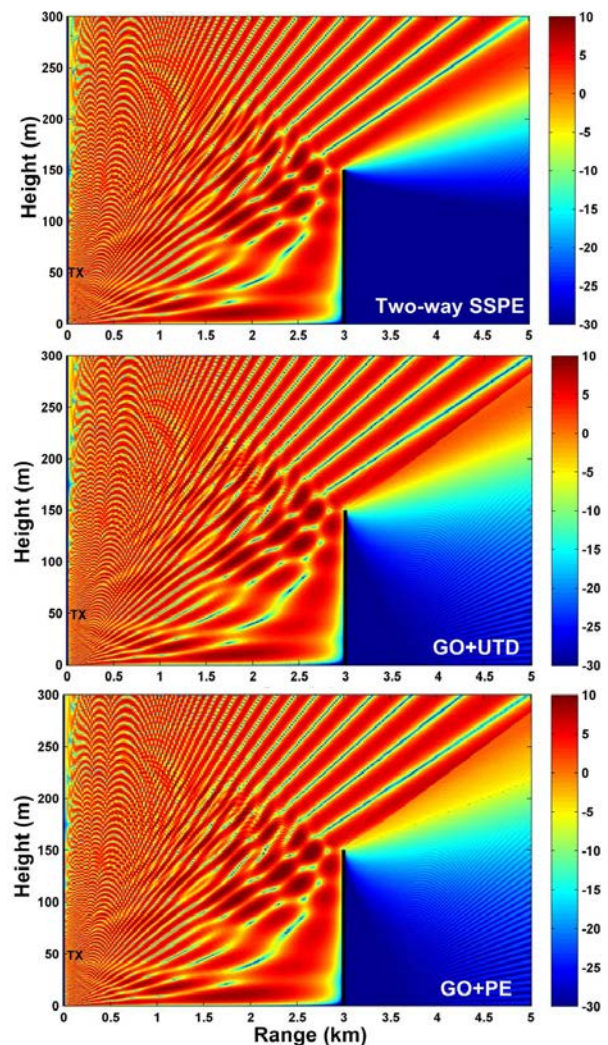


Fig. 3. 3D PF maps for a single knife edge above ground at 3 km range illuminated by a line-source at 50 m height (soft polarization): (a) Two-way SSPE, (b) GO+UTD, (c) GO+PE [$f = 300$ MHz].

¹ The propagation factor (PF) is the field strength relative to its free-space value in dB.

All techniques are also compared in Fig. 4, which shows the polar plot of the total field along a circle of radius 50 m centered at the tip of the single knife edge. In addition, in Figs. 5(a) and 5(b), the PF values are plotted at two different values of range (2.8 km and 4 km, which are in interference and shadow regions, respectively). In Figs. 5(c) and (d), similarly, the values are plotted at different height values (140 m and 160 m). It is concluded from the results that all analytical methods are in good harmony with each other. The results of the two-way SSPE are slightly different in the shadow region, as discussed above. However, it is remarkable to emphasize that the efficiency of the two-way SSPE, in terms of the computation time, is quite superior to the analytical techniques. Moreover, the two-way SSPE can easily be applied to any type of terrain or any number of knife-edges with little effort. If the analytical techniques are sorted according to the computation time, UTD is the fastest, and then the PE, exact integral and exact series methods come in order. But, especially in the exact methods, the computation time is highly dependent on the frequency and the distance between the observation point and the edge. Note that analytical exact models serve as reference if numerically computed accurately.

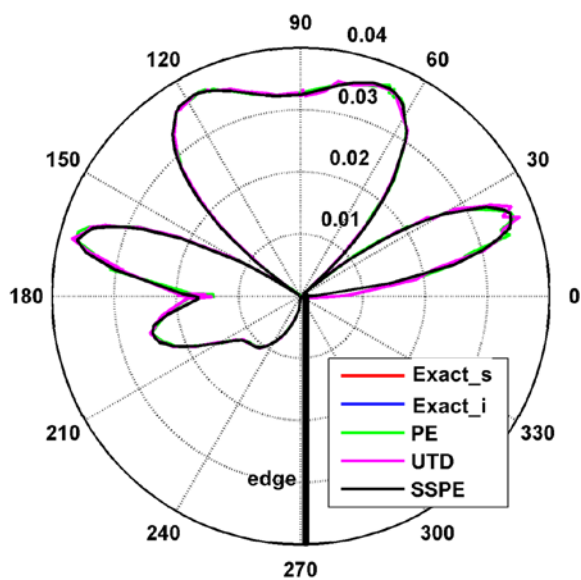


Fig. 4. Polar plot of the total field along a circle of radius 50 m centered at the tip of the single knife edge shown in Fig. 3. [s: series, i: integral].

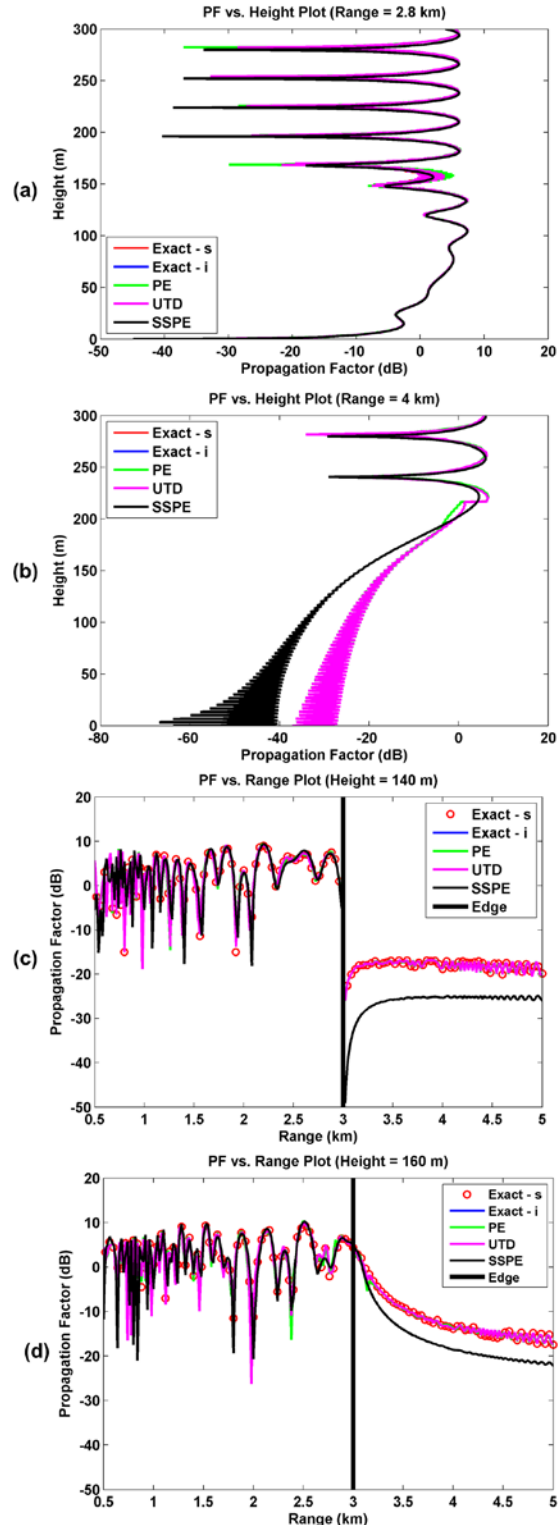


Fig. 5. 2D PF plots for the single knife edge problem shown in Fig. 3: (a) PF vs. height at 2.8 km range, (b) PF vs. height at 4 km range, (c) PF vs. range at 140 m height, (d) PF vs. range at 160 m height. [s: series, i: integral].

The second scenario is the same as the first one, except that the polarization is hard and the line-source is at 100 m height. The results are plotted in Figs. 6, 7, and 8. Again, a good agreement is observed among different models.

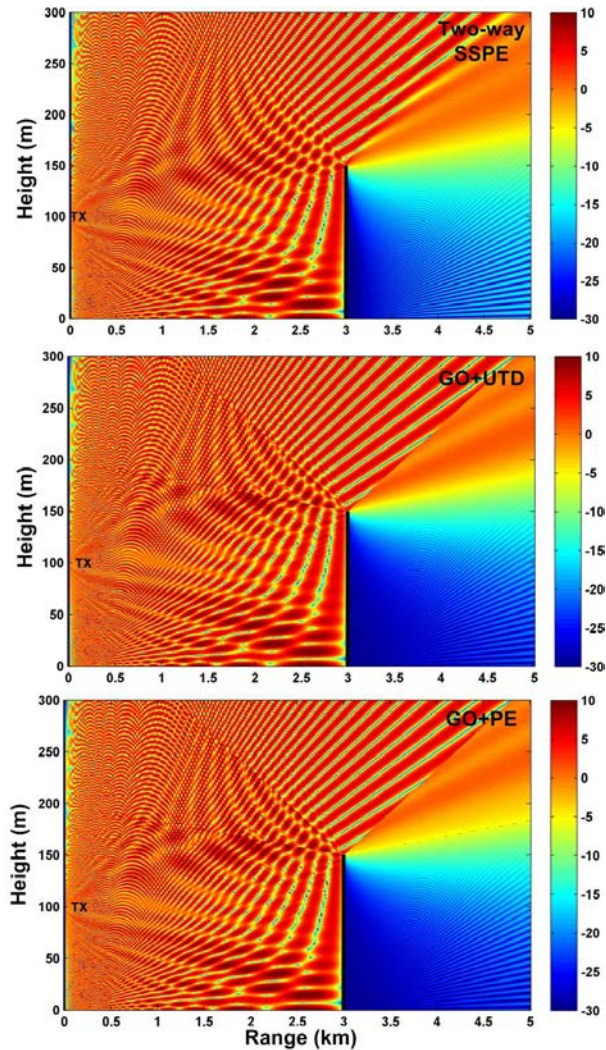


Fig. 6. 3D propagation factor maps for a single knife edge above ground at 3 km range illuminated by a line-source at 100 m height (hard polarization): (a) Two-way SSPE, (b) GO+UTD, (c) GO+PE. [f = 300 MHz].

The last scenario considers double knife-edge of heights 150 m and 170 m located at 3 km and 5 km, respectively. The line-source is at 25 m height; the frequency is 300 MHz; and the polarization is soft. The results are plotted in Figs. 9, 10, and 11. In comparing the two-way SSPE

with the analytical methods, the contributions of the waves hitting the walls up to 3 times are superposed. To achieve fair comparisons up to the third degree of reflections, the analytical methods account for 35 types of rays bouncing from the walls and the ground. The multiple bouncing of the diffracted fields from the walls and the ground is ignored due their negligible effects compared to strong reflections.

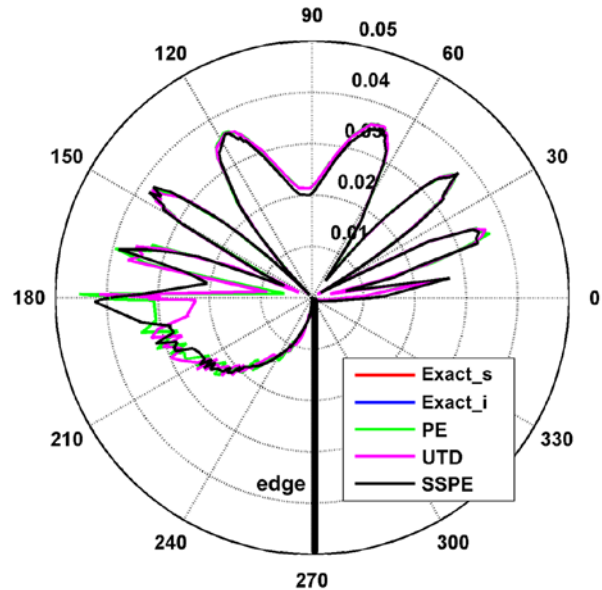


Fig. 7. Polar plot of the total field along a circle of radius 50 m centered at the tip of the single knife edge shown in Fig. 6. [s: series, i: integral].

Again, a good agreement is observed especially in the regions where strong multipath effects are observed, but some discrepancies exist between SSPE and the diffraction algorithms in the deep shadow region.

Simulations with double knife-edges and with other frequencies are repeated for the other polarization (i.e., hard boundary condition) and similar agreement among the models are obtained.

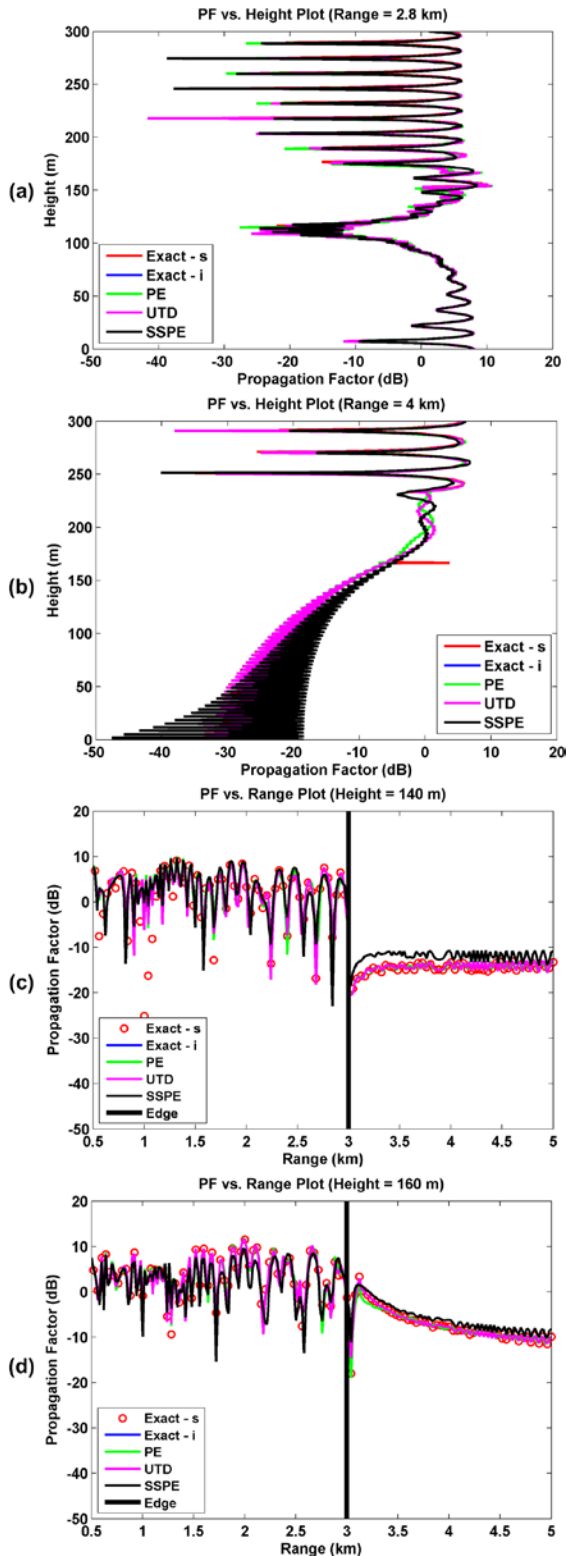


Fig. 8. 2D PF plots for the single knife edge problem shown in Fig. 6: (a) PF vs. height at 2.8 km range, (b) PF vs. height at 4 km range, (c) PF vs. range at 140 m height, (d) PF vs. range at 160 m height. [s: series, i: integral].

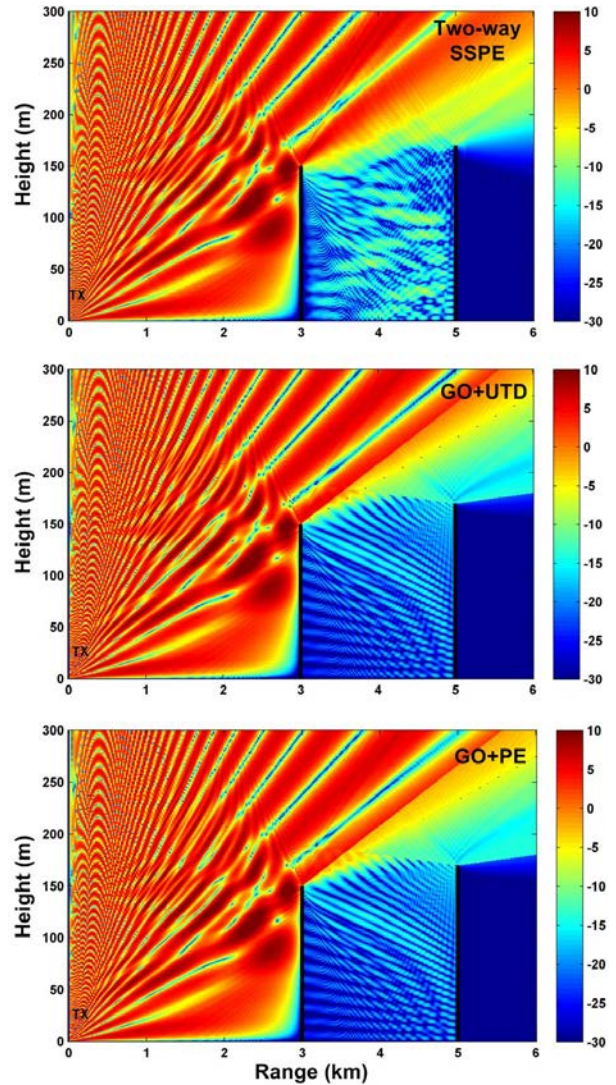


Fig. 9. 3D propagation factor maps for double knife edge above ground at 3 km and 5 km ranges illuminated by a line-source at 25 m height (soft polarization): (a) Two-way SSPE, (b) GO+UTD, (c) GO+PE. [f = 300 MHz].

V. CONCLUSION

Analytical (exact and asymptotic) techniques and the two-way SSPE were discussed and compared through several numerical simulations in the context of the problem of scattering from single and double edge above ground. It was concluded that the results are in good agreement in general, however, some differences might be observed in the deep shadow region or around the shadow boundaries. The disparity of the two-way SSPE in the shadow region, which indeed exhibits "small" field values, might be tolerated in favor of

its computational efficiency. Finally, MATLAB-based codes were provided in Appendix.

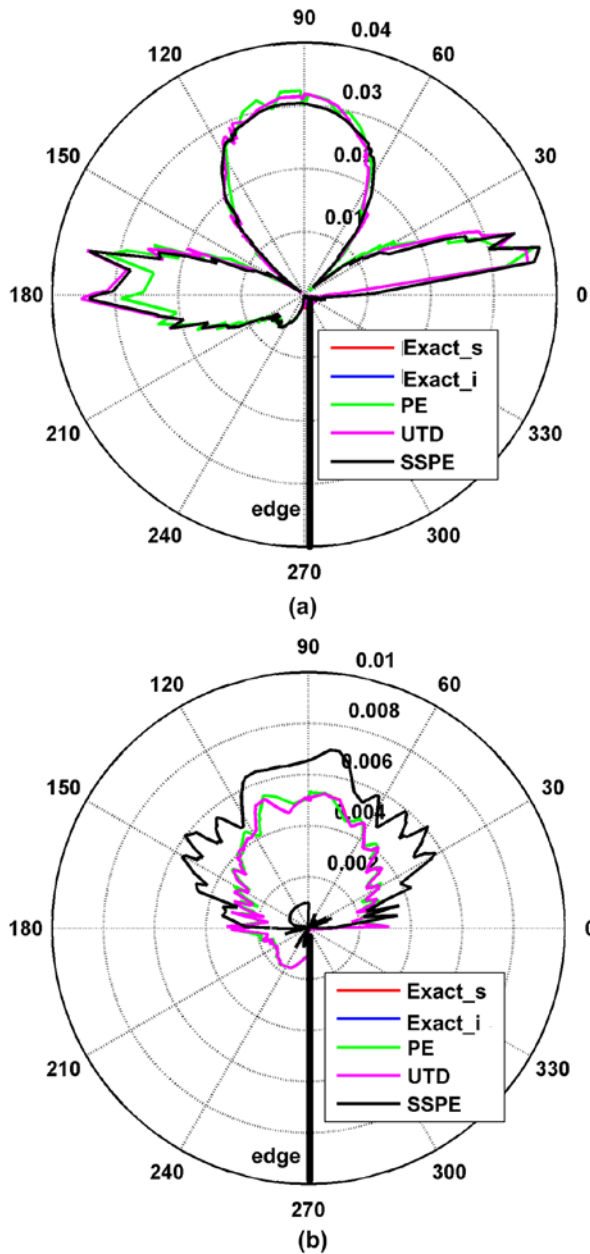


Fig. 10. Polar plot of the total field along a circle of radius 50 m centered at the tip of each knife edge shown in Fig. 9: (a) Edge at 3 km range, (b) Edge at 5 km range. [s: series, i: integral].

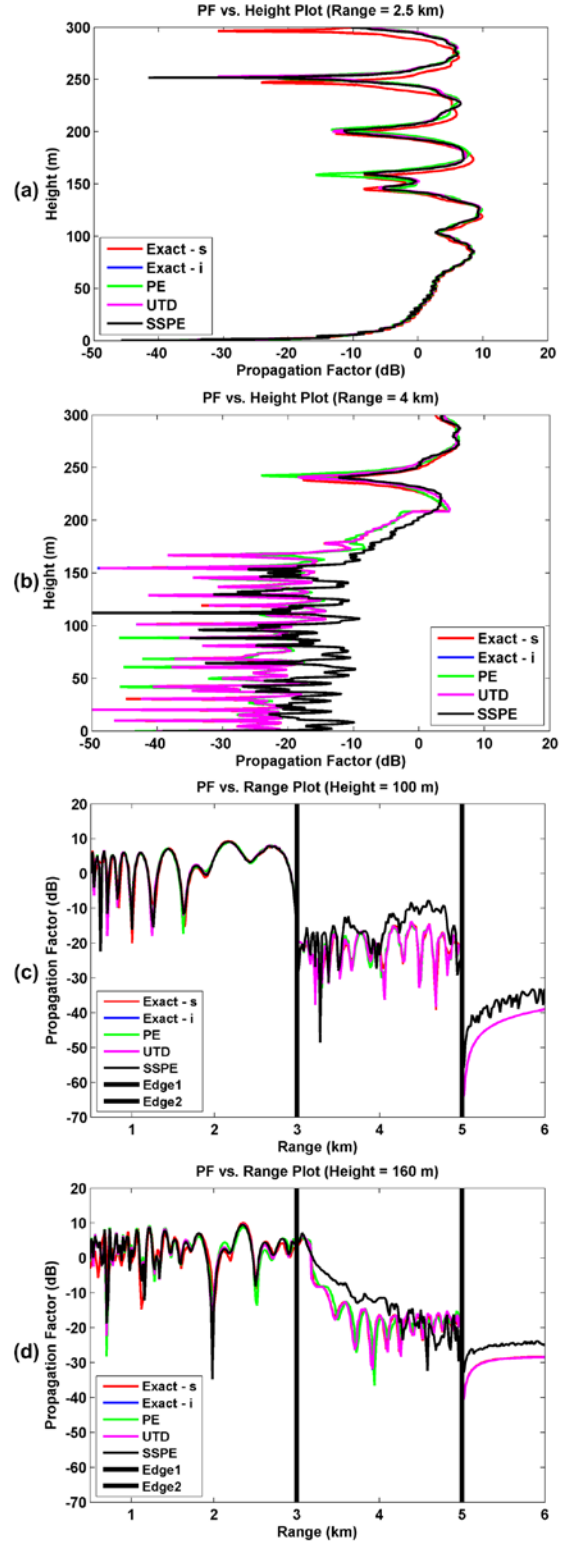


Fig. 11. 2D propagation factor (PF) plots for the double knife edge problem shown in Fig. 9: (a) PF vs. height at 2.5 km range, (b) PF vs. height at 4 km range, (c) PF vs. range at 100 m height, (d) PF vs. range at 160 m height. [s: series, i: integral].

APPENDIX

MATLAB Codes

Sample codes for the diffraction algorithms in Sec. II are given in Tables 1-5 below. The codes computing the 3D field maps of the single or double edge problem (with respect to various LOS conditions) can be provided upon request from the authors. Note that the two-way SSPE algorithm (PETOOL) can be downloaded from [25].

Table 1: Input parameters common to the codes

```
clear all; format long;
freq = 300; %input('frequency [MHz] = ');
alfamax = 360; %input('wedge angle [Deg] = ');
I0 = 1; %input('strength of line source = ');
r = 50; %input('distance of the observer to wedge = ');
r0 = 212; %input('distance of the source to wedge = ');
ang0 = 45; %input('incident angle [Deg] = ');
ang = 150; %input('observation angle [Deg] = ');
c = 3e8; % speed of light
alfa = alfacmax*pi/180; % change wedge angle degree to radians
ang0 = ang0*pi/180; % change incident angle degree to radians
ang = ang*pi/180; % change observation angle degree to radians
error = 1e-12;
freq = freq*1e6; rlam = r*freq/c; k = 2*pi*freq/c; kr = k*r; kr0 = k*r0;
```

Table 2: Code of the exact by series method

```
Us=0; Uh=0; n=0; vn=0; err1 = 1e6; err2 = 1e6; coeff1 = pi*I0/(1*alfa);
U0 = I0*besselh(0,1,kr0)/(4*i);
% define N for Soft BSc
while (err1 > error)
    vn1 = n*pi/alfa; vn2 = (n+1)*pi/alfa; vn3 = (n+2)*pi/alfa;
    vn4 = (n+3)*pi/alfa; vn5 = (n+4)*pi/alfa;
    if r <= r0
        a1 = besselj(vn1,kr)*besselh(vn1,1,kr0)*sin(vn1*ang0)*sin(vn1*ang);
        a2 = besselj(vn2,kr)*besselh(vn2,1,kr0)*sin(vn2*ang0)*sin(vn2*ang);
        a3 = besselj(vn3,kr)*besselh(vn3,1,kr0)*sin(vn3*ang0)*sin(vn3*ang);
        a4 = besselj(vn4,kr)*besselh(vn4,1,kr0)*sin(vn4*ang0)*sin(vn4*ang);
        a5 = besselj(vn5,kr)*besselh(vn5,1,kr0)*sin(vn5*ang0)*sin(vn5*ang);
        Xs = a1+a2+a3+a4+a5; err1 = abs(Xs);
    else
        a1 = besselj(vn1,kr0)*besselh(vn1,1,kr)*sin(vn1*ang0)*sin(vn1*ang);
        a2 = besselj(vn2,kr0)*besselh(vn2,1,kr)*sin(vn2*ang0)*sin(vn2*ang);
        a3 = besselj(vn3,kr0)*besselh(vn3,1,kr)*sin(vn3*ang0)*sin(vn3*ang);
        a4 = besselj(vn4,kr0)*besselh(vn4,1,kr)*sin(vn4*ang0)*sin(vn4*ang);
        a5 = besselj(vn5,kr0)*besselh(vn5,1,kr)*sin(vn5*ang0)*sin(vn5*ang);
        Xs = a1+a2+a3+a4+a5; err1 = abs(Xs);
    end
    n=n+1;
end
N1 = n+10;
% define N for Hard BSc
n=0; vn=0;
while (err2 > error)
    vn1 = n*pi/alfa; vn2 = (n+1)*pi/alfa; vn3 = (n+2)*pi/alfa;
    vn4 = (n+3)*pi/alfa; vn5 = (n+4)*pi/alfa;
    if (n == 0) eps = 0.5; else eps = 1; end
    if r <= r0
        b1 = eps*besselj(vn1,kr)*besselh(vn1,1,kr0)*cos(vn1*ang0)*cos(vn1*ang);
        b2 = eps*besselj(vn2,kr)*besselh(vn2,1,kr0)*cos(vn2*ang0)*cos(vn2*ang);
        b3 = eps*besselj(vn3,kr)*besselh(vn3,1,kr0)*cos(vn3*ang0)*cos(vn3*ang);
        b4 = eps*besselj(vn4,kr)*besselh(vn4,1,kr0)*cos(vn4*ang0)*cos(vn4*ang);
        b5 = eps*besselj(vn5,kr)*besselh(vn5,1,kr0)*cos(vn5*ang0)*cos(vn5*ang);
        Xh = b1+b2+b3+b4+b5; err2 = abs(Xh);
    else
        b1 = eps*besselj(vn1,kr0)*besselh(vn1,1,kr)*cos(vn1*ang0)*cos(vn1*ang);
        b2 = eps*besselj(vn2,kr0)*besselh(vn2,1,kr)*cos(vn2*ang0)*cos(vn2*ang);
        b3 = eps*besselj(vn3,kr0)*besselh(vn3,1,kr)*cos(vn3*ang0)*cos(vn3*ang);
        b4 = eps*besselj(vn4,kr0)*besselh(vn4,1,kr)*cos(vn4*ang0)*cos(vn4*ang);
        b5 = eps*besselj(vn5,kr0)*besselh(vn5,1,kr)*cos(vn5*ang0)*cos(vn5*ang);
        Xh = b1+b2+b3+b4+b5; err2 = abs(Xh);
    end
end
```

```
n=n+1;
end
N2 = n+10; n = 0;
% Calculating Diffracted and Total Field
while N1 > n
    vn = n*pi/alfa;
    if n == 0 eps = 0.5; else eps = 1; end
    if r <= r0, Us=Us+besselj(vn,kr)*besselh(vn,1,kr0)*sin(vn*ang0)*sin(vn*ang);
    else, Us=Us+eps*besselj(vn,kr0)*besselh(vn,1,kr)*sin(vn*ang0)*sin(vn*ang);
    end
    n=n+1;
end
n = 0;
while N2 > n
    vn = n*pi/alfa;
    if n == 0 eps = 0.5; else eps = 1; end
    if r <= r0
        Uh=Uh+eps*besselj(vn,kr)*besselh(vn,1,kr0)*cos(vn*ang0)*cos(vn*ang);
    else
        Uh=Uh+eps*besselj(vn,kr0)*besselh(vn,1,kr)*cos(vn*ang0)*cos(vn*ang);
    end
    n=n+1;
end
Us=Us*coeff1; Uh=Uh*coeff1;
if (ang >= 0) && (ang < pi-ang0) % ----- Region I -----
    R1=sqrt(r*r+r0*r0-2*r*r0*cos(ang-ang0));
    R2=sqrt(r*r+r0*r0-2*r*r0*cos(ang+ang0));
    Uxs=I0*besselh(0,1,k*R1)/(4*i)-I0*besselh(0,1,k*R2)/(4*i);
    Uxh=I0*besselh(0,1,k*R1)/(4*i)+I0*besselh(0,1,k*R2)/(4*i);
    Usdiff = Us-Uxs; Uhdiff = Uh-Uxh;
elseif (ang >= pi-ang0) && (ang < pi+ang0) % ----- Region II -----
    R1=sqrt(r*r+r0*r0-2*r*r0*cos(ang-ang0));
    Ux=I0*besselh(0,1,k*R1)/(4*i); Usdiff = Us-Ux; Uhdiff = Uh-Ux;
elseif (ang >= pi+ang0) && (ang <= alfa) % ----- Region III -----
    Usdiff = Us; Uhdiff = Uh;
end
UhnTOTAL_SERIES= (Uh/U0); % exact normalised Total fields hard
UhnDIFF_SERIES=(Uhdiff/U0)*sqrt(2*pi*kr)/exp(1i*kr); % exactdiffco hard
UsnTOTAL_SERIES= (Us/U0); % exact normalised Total fields Soft
UsnDIFF_SERIES=(Usdiff/U0)*sqrt(2*pi*kr)/exp(1i*kr); % exactdiffco soft
UsnDIFF_SERIES = conj(UsnDIFF_SERIES/sqrt(2*pi*k))
UhnDIFF_SERIES = conj(UhnDIFF_SERIES/sqrt(2*pi*k))
```

Table 3: Code of the exact by integral method

```
sgm = (2*pi-alfa)/2; phi0 = ang0+sgm; B = ang+sgm;
nu = (2*pi-2*sgm)/pi; phi = B; m = 0; U0 = besselh(0,1,kr0);
V1 = Vd_Int(-pi-phi+phi0,r,r0,nu,k); V2 = Vd_Int(pi-phi+phi0,r,r0,nu,k);
V3 = Vd_Int(-pi-phi-phi0+2*sgm,r,r0,nu,k);
V4 = Vd_Int(pi-phi-phi0+2*sgm,r,r0,nu,k);
UsnDIFF = (V1-V2-V3-V4)/U0; % exact normalised diffracted fields
UhnDIFF = (V1-V2+V3-V4)/U0; % exact normalised diffracted fields
BWsndIFF = UsnDIFF*sqrt(2*pi*kr)/exp(1i*kr); % diff coeff for soft BCs
BWhndIFF = UhnDIFF*sqrt(2*pi*kr)/exp(1i*kr); % diff coeff for hard BCs
BWsndIFF = conj(BWsndIFF/sqrt(2*pi*k))
BWhndIFF = conj(BWhndIFF/sqrt(2*pi*k))
%-----
% Function : Vd_Int.m (calculate Vd integral on deformed contour )
function result = Vd_Int(beta,ro,ro0,nu,k)
    eps = 1e-12; d = 1e-3; % step size of the integration
    Mmax = 5000; y0 = min(pi,abs(beta)); fun = 1e6; x = y0-0.01;
    while ( abs(fun)>eps ) % controlling maximum x value
        z = x+1i*(y0-0.01); R_it = sqrt(ro*ro+ro0*ro0+2*ro*ro0*cos(1i*z));
        fun = besselh(0,1,k*R_it)/(cosh(z/nu)-cos(beta/nu)); x = x+0.2;
    end
    xmax = x; tan_teta = (y0-0.01)/xmax; % slope of the deformed contour
    x = 0;d:xmax; z1 = x+1i*x*tan_teta; % deformed contour
    R_it_1 = sqrt(ro*ro+ro0*ro0+2*ro*ro0*cos(1i*z1));
    fun1 = sin(beta/nu)*besselh(0,1,k*R_it_1)/(cosh(z1/nu)-cos(beta/nu));
    y1 = trapz(z1,fun1); result = (y1)/(2*pi*nu);
```

Table 4: Code of the UTD method

```
phi0 = -ang0; n = (alfa)/pi; B = -ang; phi = B;
ksi_p = phi+phi0; ksi_m = phi-phi0; % ksi+ and ksi-
Npp = (pi+ksi_p)/(2*pi*n); Npm = (pi+ksi_m)/(2*pi*n); % N+
Nmp = (-pi+ksi_p)/(2*pi*n); Nmm = (-pi+ksi_m)/(2*pi*n); % N-
m = 0; U0 = besselh(0,1,kr0); coeff = exp(-1i*pi/4)/(2*n*sqrt(2*pi*k));
if (Npp<1) || (Npm<1) , Npp = 0; Npm = 0;
```

```

elseif (Npp>=1) || (Npm>=1), Npp = 1; Npm = 1;
end
if (Nmp<0) || (Nmm<0), Nmp = -1; Nmm = -1;
elseif (0<=Nmp<1) || (0<=Nmm<1), Nmp = 0; Nmm = 0;
elseif (Nmp>=1) || (Nmm>=1), Nmp = 1; Nmm = 1;
end
gpp = 1+cos(ksi_p-2*n*pi*Npp); gpm = 1+cos(ksi_m-2*n*pi*Npm);
gmp = 1+cos(ksi_p-2*n*pi*Nmp); gmm = 1+cos(ksi_m-2*n*pi*Nmm);
x1 = k*r*r0*gpm/(r+r0); x2 = k*r*r0*gmm/(r+r0);
x3 = k*r*r0*gpp/(r+r0); x4 = k*r*r0*gmp/(r+r0);
F1 = Fresnel_Int(x1); F2 = Fresnel_Int(x2); F3 = Fresnel_Int(x3);
F4 = Fresnel_Int(x4);
UsDIFF_UTD = -coeff*(cot((pi+ksi_m)/(2*n))*F1+cot((pi-
ksi_m)/(2*n))*F2...
-cot((pi+ksi_p)/(2*n))*F3-cot((pi-ksi_p)/(2*n))*F4); % coeff for soft BCs
UhDIFF_UTD = -coeff*(cot((pi+ksi_m)/(2*n))*F1+cot((pi-
ksi_m)/(2*n))*F2...
+cot((pi+ksi_p)/(2*n))*F3+cot((pi-ksi_p)/(2*n))*F4); % coeff for hard BCs
Us_UTD=UsDIFF_UTD*sqrt(2*pi*k);
Uh_UTD=UhDIFF_UTD*sqrt(2*pi*k);
% ----- Total Field for UTD -----
if (ang >= 0) && (ang < pi-ang0) % ----- Region I -----
R1=sqrt(r*r+r0*r0-2*r*r0*cos(phi-phi0));
R2=sqrt(r*r+r0*r0-2*r*r0*cos(phi+phi0));
Uxs=besselh(0,1,k*R1)-besselh(0,1,k*R2);
Uxh=besselh(0,1,k*R1)+besselh(0,1,k*R2);
UsTOTAL_UTD = UsDIFF_UTD+Uxs/U0;
UhTOTAL_UTD = UhDIFF_UTD+Uxh/U0;
elseif (ang >= pi-ang0) && (ang < pi+ang0) % ----- Region II -----
R1=sqrt(r*r+r0*r0-2*r*r0*cos(phi-phi0)); Ux=besselh(0,1,k*R1);
UsTOTAL_UTD = UsDIFF_UTD+Ux/U0;
UhTOTAL_UTD = UhDIFF_UTD+Ux/U0;
elseif (ang >= pi+ang0) && (ang <= alpha) % ----- Region III -----
UsTOTAL_UTD = UsDIFF_UTD; UhTOTAL_UTD = UhDIFF_UTD;
end
Us_UTD = Us_UTD/sqrt(2*pi*k)
Uh_UTD = Uh_UTD/sqrt(2*pi*k)
% -----
% Function : Fresnel_Int.m (Fresnel integral)
function result = Fresnel_Int(x)
Ml = 0.3; Mu = 5.5; coeff = 2*i*sqrt(x)*exp(1i*x);
if (x < Ml)
result = exp(1i*(pi/4+x))*sqrt(pi*x)-2*x*exp(1i*pi/4)-(2/3)*x*x*exp(-
1i*pi/4);
elseif (x > Mu)
result = 1+1i/(2*x)-3/(4*x^2)-15*1i/(8*x^3)+75/(16*x^4);
else
eps = 1e-12; Mmax = 5000; d = 1e-3; y_old = 1e6; ii = 0;
for M=sqrt(x)+1:Mmax
ii = ii+1; t1 = sqrt(x);d:M; t2=0:d:M-sqrt(x); t = t1-1i*t2;
fun = exp(-1i*t.*t); y(ii) = trapz(t,fun); error = abs(y(ii)-y_old);
y_old = y(ii);
if (error<eps) , result = y(ii)*coeff; break;
else continue
end
end
result = y(ii)*coeff;
end

```

Table 5: Code of the PE diffraction method

```

n = alfa/pi; rho=r*r0/(r+r0); m=0; krho=k*rho; psi = ang-ang0;
w1 = Int_calcPE2(alfa,krho,psi)*exp(1i*(krho+pi/4))/(pi*sqrt(2));
psi = ang+ang0;
w2 = Int_calcPE2(alfa,krho,psi)*exp(1i*(krho+pi/4))/(pi*sqrt(2));
Ws=(w1-w2)*exp(-1i*krho); Wh=(w1+w2)*exp(-1i*krho);
Us_PE = Ws*sqrt(r0/(r0+r))*exp(1i*kr); % normalized PE diff field -soft
Uh_PE = Wh*sqrt(r0/(r0+r))*exp(1i*kr); % normalized PE diff field -hard
PEs_DiffCoeff = Us_PE*sqrt(2*pi*kr)/exp(1i*kr);
PEh_DiffCoeff = Uh_PE*sqrt(2*pi*kr)/exp(1i*kr);
PEs_DiffCoeff = conj(PEs_DiffCoeff)/sqrt(2*pi*k)
PEh_DiffCoeff = conj(PEh_DiffCoeff)/sqrt(2*pi*k)
% -----
% Function : Int_calcPE2.m
function result = Int_calcPE2(alfa,kr,psi)
eps = 1e-12; n = alfa/pi; y_old = 1e6; result = 0;
for M=1:100
s = -M:0.0001:M; eta=sqrt(2).*s.*exp(-1i*pi/4);
F2 = (1/n).*sin(pi/n)/(cos(pi/n)-cos(eta+psi/n));
fun = exp(-kr*s.*s).*F2;

```

```

y(M) = trapz(s,fun); error = abs(y(M)-y_old); y_old = y(M);
if (error<eps) , result = y(M); N = M; break;
else, continue
end
end
end

```

REFERENCES

- [1] A. Sommerfeld, "Mathematische Theorie der Diffraction," *Mathematische Annalen*, vol. 16, pp. 317-374, 1896.
- [2] H. M. Macdonald, *Electric Waves*, The University Press, Cambridge, England, 1902.
- [3] A. Sommerfeld, *Theorie der Beugung*, Chapter 20 in the book "Die Differential- und Integralgleichungen der Mechanik und der Physik", The second (Physical) part. Editors: Ph. Frank and R. Mises, Friedr. Vieweg & Sohn, Braunschweig, Germany, 1935. American publication by Mary S. Rosenberg, New York, 1943.
- [4] G. D. Malyuzhinets, "Development of Ideas about Diffraction Phenomena," *Soviet Physics-Uspekhi*, vol. 69, no. 2, p. 5, 1959.
- [5] V. A. Fock and L. A. Wainshtein, "Transverse Diffusion of Short Waves Diffracted by a Convex Cylinder, Part 1 and 2," (in Russian) *Radiotekhnika i Elektronika*, vol. 8, no. 3, pp. 363-388, 1963. (This journal was translated into English as *Radio Engineering and Electronic Physics* by Scripta Technica.)
- [6] J. J. Bowman, T. B. A. Senior, and P. L. E. Uslenghi, Eds., *Electromagnetic and Acoustic Scattering by Simple Shapes*, Hemisphere Publishing Corporation, 1987.
- [7] V. A. Fock, *Electromagnetic Diffraction and Propagation Problems*, Pergamon Press, London, 1965.
- [8] J. B. Keller, "Geometrical Theory of Diffraction," *J. Opt. Soc. Amer.*, vol. 52, pp. 116-30, 1962.
- [9] C. Hansen, Ed., *Geometrical Theory of Diffraction*, IEEE Press, 1981.
- [10] P. H. Pathak and R. G. Kouyoumjian, "The Dyadic Diffraction Coefficient for a Perfectly Conducting Wedge," *Technical report# 2183-4, ElectroScience Laboratory, The Ohio State University*, prepared under contract number AF19 (628)-5929 for Air Force Cambridge Research Laboratories (AFCLR), Bedford, Mass., June 1970.
- [11] R. G. Kouyoumjian and P. H. Pathak, "A Uniform Geometrical Theory of Diffraction for an Edge in a Perfectly Conducting Surface," *Proc. IEEE*, vol. 62, pp. 1448-1461, 1974.
- [12] P. Ya. Ufimtsev, *Fundamentals of the Physical Theory of Diffraction*, Wiley & Sons, Inc., Hoboken, New Jersey, 2007.

- [13] P. Ya. Ufimtsev, *Theory of Edge Diffraction in Electromagnetics: Origination & Validation of PTD*, SciTech Publishing, Inc., 2009.
- [14] F. Hacivelioglu, L. Sevgi, and P. Ya. Ufimtsev, "Electromagnetic Wave Scattering from a Wedge with Perfectly Reflecting Boundaries: Analysis of Asymptotic Techniques," *IEEE Antenn. and Propagat. Mag.*, vol. 53, no. 3, pp. 232-253, 2011.
- [15] G. Cakir, L. Sevgi, and P. Ya. Ufimtsev, "FDTD Modeling of Electromagnetic Wave Scattering from a Wedge with Perfectly Reflecting Boundaries: Comparisons against Analytical Models and Calibration," *IEEE Trans. on Antennas and Propagat.* (to appear) July 2012.
- [16] F. Cátedra, L. Lozano, I. González, E. García, and M. Algar, "Efficient Techniques for Accelerating the Ray-Tracing for Computing the Multiple Bounce Scattering of Complex Bodies Modeled by Flat Facets," *Applied Computational Electromagnetics Society (ACES) Journal*, vol. 25, no. 5, pp. 395-409, May 2010.
- [17] F. Weinmann, "UTD Shooting-and-Bouncing Extension to a PO/PTD Ray Tracing Algorithm," *Applied Computational Electromagnetics Society (ACES) Journal*, vol. 24, no. 3, pp. 281-293, June 2009.
- [18] R. H. Hardin, and F. D. Tappert, "Applications of the Split-Step Fourier Method to the Numerical Solution of Nonlinear and Variable Coefficient Wave Equations," *SIAM Rev.*, vol. 15, p. 423, 1973.
- [19] J. R. Kuttler and G. D. Dockery, "Theoretical Description of the Parabolic Approximation / Fourier Split-Step Method of Representing Electromagnetic Propagation in the Troposphere," *Radio Sci.*, vol. 26, pp. 381-393, 1991.
- [20] M. F. Levy, *Parabolic Equation Methods for Electromagnetic Wave Propagation*, IEEE Electromagnetic Wave Series, London, 2000.
- [21] L. Sevgi, *Complex Electromagnetic Problems and Numerical Simulation Approaches*, IEEE Press/John Wiley, New York, 2003.
- [22] G. Apaydin and L. Sevgi, "Validation, Verification and Calibration in Applied Computational Electromagnetics", *Applied Computational Electromagnetics Society (ACES) Journal*, vol. 25, no. 12, pp. 1026-1035, Dec. 2010.
- [23] O. Ozgun, "Recursive Two-Way Parabolic Equation Approach for Modeling Terrain Effects in Tropospheric Propagation," *IEEE T Antenn. Propag.*, vol. 57, no. 9, pp. 2706-2714, Sept. 2009.
- [24] O. Ozgun, G. Apaydin, M. Kuzuoglu, and L. Sevgi, "Two-Way Fourier Split Step Algorithm over Variable Terrain with Narrow and Wide Angle Propagators," *IEEE Int. Symp. on Antenn. and Propag.*, ON, Canada, 2010.
- [25] O. Ozgun, G. Apaydin, M. Kuzuoglu, and L. Sevgi, "PETOOL: MATLAB-Based One-Way and Two-Way Split-Step Parabolic Equation Tool for Radiowave Propagation over Variable Terrain," *Computer Physics Communications*, vol. 182, no. 12, pp. 2638-2654, Dec. 2011.
Associated program is available at: http://cpc.cs.qub.ac.uk/summaries/AEJS_v1_0.html
- [26] F. Hacivelioglu, L. Sevgi, P. Ya. Ufimtsev, "Electromagnetic Wave Scattering from a Wedge with Perfectly Reflecting Boundaries: Analysis of Asymptotic Techniques," *IEEE Antennas and Propagation Magazine*, vol. 53, no. 3, pp. 232-253, June 2011.

Özlem Özgün received the Ph.D. degree in Electrical



Engineering from Middle East Technical University (METU), Ankara, Turkey, in 2007. She was with the same university between 2008-2012. She is now an associate professor in TED University, Ankara, Turkey. Her main research interests are computational electromagnetics,

finite element method, domain decomposition, electromagnetic propagation and scattering, metamaterials, and stochastic electromagnetic problems.



Levent Sevgi has been with Dogus University since 2002. He has involved in complex electromagnetic problems for more than two decades. He is also interested in novel approaches in engineering education, teaching electromagnetics via virtual tools and popular science.

He is a member of Turkish Chamber of Electrical Engineers (EMO), a Fellow member of the IEEE, an assoc. Editor, of the IEEE Antennas and Propagation Magazine, "Testing ourselves" Column and member of the IEEE Antennas and Propagation Society Education Committee.

Numerical Prepackaging with PMC Lid – Efficient and Simple Design Procedure for Microstrip Circuits Including the Packaging

¹Ahmed Kishk, ²Ashraf Uz Zaman, and ²Per-Simon Kildal

¹Department of Electrical and Computer Engineering
Concordia University, Montreal, Quebec H3G 1M8, Canada
kishk@encs.concordia.ca

² Department of Signals and System
Chalmers University of Technology, Göteborg, SE-41296, Sweden
zaman@chalmers.se; per-simon.kildal@chalmers.se

Abstract — The paper presents an efficient method for the design of printed microstrip circuit with packaging in mind, referred to as numerical prepackaging with a perfectly magnetic conductive (PMC) lid. The method comprises making the design including the packaging from the start by using a PMC lid, rather than first designing the open-aired circuit; and thereafter, considering the packaging effect and the often required retuning of the circuits themselves. The advantage is that no parallel plate modes can propagate between the perfect electric conductor (PEC) ground plane and the PMC lid plate if the spacing is smaller than an effective quarter of wavelength. This provides a limited computational volume so that the computation time is significantly reduced in the case of the finite element method (FEM) or the finite difference time domain method (FDTD). By using numerical packaging with PMC lid, the ideal PMC lid has to be realized afterwards e.g. by using a lid of nails, which is a minor task as compared to existing approaches.

Index terms- Cavity resonance, FDTD, FEM, PMC, PEC, shielded microstrip line.

I. INTRODUCTION

In the design of printed microwave circuits using numerical methods such as the finite difference time domain method (FDTD) [1], finite element method (FEM) [2], finite integral method [3] or any volume type formulations, it is necessary to limit the computational space using virtual boundaries such as radiation boundaries [4]

or perfect matching boundaries [5] in terms of different implementations as described in [6-8]. In order to use such boundaries some restriction should be enforced to make valid computations. For example, it is recommended that the distance between these boundaries and the actual circuits to be in order of a quarter wavelengths at the low frequency to have reliable results. Some of the perfect matching boundary conditions require several layers [1] that in some cases would be eight layers. Such requirement regarding the distance of the virtual boundaries increases the overhead of computational time and storage. After reaching a final circuit design in such a way, one will always need to package the circuit. In order to have a compact package circuit it is important that the package cavity be very close to the circuit. However, such packaging should not affect the circuit performance. Some engineers might use resistive loading inside the packaging cavity to suppress resonances of the cavity appearing within the operating frequency band. Such a technique increases the losses and reduces the circuit efficiency. It would be better if the packaging is not affecting the circuit efficiency and at the same time be compact and nearly lossless. However, as the packaging gets closer to the circuit, packaging might interact with the circuit and affect its performance and the designer might find that some tuning of his circuit is necessary to achieve the desired performance. Such a tuning may be quite tedious to perform and requires experience in designing circuits.

Here, we propose an efficient procedure to design printed circuits with packaging in mind.

Packaging is needed for mechanical protection, but also to shield the circuits from outside strong fields and interference, and to prevent any possible radiation emissions from the circuit. In some cases resistive loading inside the package cavity can be used to suppress high order modes. Here, we propose, during the initial design to use perfect magnetic conductor (PMC) lid to shield the circuit and to consider it as an ideal packaging approach, which also will confine the computational domain volume. From the circuit point of view, one might consider the PMC as an open circuit surface dual to the perfect electric conductor (PEC) that is a short circuit surface. Note that a metal surface to a very good approximation can be considered a PEC in electromagnetic (EM) field analysis. PMC and PEC surfaces can be used as boundaries that limit the computational domain. Since PMC could be considered as an open circuit, its influence on the printed circuit is much smaller than a PEC (i.e. a metal surface). Possible parallel plate waveguide modes will be suppressed as far as the effective height of the parallel plates between the ground PEC and the PMC lid is less than an effective quarter wavelength [6]. As resonances are suppressed from the cavity the convergence of the FDTD method should improve as well. One might object on using PMC as it does not exist in nature, but nowadays we can artificially realize PMC or high impedance surfaces or what is referred to as an artificial magnetic conductor (AMC) using periodic surfaces. There are many ways to realize such surfaces, but it is important to realize it in a way that will not increase the losses of the system. Actually, the PMC lid packaging relates more to realizing a parallel-plate cut-off (or stopband) between PEC and AMC, and different ways of realizing this are studied numerically in [10]. The simplest realization is in terms of a lid of nails or pins, for which the practical demonstration of usefulness to packaging is described in [11].

The PMC prepackaging is a result of research on soft and hard surfaces originating from a generalization of the corrugated surfaces used in corrugated horn antennas. This surface concept was first defined in 1988, and improved in 1990 [12]. The hard surface was already in 1996 applied to realize what today is known as cloaking [13]. The original soft surface is a transverse PEC/PMC

strip grid acting as an anisotropic electromagnetic bandgap (EBG) surface, as explained in [14] and [16]. Other marvels of EBG surfaces are described in [15]. The ideal PEC surface, PMC and PEC/PMC strip grids are in [16] referred to as canonical surfaces. The use of simplified canonical representations of advanced periodic surfaces with many details is very important in conceptual and numerical work; in conceptual work they improve physical understanding and creativity, and in numerical work they are fast and convenient to use in initial studies. The canonical surface concept has e.g. resulted in the present PMC prepackaging approach. Note that canonical representation of the EBG surface is proposed in [17], although not yet being so generally applicable as the PEC, PMC, and PEC/PMC strip grid. The EBG surface can also be used to create parallel-plate cut-off [10]. The concepts of soft and hard surfaces and canonical surfaces are also the background of the gap waveguide technology, as introduced in [6], verified by measurements in [11-18], and studied by plane wave spectral domain solutions in [19] and by classical subdomain plane wave expansions in [20]. The latter theoretical work is extended to more analytic expressions in [20]. There exists three types of gap waveguides; ridge gap waveguide, groove gap waveguide, and microstrip gap waveguide [22]. The PMC packaged microstrip line of the present paper is a kind of microstrip gap waveguide.

In this paper, we perform a parametric study of microstrip transmission lines in the presence of PMC cover. We look at what is the proper separation distance between the microstrip lines and the PMC that does not affect the original characteristic of the microstrip lines as ideal transmission line. We also study the effect of the PMC shielding on microstrip lines that violates the radiation condition as provided in [23-24]. The study shows how the PMC shielding removes such radiation condition constraints. Also, we look at some discontinuities that cause radiation losses from the circuit and how the PMC shielding also suppress such radiation losses. After that we introduce a periodic structure that is designed to realize the PMC surface and compare the ideal PMC shielding with the realized artificial magnetic conductor. We believe that such a procedure will eliminate or at least reduce the

needs for any tuning for the printed circuit after packaging. In addition, the design can be performed in one combined process, which certainly will be much faster than what is currently performed (as the circuit is designed in one process and the packaging in a second process). For the proposed design to be implemented, the software has to have the ability to model and include PMC surfaces. There are several commercial software codes that have such capabilities. Here, we considered a commercial software CST microwave studio [25], which is based on the volume integral equation in frequency and time domain.

II. COMPARISON OF RESONANCE FREQUENCIES OF CAVITIES WITH PEC OR PMC LIDS

Usually, printed circuits are packaged in a conducting cavity, i.e. the circuit is located in a metal box so that it is surrounded by six conducting walls (ground plane, four conducting sidewalls, and a conducting lid). This creates an inhomogeneous cavity as shown in Fig. 1, i.e. being filled with a dielectric substrate layer located on the ground plane wall and with metal traces on the other side of it. The height h of the cavity is suggested to be higher than the substrate surface by 5 or 4 times substrate thickness in order not to affect the characteristic impedances of the microstrip lines, and not to interact with the circuit, and in turn not to affect the designed circuit performance. Since the total height is usually small, a transverse magnetic TM_z mode with mainly z -directed electric field is supported. This makes the first resonance of the cavity determined by the dimensions of the ground-plane of the cavity. If the cavity modes are within the operating frequency band of the circuit, the cavity will interact strongly with the circuit and distort its characteristics. The effect is in particular severe when packaging active components such as mixers, oscillators, and amplifiers. The cavity may be loaded with resistive sheets or absorbers in order to suppress the resonances.

However, if the cavity has a PMC lid, the TM_z mode will be in cut-off, as well as TE_z modes, as long as the cavity height is smaller than a quarter of the wavelength, effectively. Therefore, the first resonance will appear at a much higher frequency

than for the PEC lid case. The PMC concept is rather new, so it is not possible to find fundamental results like resonance frequencies of conducting cavities with PMC lids. Therefore, we will here present the formulas together with those of a conducting cavity with PEC lid. To that end, we consider an ideal rectangular cavity with PEC floor and sidewalls, and either a PEC or PMC lid at a height h above the floor, and the cavity has a dielectric layer of thickness t at the floor, as shown in Fig. 1. The cavity planar dimensions are $a \times b$, and ϵ_1 is the relative permittivity of the dielectric substrate.

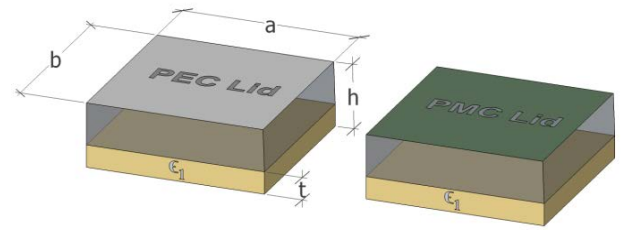


Fig. 1. Partially filled cavity with PEC base and sidewalls, and (a) PEC lid and (b) PMC lid. The sidewalls are not shown.

The resonance frequencies can for the PEC lid case be obtained by solving the transcendental dispersion equations, in [26] for k_z , i.e.

for TM_x mode:

$$\frac{k_{z1}}{\epsilon_1} \tan k_{z1} t = -\frac{k_{z2}}{\epsilon_2} \tan k_{z2} (h - t) \quad (1.a)$$

for TE_x mode:

$$k_{z1} \cot k_{z1} t = -k_{z2} \cot k_{z2} (h - t) \quad (1.b)$$

Similar equations can be derived for the PMC lid case, taking the form:

for TM_x modes:

$$\frac{k_{z1}}{\epsilon_1} \tan k_{z1} t = \frac{k_{z2}}{\epsilon_2} \cot k_{z2} (h - t) \quad (2.a)$$

for TE_x modes:

$$k_{z1} \cot k_{z1} t = k_{z2} \tan k_{z2} (h - t) \quad (2.b)$$

where in both cases

$$k_{z1} = \left[\omega^2 \varepsilon_1 \mu - \left(\frac{n\pi}{a} \right)^2 + \left(\frac{m\pi}{b} \right)^2 \right]^{1/2} \quad (3.a)$$

$$k_{z2} = \left[\omega^2 \varepsilon_2 \mu - \left(\frac{n\pi}{a} \right)^2 + \left(\frac{m\pi}{b} \right)^2 \right]^{1/2} \quad (3.b)$$

and where n and m are integer numbers.

For a homogeneous cavity there exists closed form expressions for the resonant frequencies, which for the TM_z case is given as:

$$f(\text{GHz})_{\text{mnl}}^{\text{PEC}} = \sqrt{\left[\left(\frac{l\pi}{d} \right)^2 + \left(\frac{n\pi}{a} \right)^2 + \left(\frac{m\pi}{b} \right)^2 \right]}, l=0,1,2,\dots, m=1,2,\dots, n=1,2,\dots \quad (4.a)$$

$$f(\text{GHz})_{\text{mnl}}^{\text{PMC}} = \sqrt{\left[\left(\frac{(l+1)\pi}{2d} \right)^2 + \left(\frac{n\pi}{a} \right)^2 + \left(\frac{m\pi}{b} \right)^2 \right]}, l=0,1,2,\dots, m=1,2,\dots, n=1,2,\dots \quad (4.b)$$

Table 1 shows the first resonance in a cavity with different dimensions and different dielectric materials, computed from the above formulas. For a homogenized cavity, the base dimensions of the cavity determine the first resonant frequency when the cover is PEC, but the height determines the first resonance frequency when the cover is PMC. In both cases, the height must be much smaller than the cavity base dimensions and smaller than a quarter of a wave length. It is in our interest to show results when the cavity is partially filled with dielectric substrate and the separation between the dielectric surface and the top is small. The results are shown in Table 1 for different separation

distances ranging from $2t$ (i.e. $h = 3$ mm) to $4t$ (i.e. $h = 5$ mm). We see that the size of the cavity base and the dielectric loading determines the first resonance for the PEC case, and again the cavity height and the permittivity determine the first resonance for the PMC case. It can also be seen that the resonance frequency decrease when the permittivity increases and when the separation between the substrate and the lid increases. The resonances for the PMC lid case are 3 to 5 times higher than those of the PEC case.

III. PMC PACKAGING EXAMPLES FOR MICROSTRIP CIRCUITS

First, we consider a simple 50Ω microstrip line as a two port device, and we use waveguide ports in CST in order to have perfect match to the microstrip line ports. We need this perfect match in order to get good accuracy in determining the reflection coefficient and associated transmission losses. The computational domain is bounded by the radiation box as suggested by the software developer. Thereafter, the PMC is added with different separations between the substrate surface and the PMC. Notice that the upper bound of the computational domain now is bounded by the PMC, and there is no need for any upper radiation boundary. However, the side walls of the computational domains are still bounded by what is suggested by the software developer. The computational domain is now limited between the ground plane and the PMC. This reduces the computational domain a lot. To make simple design guide, the separation distance will be related to the physical substrate thickness and transmission line width, but we have to keep in mind that this distance must be smaller than the quarter of a wavelength of the upper frequency to

Table 1: First resonance frequency in GHz of a cavity with PEC lid and PMC lid, with a substrate thickness $t=1$ mm

cavity base $a \times b$ (mm)	ε_1	h = 5 mm		h = 4 mm		h = 3 mm	
		PEC lid	PMC lid	PEC lid	PMC lid	PEC lid	PMC lid
50 x 50	1.0	4.243	15.588	4.243	19.224	4.243	25.357
	2.3	3.994	15.329	3.930	18.781	3.820	24.281
	10.2	3.832	14.274	3.724	16.525	3.538	18.982
50 x 60	1.0	3.905	15.588	3.905	19.224	3.905	25.357
	2.3	3.677	15.260	3.618	18.729	3.517	24.246
	10.2	3.528	14.224	3.429	16.497	3.258	18.970
60 x 60	1.0	3.536	15.588	3.536	19.224	3.536	25.357
	2.3	3.329	12.277	3.275	18.677	3.184	24.211
	10.2	3.195	14.182	3.106	16.469	2.951	18.956

make sure that the high order modes of the cavity will not be excited. Several parameters are considered such as the permittivity and thickness of the substrate.

a) Insertion losses: Here, we consider an example of a 20 mm long 50 Ω microstrip line with a substrate thickness $t = 0.635$ mm and two different relative permittivities of 10.2 and 6.15 and loss tangent 0.0027. The conductor is considered to be copper. The transmission coefficient S_{21} is shown versus frequency in Fig. 2 for three cases; open, with PEC at $4t$ from the substrate, and PMC. It can be seen that packaging eliminates the radiation losses which is large for the open case above 18 GHz. However, the PMC packaging provides smaller insertion losses than both the open and PEC cases. It can also be seen that higher permittivity cause larger insertion loss. It should be mentioned that based on [6], the microstrip line will have radiation losses if:

$$f \{GHz\} \times t \{mm\} > 2.14 \sqrt{\epsilon_r} \quad (5)$$

which corresponds to 10.8 GHz when the relative permittivity is 10.2 and 8.4 GHz when it is 6.15.

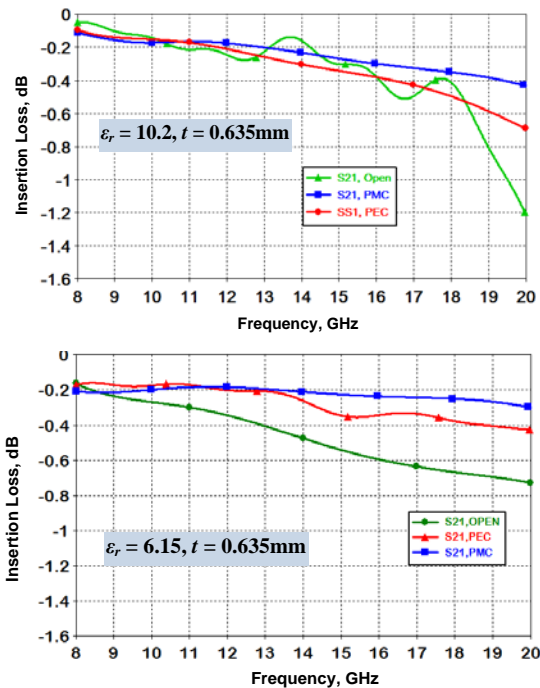


Fig. 2. Insertion losses of a straight microstrip line for different packaging cases, and for two different relative permittivities.

b) Characteristic Impedance: Figure 3 shows the variation of the characteristic impedance with frequency for the PMC lid located at different heights above the substrate. As expected, the characteristic impedance increases as the PMC lid gets closer to the line, because then the electric fields becomes more confined to the line so that its effective width is reduced. As such, the characteristic impedance increases since the characteristic impedance value is inversely proportional to the effective width of the microstrip line. The results indicate that a $3t$ to $4t$ air gap is sufficient to keep the characteristic impedance the same as the open case (no lid).

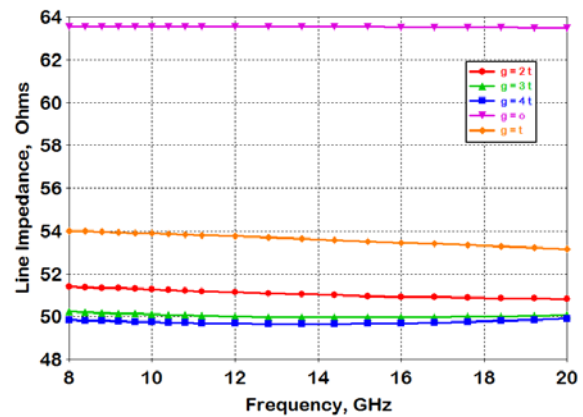


Fig. 3. Effect of the PMC lid on the characteristic impedance of the microstrip line, $g = h - t$.

c) Bended microstrip line: A microstrip line of 20 mm length and having a right angle bend is shown in Fig. 4a. The bend is mitered at the corner to reduce the effect of the discontinuity at the bend. It should be mentioned that physical microstrip line discontinuities can be designed for minimum reflections, but radiation losses are always inevitable. Here, two cases are considered. One with a thin substrate ($t = .25$ mm; $\epsilon_r = 2.2$, $w = .8$ mm) and the other with a thicker substrate ($t = 0.815$ mm; $\epsilon_r = 3.38$, $w = 1.85$ mm). Fig. 4b shows the comparison between the thin substrate case and the thick substrate case under open condition and also the thick substrate covered with PMC at $3h$. It can be seen that the PMC cover removed any kind of radiation loss and provides an overall better insertion loss, even for the open thin case.

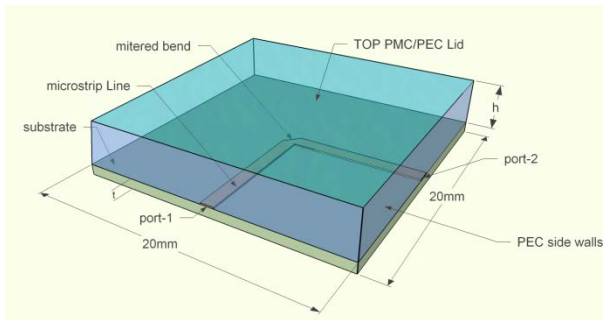


Fig.4(a). Bended microstrip line.

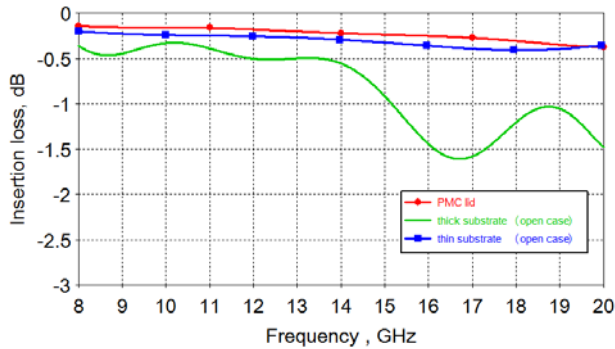


Fig. 4(b). Comparison between bended microstrip line on thin or thick substrates, open and with PMC lid 3t above substrate.

III. Realization of PMC Packaging

PMC is not a natural material so it has to be realized artificially. One method to realize the PMC lid is using a lid of periodic conducting nails [27] as shown in Fig. 5a. The artificially realized AMC surfaces have limited bandwidth, unlike the PEC that is a good approximation of conducting metal surfaces at all microwave frequencies. The lid of nails consists of nails connected to a solid ground plane which then is turned up-side-down. The magnetic surface appears at the open end of the nails, due to a transformation of the waves from the shorted end of the nails to the open end. The waves will in the nail layer propagate mainly along the nails, independent of the angle of arrival on the nails surface.

The pin structure is periodic, and therefore one cell can be analyzed by using the eigenmode solver of CST. The dispersion diagram of such an infinite periodic nail surface over a smooth metal surface is shown in Fig. 5b. We see that the structure is providing a stop band of parallel-plate modes (i.e. it is acting as an AMC surface) over a frequency band of 1:2. The S_{21} computed for a

right angle bended microstrip line covered by the lid of nails is shown in Fig. 5c. We see that the bandwidth is similar to the bandwidth obtained from the dispersion diagram. We, also, see that the losses are very close to the ideal PMC case. A parameter study of the stopband can be found in [7].

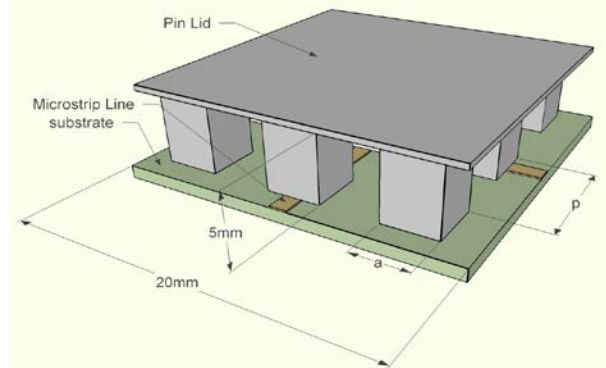


Fig. 5 (a). Geometry of the bended microstrip line in a cavity with metallic sidewalls and lid of nails.

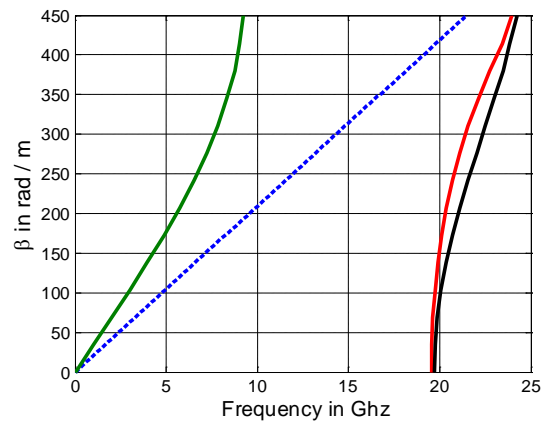


Fig. 5 (b). Dispersion diagram obtained for unit cell of periodic pin with $a = 3\text{mm}$ and $p = 6.75\text{mm}$.

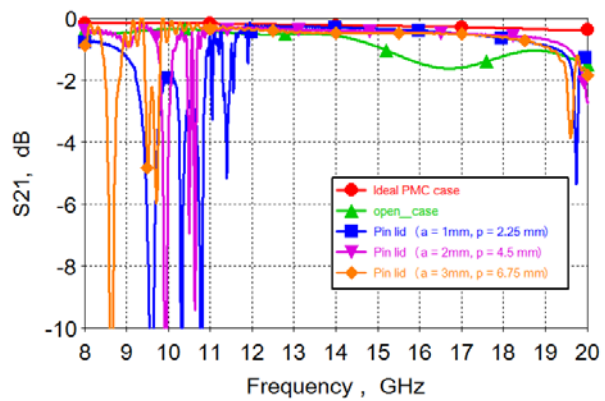


Fig. 5 (c). Simulated S_{21} of the right angle microstrip line with different a and the same a/p .

We now consider an example with an inhomogeneous nonrectangular cavity with the same right angle bended microstrip line, as shown in Fig. 6a. However, here the microstrip line is printed on a GaAs substrate with permittivity 12.9 and loss tangent 0.006 at 10 GHz, and thickness $t = 50 \mu\text{m}$. The 50Ω microstrip line has a width of $30 \mu\text{m}$. The dispersion diagram from one cell is shown in Fig. 6b. S_{21} versus frequency is shown in Fig. 6c. Figure 6c shows the performance of the three different cases; open, PEC lid, and PMC lid. We see that the PMC lid gives the smallest insertion loss, and the PEC lid curve shows some resonances within the frequency band.

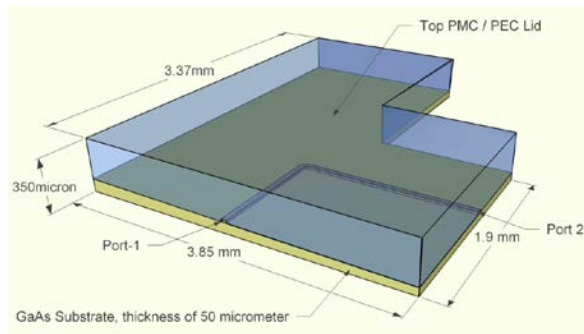


Fig. 6 (a). Geometry of the bended microstrip line in an inhomogenously filled nonrectangular cavity with metal.

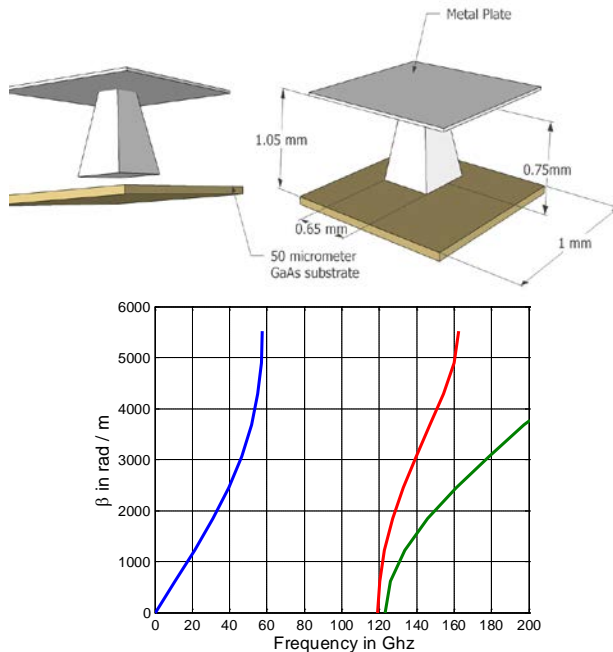


Fig. 6(b). Dispersion diagram obtained from the for one cell with inverted pyramidal-shaped pins that provide the wider bandwidth than the rectangular pins.

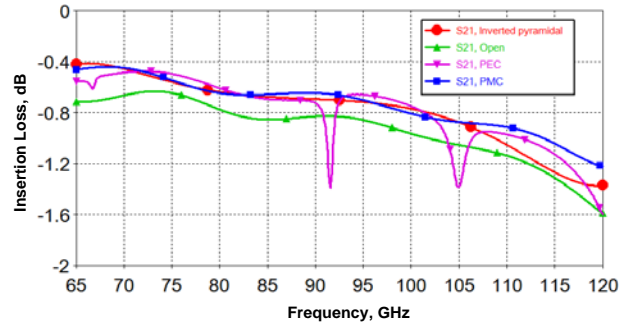


Fig. 6(c). S_{21} of the right angle microstrip line for the open case, PEC lid, PMC lid, and inverted pyramidal-shaped pin lid.

IV. Computation Summary

All the computations mentioned so far were done with CST Microwave Studio. Table 2 shows the number of mesh cells used for the different cases. For the PEC lid, PMC lid, and open case, we made a comparison based on the required number of cells. However, the open case needs matching layers, and the number of cells in this layer is not included in the number. CST does not provide the cell numbers in the matching layers that is actually five layers in the present case. Still, from the CPU time shown in Table 3, we see that the open case needs almost twice the CPU time of the PMC lid case when the PMC is at a height of $2t$.

Table 2: Comparison of mesh cell numbers for different simulation cases

Simulation case (Bended microstrip line)	Total Mesh cells
Open case (without matching layers)	258763
PMC lid (at a distance of t)	251550
PMC lid (at a distance of $2 \times t$)	301860
PEC lid (at a distance of $3 \times t$)	473616
Pin lid case ($a = 3\text{mm}$, $p = 6.75 \text{ mm}$)	773616

Table 3: Comparison of CPU time for different simulation cases

Simulation case (bended microstrip line)	Simulation time
PMC lid (at a distance of $2t$)	2 min 42 sec
PEC lid (at a distance of $3t$)	3 min 10 sec
Open (with 5 matching layers)	4 min 48 sec
Pin Lid ($a = 3$ mm, $p = 6.75$ mm)	7min 12 sec

V. PACKAGING OF PRACTICAL MICROSTRIP FILTER

As a proof of previously mentioned PMC and pin lid packaging concept, a 3rd order microstrip coupled line bandpass filter is manufactured as shown in Fig. 7a. Three cases are considered: open unpackaged case, smooth metal package case, and pin lid packaging case. Figure 7b shows the measurement results compared with the simulated ideal PMC case.

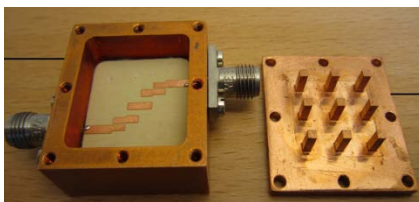


Fig. 7(a). Photo of the microstrip coupled line filter with the pin lid cover on the side.

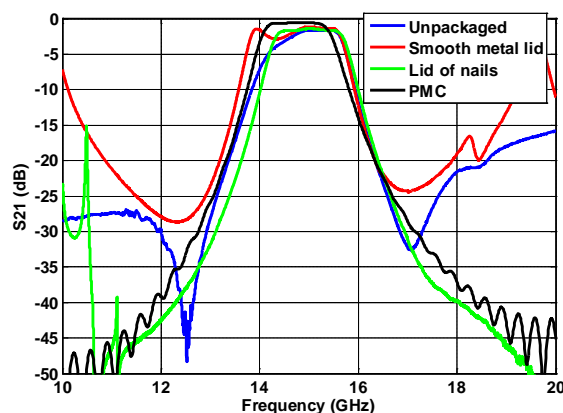


Fig. 7(b). The microstrip filter measurement response in three cases compared with the simulated PMC packaging case.

As seen from the measurement results of Fig. 7, ideal PMC and the pin lid packaging provide a

good filter response in the pass band and the rejection bands. On the other hand, for the open case and smooth metal lid case, the response of the filter is distorted within the pass band, which of course is not desired. The details of this work can be found in [24].

VI. CONCLUSION

An efficient method for the design of printed microstrip circuit with packaging in mind was presented. The results showed that the presented PMC prepackaging concept is more appropriate than PEC packaging regardless of the computational efficiency because of the wider bandwidth that can be provided by the PMC, and in particularly for packaging of large printed circuit boards. Engineers can use shorter time during the design process and optimize the circuit already from the start with the packaging in mind. After having designed with ideal PMC, the PMC can be realized by e.g. the bed of nails. This can be designed for a large stopband using simple design rules or the design curves in [10] to operate within the frequency band of interest. Larger stopband-widths can be achieved by using inverted pyramidal-shaped pins, or mushrooms (patches with via holes).

REFERENCES

- [1] Allen Taflove and Susan C. Hagness, "Computational Electrodynamics: The Finite-Difference Time-Domain Method," 3rd ed. Artech House Publishers, 2005.
- [2] Jianming Jin, "The Finite Element Method in Electromagnetics," 2nd ed. John Wiley and Sons, Inc., 2002.
- [3] D. R. Wilton and C. M. Butler, "Effective Methods for Solving Integral and Integro-Differential Equations," *Electromagnetics*, vol. 1, no. 3, pp. 289-308, 1981.
- [4] T. G. Moore, J. G. Blaschak, A. Taflove, and G. A. Kriegsmann, "Theory and Application of Radiation Boundary Operators", *Antennas and Propagation, IEEE Transactions on* 36, pp. 1797-1812, 2008.
- [5] J. Berenger, "A Perfectly Matched Layer for the Absorption of Electromagnetic Waves", *Journal of Computational Physics*, vol. 114, pp. 185-200, 1994.
- [6] J. B. Cole and D. Zhu, "Improved Version of the Second-Order MurAbsorbing Boundary Condition Based on a Nonstandard Finite Difference Model," *Applied Computational Electromagnetic Society*

- (ACES) Journal, vol. 24, no. 4, pp. 375-381, August 2009.
- [7] M. Wong and A. R. Sebak, "The Floating PML Applied to Practical FDTD Applications," *Applied Computational Electromagnetic Society (ACES) Journal*, vol. 23, no. 2, pp. 110-119, June 2008.
- [8] M. J. Inman, A. Z. Elsherbeni, J. G. Maloney, and B. N. Baker, "Practical Implementation of a CPML Absorbing Boundary for GPU Accelerated FDTD Technique," *Applied Computational Electromagnetic Society (ACES) Journal*, vol. 23, no. 1, pp. 16-22, March 2008.
- [9] P.-S. Kildal, E. Alfonso, A. Valero-Nogueira, and E. Rajo-Iglesias, "Local Metamaterial-Based Waveguides in Gaps Between Parallel Metal Plates", *IEEE Antennas and Wireless Propagation Letters (AWPL)*, vol. 8, pp. 84-87, 2009.
- [10] E. Rajo-Iglesias and P.-S. Kildal, "Numerical Studies of Bandwidth of Parallel Plate Cut-Off Realized By Bed of Nails, Corrugations and Mushroom-Type EBG for Use in Gap Waveguides", *IET Microw Antennas Propag.*, vol. 5, no. 3, pp. 282-289, March 2011.
- [11] E. Rajo-Iglesias, A. Uz Zaman, and P.-S. Kildal, "Parallel Plate Cavity Mode Suppression in Microstrip Circuit Packages Using a Lid of Nails", *IEEE Microwave and Wireless Components Letters*, vol. 20, no. 1, pp. 31-33, Dec. 2009.
- [12] P.-S. Kildal, "Artificially Soft and Hard Surfaces in Electromagnetics," *IEEE Trans. Antennas Propagat.*, vol. 38, pp. 1537-1544, Oct. 1990.
- [13] P.-S. Kildal, A. Kishk, and A. Tengs, "Reduction of Forward Scattering from Cylindrical Objects Using Hard Surfaces," *IEEE Trans. Antennas Propagat.*, vol. 44, pp. 1509-1520, Nov. 1996.
- [14] P.-S. Kildal and A. Kishk, "EM Modeling of Surfaces with STOP or GO Characteristics - Artificial Magnetic Conductors and Soft and Hard Surfaces," *Applied Computational Electromagnetics Society (ACES) Journal*, vol. 18, pp. 32-40, Mar. 2003.
- [15] Y. Rahmat-Samii, "The Marvels of Electromagnetic Band Gap (EBG) Structures," *Applied Computational Electromagnetic Society (ACES) Journal*, vol. 18, no. 3, pp. 1-10, November 2003.
- [16] P.-S. Kildal, A. A. Kishk, and S. Maci, "Special Issue on Artificial Magnetic Conductors, Soft/Hard Surfaces, and Other Complex Surfaces" (Guest Editorial), *IEEE Transactions on Antennas and Propagation*, vol. 53, pp. 2-7, Jan. 2005.
- [17] P.-S. Kildal, A. Kishk, M. Bosiljevac, and Z. Sipus, "The PMC-Amended DB Boundary - A Canonical EBG Surface", *Applied Computational Electromagnetics Society (ACES) Journal*, vol. 26, no. 2, Feb. 2011.
- [18] P.-S. Kildal, A. Uz Zaman, E. Rajo-Iglesias, E. Alfonso, and A. Valero-Nogueira, "Design and Experimental Verification of Ridge Gap Waveguides in Bed of Nails for Parallel Plate Mode Suppression", *IET Microw Antennas Propag.*, vol. 5, no. 3, pp. 262-270, March 2011.
- [19] M. Bosiljevac, Z. Sipus, and P. -S. Kildal, "Construction of Green's Functions of Parallel Plates with Periodic Texture with Application to Gap Waveguides - A Plane Wave Spectral Domain Approach", *IET Microw Antennas Propag.*, vol. 4, iss. 11, pp. 1799-1810, Nov. 2010.
- [20] A. Polemi, S. Maci, and P. -S. Kildal, "Dispersion Characteristics of Metamaterial-Based Parallel-Plate Ridge Gap Waveguide Realized by Bed of Nails", *IEEE Transactions on Antennas and Propagation*, vol. 59, no. 3, pp. 904-913, March 2011.
- [21] A. Polemi and S. Maci, "Closed Form Expressions for the Modal Dispersion Equations and for the Characteristic Impedance of a Metamaterial Based Gap Waveguide", *IET Microw Antennas Propag.*, vol. 4, iss. 8, pp. 1073-1080, August 2010.
- [22] P. -S. Kildal, "Three Metamaterial-based Gap Waveguides Between Parallel Metal Plates for mm/submm Waves", *3rd European Conference on Antennas and Propagation (EuCAP2009)*, Berlin, 23-27 March 2009.
- [23] E. O. Hammerstad and F. Bekkadal (1975) *Microstrip Handbook*, Trondheim: Norwegian Institute of Technology, Report ELAB STF44 A74169.
- [24] F. Gardiol, *Microstrip Circuits*. Jon Wiley & Sons, Inc 1994.
- [25] www.cst.com.
- [26] R. F. Harrington, *Time-Harmonic Electromagnetic Fields*, McGraw-Hill, 1961.
- [27] M. G. Silveirinha, C. A. Fernandes, and J. R. Costa, "Electromagnetic Characterization of Textured Surfaces Formed by Metallic Pins", *IEEE Trans. Antennas Propagat.*, vol. 56, no. 2, pp. 405-415, Feb. 2008
- [28] A. A. Brazález, A. U. Zaman, and P. -S. Kildal, "Improved Microstrip Filters using PMC Packaging by Lid of Nails," Accepted for publication in *IEEE Trans. On Components, Packaging and Manufacturing Technology*.



Ahmed A. Kishk received Ph.D. degree in Electrical Engineering from University of Manitoba, Canada in 1986. He is now a Professor at the Department of Electrical and Computer Engineering of Concordia University, Montreal, Canada. He is

an Editor of *Antennas & Propagation Magazine*. His research interest includes the areas of millimeter frequency antennas, dielectric resonator antennas, printed antennas, EBG, artificial magnetic conductors, soft and hard surfaces, and phased array antennas. He has published over 220-refereed Journal articles and 27 book chapters and over 380 conference papers. He is a recipient of several regional and international awards.



Ashraf Uz Zaman was born in Chittagong, Bangladesh. He received his BSc. in Electrical and Electrical Engineering from Chittagong University of Engineering and Technology, Bangladesh. In 2007, he received his M.Sc. degree from Chalmers University of Technology, Sweden. At present, he is with the Communication, Information Theory and Antenna division of same university and is working towards his Ph.D. His main research interest includes millimeter and sub millimeter waveguide technology, frequency selective surfaces, microwave passive components, integration of MMIC with the antennas etc.



Per-Simon Kildal has been Professor at Chalmers University of Technology, Gothenburg, Sweden since 1989 (www.kildal.se). He has authored antenna textbook, and more than 110 journal articles and letters in IEEE or IET journals, two of which have received best paper awards. Kildal has designed two very large antennas, including the Gregorian dual-reflector feed of Arecibo radiotelescope. He has invented several reflector antenna feeds, the latest being the so-called “Eleven antenna”. He is the originator of the concept of soft and hard surfaces. Kildal’s research group has pioneered the reverberation chamber as an accurate measurement tool for antennas and wireless terminals subjected to Rayleigh fading. Professor Kildal also received the Distinguished Achievements Award of the IEEE Antennas and Propagation Society in 2011.

Generalized Formulation for the Scattering from a Ferromagnetic Microwire

Ahmed M. Attiya and Majeed A. Alkanhal

Electrical Engineering Dept.
King Saud University, Riyadh, 11421, P.O.Box 800, Saudi Arabia
aattiya@ksu.edu.sa, majeed@ksu.edu.sa

Abstract — In this paper, we present a full wave analysis for the scattering of an obliquely incident plane wave of an arbitrary polarization angle due to an infinite magnetized ferromagnetic microwire. The analysis is based on expanding the incident and scattered waves as infinite sets of cylindrical waves and matching the corresponding modes on the surface of the microwire to obtain the unknown amplitudes of the scattered fields. The gyromagnetic properties of the ferromagnetic material introduce a coupling between the electric and magnetic field components inside the microwire. This coupling is the reason of cross polarization in the scattered field.

Index Terms: Analytical techniques, ferrites, ferromagnetic microwires, scattering.

I. INTRODUCTION

Ferromagnetic microwires based on amorphous ferromagnetic alloy compositions have gained a significant interest in RF and microwave applications due to their unique electromagnetic properties and the feasibility of simple fabrication and manufacturing process [1-2]. These ferromagnetic materials are characterized by high electrical conductivity, ferromagnetic resonance, gyromagnetic properties, and tunable characteristics. These properties make ferromagnetic microwires to be good candidates for different applications in microwave range including synthesizing artificial double negative metamaterials, shielding materials, and absorbing materials [3-5]. Another similar configuration for synthesizing double negative metamaterial is based on an array of conducting wires embedded

inside a ferromagnetic host [6]. Tuning properties of ferromagnetic microwires make them suitable to obtain tunable synthetic materials [7-11]. This can also be used to design microwave sensing tools like stress sensors [10]. In addition, it may be also expected to obtain polarization rotation from these ferromagnetic materials due to their gyromagnetic properties. This polarization rotation can introduce an additional feature which may be useful to other applications like electromagnetic polarizer or radar cross section reduction.

These unique properties of ferromagnetic microwires were the motivation for different authors to introduce different techniques for modeling the electromagnetic wave interaction with these microwires. Effective medium properties and magneto-impedance are used to obtain simple analytical expressions for the equivalent effective parameters of ferromagnetic microwire composites [11]. Other numerical techniques like TLM and FDTD can also be used to present a numerical analysis for the scattering from general gyrotropic media [12-13]. However, the small diameter of the ferro-magnetic microwire represents a significant computational challenge in these numerical methods. More recently, Liberal *et al* [14-15] introduced a full wave analysis for the scattering of an infinite ferromagnetic microwire and an infinite array of these microwires. Their analysis is based on expanding the incident and scattered waves as superpositions of cylindrical waves. The unknown amplitudes of the scattered fields are obtained by applying the boundary conditions on the surface of the microwire. They also extended their analysis to study the scattering of a ferromagnetic

microwire inside a rectangular waveguide and verified their analysis with experimental results. The advantage of this analysis is that it is full wave analysis which includes all the parameters of the ferromagnetic microwire without introducing approximation. Liberal *et al* [14-15] showed that this analysis cannot be obtained by other numerical techniques like method of moments or finite difference time domain due to the complicated properties of the ferromagnetic materials combined with the very small radius of the microwire.

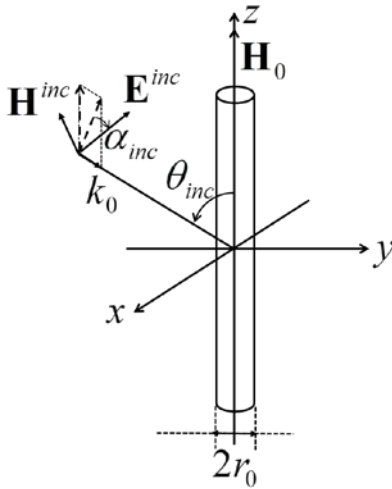


Fig. 1. Geometry of the problem.

However, the analysis of Liberal *et al* [14-15] was limited only for the case of normal incidence on the microwire with an electric field polarization parallel to its axis. For the mentioned applications of ferromagnetic microwires, it may be required to have a general insight of the electromagnetic wave interaction with ferromagnetic microwire at different angles of incidence and different polarization. This was the motivation here to extend their analysis for the case of the scattering from a ferromagnetic microwire due to an obliquely incident plane wave of an arbitrary polarization as shown in Fig. 1. The main difference in this case is coupling between the electric and magnetic field components in the ferromagnetic material due to its gyromagnetic properties. This coupling vanishes completely for normal incidence. Thus, this property is not included in the analysis of Liberal *et al* [14-15]. The resulting wave equation inside the

ferromagnetic microwire in this case is represented as a fourth order differential equation as shown in the analysis in the following section. This is similar to the problem of electromagnetic wave interaction with ferrite material in closed and open waveguides which was studied by different authors [16-19].

In the following section, we present the analysis of the problem. In Section 3, sample results for the scattering of two different ferromagnetic microwires are presented for different angle of incidence and different polarization angles. Then concluding remarks are discussed.

II. THEORY AND ANALYSIS

In the region $\rho \geq a_0$ outside the microwire, the incident plane wave and scattered fields along the longitudinal direction of the wire can be represented as a combination of inward and outward cylindrical functions as follows:

$$E_z^{inc} = (E_0 \sin \theta_{inc} \cos \alpha_{inc}) \sum_{n=-\infty}^{\infty} j^n J_n(\beta_{\rho 0} \rho) e^{-j\beta_z z} e^{-jn\phi}, \quad (1-a)$$

$$H_z^{inc} = \left(\frac{E_0}{Z_0} \sin \theta_{inc} \sin \alpha_{inc} \right) \sum_{n=-\infty}^{\infty} j^n J_n(\beta_{\rho 0} \rho) e^{-j\beta_z z} e^{-jn\phi}, \quad (1-b)$$

$$E_z^s = (E_0 \sin \theta_{inc}) \sum_{n=-\infty}^{\infty} C_n H_n^{(2)}(\beta_{\rho 0} \rho) e^{-j\beta_z z} e^{-jn\phi}, \quad (2-a)$$

$$H_z^s = \left(\frac{E_0}{Z_0} \sin \theta_{inc} \right) \sum_{n=-\infty}^{\infty} D_n H_n^{(2)}(\beta_{\rho 0} \rho) e^{-j\beta_z z} e^{-jn\phi}, \quad (2-b)$$

where $\beta_z = k_0 \cos \theta_{inc}$ is the longitudinal propagation constant and $\beta_{\rho 0} = k_0 \sin \theta_{inc}$ is the radial propagation constant. The amplitude of the incident field is assumed to be unity such that $E_0 = 1V/m$. It should be noted that the polarization angle of the scattered is included in the unknown amplitudes of the scattered electric and magnetic fields, C_n and D_n , respectively.

The transverse field components can be obtained in terms of the longitudinal field components. For the present case, we are interested in the ϕ components of the electric and magnetic fields to be applied in the tangential boundary conditions on the microwire. These ϕ components can be presented in terms of the longitudinal field components as follows:

$$E_\phi = \left(-\frac{j\beta_z}{\beta_{\rho 0}^2} \frac{1}{\rho} \frac{\partial E_z}{\partial \phi} + \frac{j\omega\mu_0}{\beta_{\rho 0}^2} \frac{\partial H_z}{\partial \rho} \right), \quad (3-a)$$

$$H_\phi = \left(-\frac{j\omega\varepsilon_0}{\beta_{\rho 0}^2} \frac{\partial E_z}{\partial \rho} - \frac{j\beta_z}{\beta_{\rho 0}^2} \frac{1}{\rho} \frac{\partial H_z}{\partial \phi} \right). \quad (3-b)$$

By applying (3) into (1) and (2), the incident and scattered ϕ field components are obtained as:

$$E_\phi^{inc} = -E_0 \frac{n \cos \theta_{inc} \cos \alpha_{inc}}{k_0 \rho \sin \theta_{inc}} \sum_{n=-\infty}^{\infty} j^n J_n(\beta_{\rho 0} \rho) e^{-j\beta_z z} e^{-jn\phi} \\ + jE_0 \sin \alpha_{inc} \sum_{n=-\infty}^{\infty} j^n J'_n(\beta_{\rho 0} \rho) e^{-j\beta_z z} e^{-jn\phi}, \quad (4-a)$$

$$H_\phi^{inc} = -j \frac{E_0}{Z_0} \cos \alpha_{inc} \sum_{n=-\infty}^{\infty} j^n J'_n(\beta_{\rho 0} \rho) e^{-j\beta_z z} e^{-jn\phi} \\ - \frac{E_0}{Z_0} \frac{n \cos \theta_{inc} \sin \alpha_{inc}}{k_0 \rho \sin \theta_{inc}} \sum_{n=-\infty}^{\infty} j^n J_n(\beta_{\rho 0} \rho) e^{-j\beta_z z} e^{-jn\phi}, \quad (4-b)$$

$$E_\phi^s = -E_0 \frac{n \cos \theta_{inc}}{k_0 \rho \sin \theta_{inc}} \sum_{n=-\infty}^{\infty} C_n H_n^{(2)}(\beta_{\rho 0} \rho) e^{-j\beta_z z} e^{-jn\phi} \\ + jE_0 \sum_{n=-\infty}^{\infty} D_n H_n^{(2)}(\beta_{\rho 0} \rho) e^{-j\beta_z z} e^{-jn\phi}, \quad (4-c)$$

$$H_\phi^s = -j \frac{E_0}{Z_0} \sum_{n=-\infty}^{\infty} C_n H_n^{(2)}(\beta_{\rho 0} \rho) e^{-j\beta_z z} e^{-jn\phi} \\ - \frac{E_0}{Z_0} \frac{n \cos \theta_{inc}}{k_0 \rho \sin \theta_{inc}} \sum_{n=-\infty}^{\infty} D_n H_n^{(2)}(\beta_{\rho 0} \rho) e^{-j\beta_z z} e^{-jn\phi}. \quad (4-d)$$

On the other hand, the fields inside the ferromagnetic microwire biased by a dc magnetic field along its axis at $\rho \leq a_0$ are related as:

$$\frac{1}{\rho} \frac{\partial E_z}{\partial \phi} - \frac{\partial E_\phi}{\partial z} = -j\omega\mu H_\rho + \omega\kappa H_\phi, \quad (5-a)$$

$$\frac{\partial E_\rho}{\partial z} - \frac{\partial E_z}{\partial \rho} = -j\omega\mu H_\phi - \omega\kappa H_\rho, \quad (5-b)$$

$$\frac{1}{\rho} \frac{\partial(\rho E_\phi)}{\partial \rho} - \frac{1}{\rho} \frac{\partial E_\rho}{\partial \phi} = -j\omega\mu_0 H_z, \quad (5-c)$$

$$\frac{1}{\rho} \frac{\partial H_z}{\partial \phi} - \frac{\partial H_\phi}{\partial z} = j\omega \left(\varepsilon_0 - j \frac{\sigma}{\omega} \right) E_\rho, \quad (5-d)$$

$$\frac{\partial H_\rho}{\partial z} - \frac{\partial H_z}{\partial \rho} = j\omega \left(\varepsilon_0 - j \frac{\sigma}{\omega} \right) E_\phi, \quad (5-e)$$

$$\frac{1}{\rho} \frac{\partial(\rho H_\phi)}{\partial \rho} - \frac{1}{\rho} \frac{\partial H_\rho}{\partial \phi} = j\omega \left(\varepsilon_0 - j \frac{\sigma}{\omega} \right) E_z, \quad (5-f)$$

where μ and κ are the elements of the permeability tensor of the ferromagnetic material and σ is its electrical conductivity. The parameters of ferromagnetic materials are given by [14-15]:

$$\mu = \mu_0 \\ + \mu_0 \left(\frac{\omega_0 \omega_m (\omega_0^2 - \omega^2 (1 - \alpha^2)) - j\alpha \omega \omega_m (\omega_0^2 + \omega^2 (1 + \alpha^2))}{[\omega_0^2 - \omega^2 (1 + \alpha^2)]^2 + 4\omega_0^2 \omega^2 \alpha^2} \right) \quad (6-a)$$

$$k = \mu_0 \left(\frac{\omega \omega_m (\omega_0^2 - \omega^2 (1 + \alpha^2)) - j2\omega_0 \omega_m \omega^2 \alpha}{[\omega_0^2 - \omega^2 (1 + \alpha^2)]^2 + 4\omega_0^2 \omega^2 \alpha^2} \right), \quad (6-b)$$

where $f_0 = \omega_0 / 2\pi$ is the Larmor frequency, $f_m = \omega_m / 2\pi$ is the resonance frequency at the saturation limit and α is a dimensionless damping factor.

It should be noted that the longitudinal dependence of the field components inside the microwire is the same as outside the microwire to satisfy the tangential propagation boundary condition. Thus, the field dependence inside the microwire is also $e^{-j\beta_z z}$ where $\beta_z = k_0 \cos \theta_{inc}$ is the same as in the free space surrounding the microwire.

The transverse field components inside the ferromagnetic microwire can be obtained in terms of the longitudinal field components as follows:

$$E_\rho = \frac{1}{D} \left(a \frac{\partial E_z}{\partial \rho} + b \frac{1}{\rho} \frac{\partial E_z}{\partial \phi} - e \frac{\partial H_z}{\partial \rho} - d \frac{1}{\rho} \frac{\partial H_z}{\partial \phi} \right), \quad (7-a)$$

$$E_\phi = \frac{1}{D} \left(-b \frac{\partial E_z}{\partial \rho} + a \frac{1}{\rho} \frac{\partial E_z}{\partial \phi} + d \frac{\partial H_z}{\partial \rho} - e \frac{1}{\rho} \frac{\partial H_z}{\partial \phi} \right), \quad (7-b)$$

$$H_\rho = \frac{1}{D} \left(b \frac{\omega\varepsilon}{\beta_z} \frac{\partial E_z}{\partial \rho} - a \frac{\omega\varepsilon}{\beta_z} \frac{1}{\rho} \frac{\partial E_z}{\partial \phi} + a \frac{\partial H_z}{\partial \rho} + b \frac{1}{\rho} \frac{\partial H_z}{\partial \phi} \right) \quad (7-c)$$

$$H_\phi = \frac{1}{D} \left(a \frac{\omega\varepsilon}{\beta_z} \frac{\partial E_z}{\partial \rho} + b \frac{\omega\varepsilon}{\beta_z} \frac{1}{\rho} \frac{\partial E_z}{\partial \phi} - b \frac{\partial H_z}{\partial \rho} + a \frac{1}{\rho} \frac{\partial H_z}{\partial \phi} \right) \quad (7-d)$$

where

$$a = j\beta_z \beta_\rho^2, \quad (8-a)$$

$$b = \omega^2 \kappa \beta_z \left(\varepsilon_0 - j \frac{\sigma}{\omega} \right), \quad (8-b)$$

$$d = -j\omega\mu \left(\beta_\rho^2 - \frac{\omega^2 \kappa^2}{\mu} \left(\varepsilon_0 - j \frac{\sigma}{\omega} \right) \right), \quad (8-c)$$

$$e = \omega\kappa\beta_z^2, \quad (8-d)$$

$$D = (\omega^2 \kappa \varepsilon)^2 - \beta_\rho^4, \quad (8-e)$$

$$\beta_\rho = \sqrt{\omega^2 \mu \left(\varepsilon_0 - j \frac{\sigma}{\omega} \right) - \beta_z^2}. \quad (8-f)$$

By inserting Eq. (7) with the definitions of Eq. (8) into Eq. (5), one can obtain two coupled wave

equations of the longitudinal field components as follows [16-17]:

$$\nabla_t^2 E_z + c_1 E_z - j d_1 H_z = 0, \quad (9-a)$$

$$\nabla_t^2 H_z + f_1 H_z + j g_1 E_z = 0, \quad (9-b)$$

where

$$c_1 = \left(\beta_{\rho 1}^2 - \frac{\omega^2 \kappa^2}{\mu} \left(\varepsilon_0 - j \frac{\sigma}{\omega} \right) \right), \quad (10-a)$$

$$d_1 = \frac{\mu_0 \omega \kappa \beta_z}{\mu}, \quad (10-b)$$

$$f_1 = \frac{\mu_0 \beta_\rho^2}{\mu}, \quad (10-c)$$

$$g_1 = \frac{\omega \kappa \beta_z}{\mu} \left(\varepsilon_0 - j \frac{\sigma}{\omega} \right). \quad (10-d)$$

It should be noted that the coupling between the longitudinal electric and magnetic field components vanishes for the case of normal incidence where $\beta_z = 0$. These two coupled wave equations can be represented as two decoupled fourth order differential equation as follows:

$$\left(\nabla_t^2 \nabla_t^2 + (f_1 + c_1) \nabla_t^2 + f_1 c_1 - d_1 g_1 \right) \Psi_z = 0, \quad (11)$$

where Ψ_z is either E_z or H_z . This fourth order differential equation can be represented as a multiplication of two wave equations of different propagation constants as follows:

$$\left(\nabla_t^2 + \gamma_{\rho 1}^2 \right) \left(\nabla_t^2 + \gamma_{\rho 2}^2 \right) \Psi_z = 0, \quad (12-a)$$

where the two propagation constants are:

$$\gamma_{\rho 1/2} = \sqrt{\frac{1}{2} \left((f_1 + c_1) \pm \sqrt{(f_1 - c_1)^2 + 4d_1 g_1} \right)}. \quad (12-b)$$

The general solution of Eq. (12) for the longitudinal electric field inside the microwire in terms of cylindrical waves is [16-17]:

$$E_z^i = \sum_{n=-\infty}^{\infty} \left(A_n J_n(\gamma_{\rho 1} \rho) + B_n J_n(\gamma_{\rho 2} \rho) \right) e^{-jn\phi} e^{-j\beta_z z}. \quad (13-a)$$

A similar solution can be obtained for the longitudinal magnetic field. The unknown amplitudes of the longitudinal magnetic field can be related to the corresponding ones of the longitudinal electric field by inserting Eq. (13-a) into Eq. (9-b). Thus, the general solution of the longitudinal magnetic field component in terms of the unknown amplitudes of the longitudinal electric field component is given by:

$$H_z^i = \sum_{n=-\infty}^{\infty} \left(\eta_1 A_n J_n(\gamma_{\rho 1} \rho) + \eta_2 B_n J_n(\gamma_{\rho 2} \rho) \right) e^{-jn\phi} e^{-j\beta_z z}, \quad (13-b)$$

where the coupling coefficients between the longitudinal electric and magnetic field components are given by:

$$\eta_{1/2} = \frac{j g_1}{\gamma_{\rho 1/2}^2 - f_1}. \quad (14)$$

By inserting Eq. (13) into Eqs. (7-b) and (7-d), one can obtain the ϕ components of the electric and magnetic fields inside the microwire as:

$$E_\phi^i = \sum_{n=-\infty}^{\infty} \left[A_n X_{1n}(\rho) + B_n X_{2n}(\rho) \right] e^{-jn\phi} e^{-j\beta_z z}, \quad (15-a)$$

$$H_\phi^i = \sum_{n=-\infty}^{\infty} \left[A_n \Lambda_{1n}(\rho) + B_n \Lambda_{2n}(\rho) \right] e^{-jn\phi} e^{-j\beta_z z}, \quad (15-b)$$

where

$$X_{in}(\rho) = \frac{1}{D} \left(d \eta_i \gamma_{\rho i} - b \gamma_{\rho i} \right) J_n'(\gamma_{\rho i} \rho) + \frac{1}{D} \frac{j n (e \eta_i - a)}{\rho} J_n(\gamma_{\rho i} \rho), \quad (16-a)$$

$$\Lambda_{in}(\rho) = \frac{1}{D} \left(a \gamma_{\rho i} \frac{\omega}{\beta_z} \left(\varepsilon_0 - j \frac{\sigma}{\omega} \right) - b \gamma_{\rho i} \eta_i \right) J_n'(\gamma_{\rho i} \rho) - j \frac{1}{D} \frac{n}{\rho} \left(a \eta_i + b \frac{\omega}{\beta_z} \left(\varepsilon_0 - j \frac{\sigma}{\omega} \right) \right) J_n(\gamma_{\rho i} \rho). \quad (16-b)$$

“ i ” here stands for either 1 or 2. By applying the boundary conditions of the tangential field components at the boundary of the microwire one can obtain a linear system of equations for each cylindrical wave mode “ n ” to obtain the corresponding unknown field amplitudes as shown in Eq. 17 below.

By solving the above system of equation one can obtain the unknown amplitudes of the scattered and penetrated field components. For a very thin wire compared with the free space wave length as in the present case of the microwire, the zero-order cylindrical wave is the dominant mode. The amplitudes of the other modes are much smaller such that they can be ignored compared with the amplitudes of the zero-order mode [14].

$$\begin{bmatrix}
J_n(\gamma_{\rho 1} a_0) & J_n(\gamma_{\rho 2} a_0) & -\sin \theta_0 H_n^{(2)}(\beta_{\rho 0} a_0) & 0 \\
Z_0 \eta_1 J_n(\gamma_{\rho 1} a_0) & Z_0 \eta_2 J_n(\gamma_{\rho 1} a_0) & 0 & -\sin \theta_0 H_n^{(2)}(\beta_{\rho 0} a_0) \\
k_0 a_0 \sin \theta_0 X_{1n}(a_0) & k_0 a_0 \sin \theta_0 X_{2n}(a_0) & n \cos \theta_0 H_n^{(2)}(\beta_{\rho 0} a_0) & -jk_0 a_0 \sin \theta_0 H_n'^{(2)}(\beta_{\rho 0} a_0) \\
Z_0 k_0 a_0 \sin \theta_0 \Lambda_{1n}(a_0) & Z_0 k_0 a_0 \sin \theta_0 \Lambda_{2n}(a_0) & jk_0 a_0 \sin \theta_0 H_n'^{(2)}(\beta_{\rho 0} a_0) & n \cos \theta_0 H_n^{(2)}(\beta_{\rho 0} a_0)
\end{bmatrix}
\begin{bmatrix}
A_n \\
B_n \\
C_n \\
D_n
\end{bmatrix}
=
\begin{bmatrix}
j^n \sin \theta_{inc} \cos \alpha_{inc} J_n(\beta_{\rho 0} a_0) \\
j^n \sin \theta_{inc} \sin \alpha_{inc} J_n(\beta_{\rho 0} a_0) \\
-n \cos \theta_{inc} \cos \alpha_{inc} j^n J_n(\beta_{\rho 0} a_0) + k_0 a_0 \sin \theta_{inc} \sin \alpha_{inc} j^{n+1} J_n'(\beta_{\rho 0} a_0) \\
-j^{n+1} k_0 a_0 \sin \theta_{inc} \cos \alpha_{inc} J_n'(\beta_{\rho 0} a_0) - j^n n \cos \theta_{inc} \sin \alpha_{inc} J_n(\beta_{\rho 0} a_0)
\end{bmatrix}. \quad (17)$$

Thus, we are concentrating only on C_0 and D_0 in the results shown in the following section.

III. RESULTS AND DISCUSSIONS

In this section, we present sample results for the scattering of two ferromagnetic microwires at different angles of incidence and different polarization angles. The ferromagnetic material is assumed to be $(\text{Co}_{0.94}\text{Fe}_{0.06})_{75}\text{Si}_{12.5}\text{B}_{12.5}$. The parameters of this ferromagnetic material are [14-15] $f_0 = \omega_0 / 2\pi = 5.666$ GHz, $\alpha = 0.02$ and $f_m = \omega_m / 2\pi = 11.642$ GHz.

For ferromagnetic materials, there are two main mechanisms for electromagnetic wave propagation, namely along the dc magnetization biasing or perpendicular to it [20]. For the former mechanism, the plane wave can be presented a superposition of two oppositely circular polarized waves. One of them has an equivalent permeability $\mu + k$ while the other has an equivalent permeability $\mu - k$. The first circular polarization has a resonance at Larmor frequency while the second circular polarization does not have any resonance effect. On the other hand, for the case of electromagnetic wave propagation which is perpendicular to the dc magnetic biasing while its electric field is parallel to the dc magnetic biasing, the equivalent permeability is $\mu_e = (\mu^2 - k^2) / \mu$. This case is known as an extra ordinary wave [20]. The equivalent permeability in this case has a resonance frequency at 9.9 GHz for the present ferromagnetic material. The final case, where both the propagation direction and the electric field polarization are perpendicular to the dc magnetic biasing, the equivalent permeability is the permeability of free space. Thus, for the present material we have two resonance

frequencies, Larmor resonance frequency at 5.666 GHz and extra ordinary wave resonance at 9.9 GHz.

The following results shown in Figures 2 to 5 present the amplitudes of the zero-order modes of the scattered fields as functions of frequency f and angle of incidence θ_{inc} for different polarization angles α_{inc} . The radius of the microwire in Figs. 2 and 3 is $45 \mu\text{m}$ while the corresponding one in Figs. 4 and 5 is $4 \mu\text{m}$. It can be noted that only the resonance effect of extra ordinary wave is detected in the amplitudes of the scattered fields. For the case of $\alpha_{inc} = 0^\circ$, the incident field is pure TM wave. Thus, D_0 in this case corresponds to the amplitude of a cross polarized component of the scattered field. The resonance behavior in this case appears as a minimum in the amplitude of the co-polarized scattered field and as a maximum in the amplitude of the cross-polarized field component. It can be noted that the cross polarized component vanishes completely for normal incidence while it has a peak at θ_{inc} in the range from 40° to 60° depending on the frequency and the radius of the microwire.

For the case of a polarization angle $\alpha_{inc} = 45^\circ$, the main characteristics of the reflected E_z component is the same as in the case of the pure TM wave. However, the amplitude of C_0 is decreased in this case by nearly a factor of $\cos \alpha_{inc}$. On the other hand, the amplitude of D_0 is monotonically increased with frequency and angle of incidence for the case of the thick microwire while it is nearly not affected for the thin microwire.

Finally, for the case of a polarization angle $\alpha_{inc} = 90^\circ$ where the incident wave represents pure TE wave, the amplitude of D_0 is the co-polarized component of the scattered field while C_0 is the cross-polarized component. It can be noted that in this case the co-polarized component is not characterized by any resonance behavior. However, for the thick microwire, the results show a resonance behavior at a cross-polarized component around the resonance frequency of extra ordinary wave. This resonance behavior is nearly negligible in the case of the thin microwire. It can also be noted that the cross polarized component vanishes completely in normal incidence as in the case of TM incident wave.

From these results, it can be concluded that the scattering of magnetized ferromagnetic microwire introduces a cross polarized component for oblique incidence and the frequency response of the scattered field is mainly characterized by a resonance effect around the resonance frequency of extra ordinary waves in most cases for both co-polarized and cross-polarized components.

IV. CONCLUSION

In this paper, we presented a full wave analysis for the scattering of an obliquely incident plane wave of an arbitrary polarization angle due to an infinite magnetized ferromagnetic microwire. The present analysis represents a generalization for a previously published analysis based on only normal incidence TM wave. The main difference in the present case lies in the coupling between the electric and magnetic field components due to the gyromagnetic properties of the ferromagnetic microwire. This field coupling introduces cross polarized component in the scattered field. This cross polarized component vanishes completely for the case of normal incidence. The scattered field components are mainly characterized by resonance effects close to the resonance of extra ordinary wave in most cases for both co-polarized and cross-polarized components.

ACKNOWLEDGMENT

This work was supported by The Research Center – College of Engineering – King Saud University.

REFERENCES

- [1] D. Y.-Jiang, J. J.-Jun, D. Gang, T. Bin, B. S.-Wei, and H. H.-Hui, "Magnetic and Microwave Properties of Glass-Coated Amorphous Ferromagnetic Microwires", *Trans. Nonferrous Met. Soc. China*, vol. 17, pp. 1352-1357, 2007.
- [2] F. X. Qin, H. X. Peng, L. V. Panina, M. Ipatov, V. Zhukova, A. Zhukov, and J. Gonzalez, "Smart Composites with Short Ferromagnetic Microwires for Microwave Applications," *IEEE Transactions on Magnetics*, vol. 47, no. 10, pp. 4481-4484, Oct. 2011.
- [3] F. X. Qin, H. X. Peng, N. Pankratov, M. H. Phan, L. V. Panina, M. Ipatov, V. Zhukova, A. Zhukov, and J. Gonzalez, "Exceptional Electromagnetic Interference Shielding Properties of Ferromagnetic Microwires Enabled Polymer Composites", *J. Appl. Phys.* vol. 108, pp. 044510, 2010.
- [4] L. Liu, Z. H. Yang, L. B. Kong, and P. Li, "Nanocrystalline Ferromagnetic Microwires Silicone Flexible Composite with Optical Transparency," *IEEE Transactions on Electromagnetic Compatibility*, (In Press).
- [5] J. Carbonell, H. G.-Miquel, and J. S.-Dehsa, "Double Negative Metamaterials Based on Ferromagnetic Microwires", *Physical Review B*, vol. 81, pp. 024401, 2010.
- [6] Y. Huang, G. Wen, T. Li, and K. Xie, "Positive-Negative-Positive Metamaterial Consisting of Ferrimagnetic Host and Wire Array," *Applied Computational Electromagnetics Society (ACES) Journal*, vol. 25, no. 8, pp. 696-702, Aug. 2010.
- [7] H. G.-Miquel, J. Carbonell, and J. S.-Dehesa, "Left Handed Material Based on Amorphous Ferromagnetic Microwires Tunable by Dc Current", *Applied Physics Letters*, vol. 97, pp. 094102, 2010.
- [8] A. Labrador, C. G.-Polo, J. I. P.-Landazábal, V. Zablotkii, I. Ederra, R. Gonzalo, G. B.-Confalonieri, and M. Vázquez, "Magnetotunable Left-Handed Fesib Ferromagnetic Microwires," *Opt. Lett.* vol. 35, pp. 2161-2163, 2010.
- [9] M. Ipatov, V. Zhukova, L. V. Panina, and A. Zhukov, "Ferromagnetic Microwires Composite Metamaterials with Tuneable Microwave Electromagnetic Parameters", *Progress in Electromagnetics Research Symposium PIERS*, vol. 5, no. 6, pp. 586-590, 2009.
- [10] D. Makhnovskiy, A. Zhukov, V. Zhukova, and J. Gonzalez, "Tunable and Self-Sensing Microwave Composite Materials Incorporating Ferromagnetic Microwires", *Advances in Science and Technology*, vol. 54, pp. 201-210, 2008.

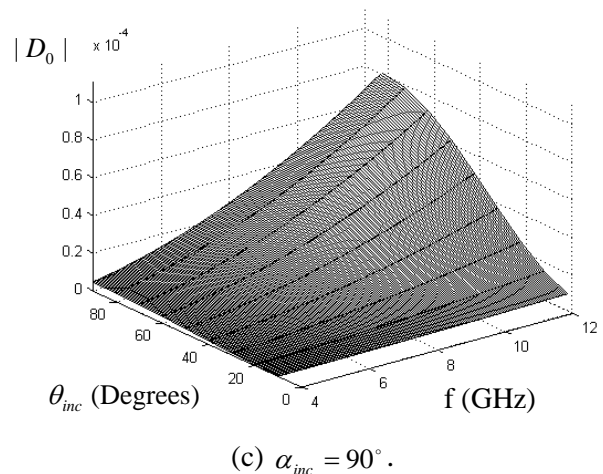
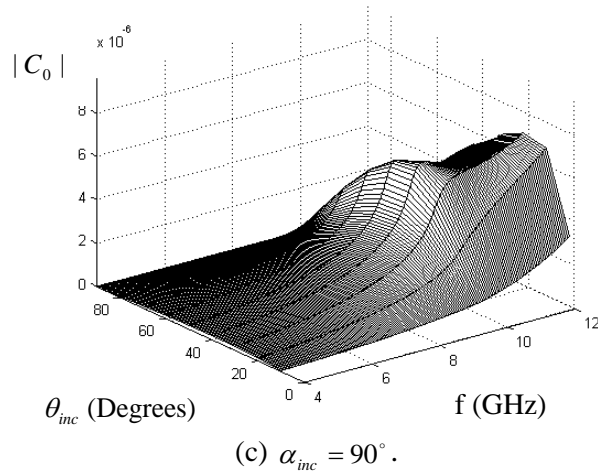
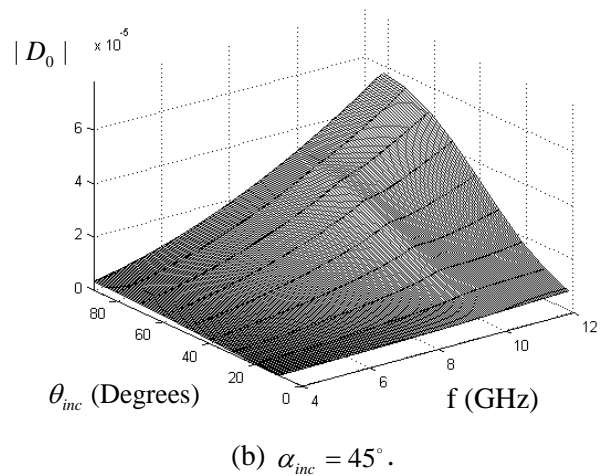
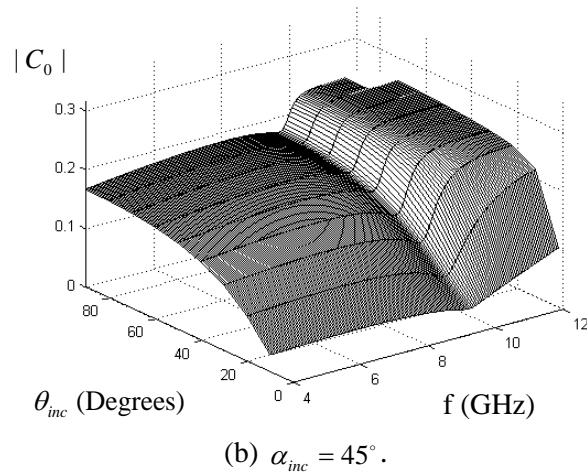
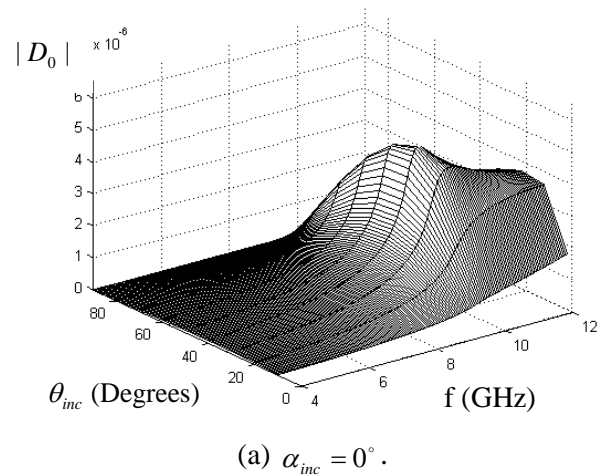
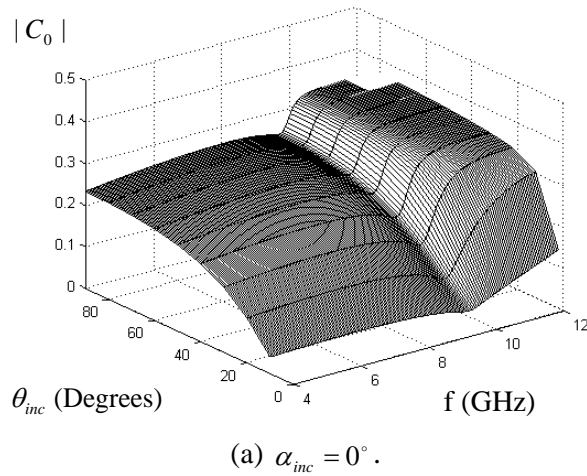


Fig. 2. C_0 scattering coefficient for a ferromagnetic microwire of a radius $r_0 = 45\mu m$ as functions of frequency and angle of incidence (θ_{inc}) at different polarization angles (α_{inc}).

Fig. 3. D_0 scattering coefficient for a ferromagnetic microwire of a radius $r_0 = 45\mu m$ as functions of frequency and angle of incidence (θ_{inc}) at different polarization angles (α_{inc}).

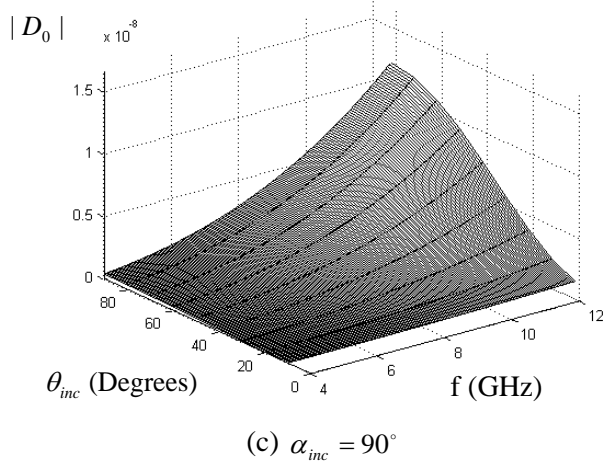
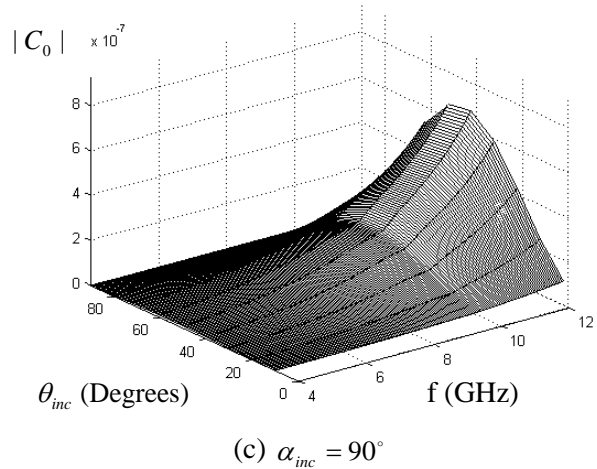
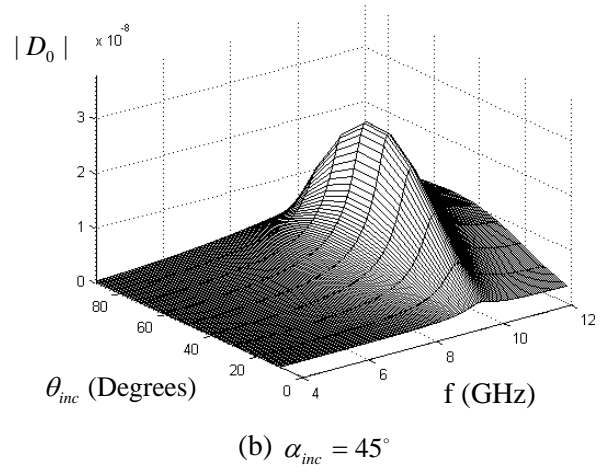
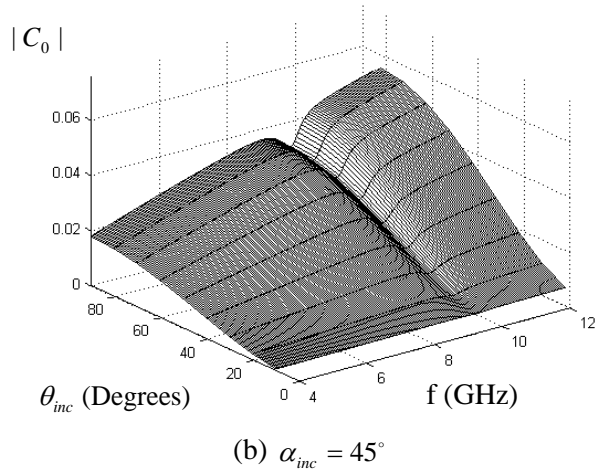
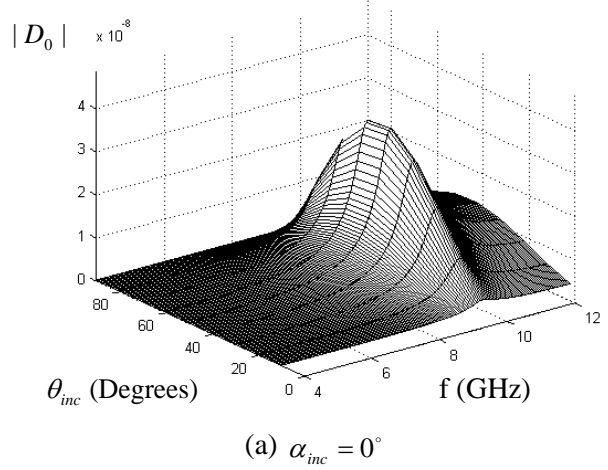
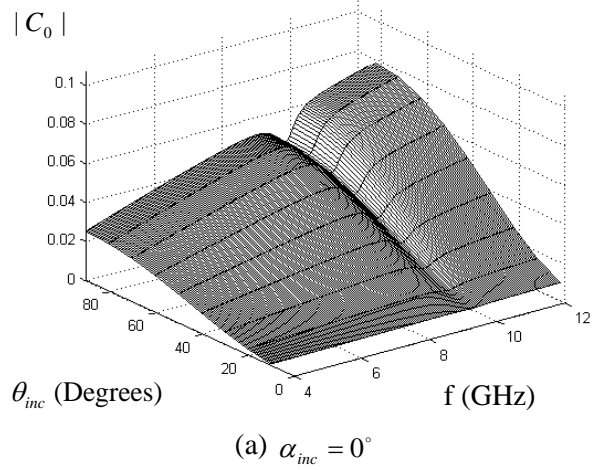


Fig. 4. C_0 scattering coefficient for a ferromagnetic microwire of a radius $r_0 = 4\mu m$ as functions of frequency and angle of incidence (θ_{inc}) at different polarization angles (α_{inc}).

Fig. 5. D_0 scattering coefficient for a ferromagnetic microwire of a radius $r_0 = 4\mu m$ as functions of frequency and angle of incidence (θ_{inc}) at different polarization angles (α_{inc}).

- [11] L. V. Panina, M. Ipatov, V. Zhukova, A. Zhukov, and J. Gonzalez, "Microwave Metamaterials with Ferromagnetic Microwires", *Applied Physics A*, vol. 103, pp. 653-657, 2011.
- [12] A. F. Yagli, J. K. Lee, and E. Arvas, "Monochromatic Scattering from Three-Dimensional Gyrotropic Bodies using the TLM Method", *Applied Computational Electromagnetics Society (ACES) Journal*, vol. 22, no. 1, pp. 155-163, March 2007.
- [13] F. Hunsberger, R. Luebbers, and K. Kunz, "Finite-Difference Time-Domain Analysis of Gyrotropic Media - I: Magnetized Plasma," *IEEE Trans. on Antennas and Propagation*, vol. 40, no. 12, pp. 1489-1495, 1992.
- [14] I. Liberal, I. Ederra, C. G.-Polo, A. Labrador, J. L. P.-Landazábal, R. Gonzalo, "Theoretical Modeling and Experimental Verification of the Scattering from a Ferromagnetic Microwire," *IEEE Trans. on Microwave Theory and Techniques*, vol. MTT-59, no. 3, pp. 517-526, March 2011.
- [15] I. Liberal, I. S. Nefedov, I. Ederra, R. Gonzalo, and S. A. Tretyakov, "Electromagnetic Response and Homogenization of Grids of Ferromagnetic Microwires", *J. Appl. Phys.* vol. 110, pp. 064909, 2011
- [16] R. A. Waldron, "Electromagnetic Wave Propagation in Cylindrical Waveguides Containing Gyromagnetic Media," *Journal of the British Institution of Radio Engineers*, vol.18, no.10, pp. 597-612, Oct. 1958.
- [17] R. A. Waldron, "Theory of the Mode Spectra of Cylindrical Waveguides Containing Gyromagnetic Media," *Journal of the British Institution of Radio Engineers*, vol. 19, no. 6, pp. 347-356, 1959.
- [18] J. Helszajn and A. A. P. Gibson, "Mode Nomenclature of Circular Gyromagnetic and Anisotropic Waveguides with Magnetic and Open Walls", *IEE Proc.*, vol. 134, pt. H, no. 6, pp. 488-496, 1987.
- [19] Y. Rong, W.-B. Dou, and S. -F. Li, "Generalized Field Theory of Irregular Waveguide Partially Filled with Longitudinally Magnetized Ferrite", *IEE Proc.*, vol. 138, pt. H, no. 5, pp. 412-416, 1991.
- [20] D. Pozar, *Microwave Engineering*. 3rd Ed. John Wiley & Sons, Inc., Ch. 9, 2005.

Ahmed M. Attiya graduated from Zagazig University of Egypt in 1991 and received his M.Sc. and Ph.D. in Electronics and Electrical Communications from Cairo University in 1996 and 2001, respectively. Attiya is a full Professor in Microwave Engineering Dept. Electronics Research Institute (Egypt). He is currently a visiting teaching member in Electrical Engineering Dept., King Saud University. In 2002-2004, he was a research fellow in Virginia Polytechnic Inst. and State University. In 2004-2005, he was a visiting scholar in University of Mississippi. His research interest includes antennas, electromagnetic wave propagation, scattering and diffraction problems, and numerical techniques in electromagnetics.

Majeed A. Alkanhal graduated from King Saud University (Saudi Arabia) in 1984 and received his M.Sc. from the same university in 1986. He received Ph.D. in Electronics and Electrical Communications from Electrical Engineering, Syracuse University, Syracuse, New York in 1994. Alkanhal is currently a Full Professor in the Electrical Engineering Dept. Faculty of Engineering, King Saud University. In 2001, he was a Visiting Assistant Professor at the University of Manitoba, Canada. His research interest includes RF and microwave communications and radar systems, radar cross section of complex bodies and materials, electromagnetic scattering from chiral, bi-istropic and bi-anisotropic material objects, antenna design and optimization for communication and radar systems, application of modern estimation and optimization techniques to signal processing and digital communications problems, radar and SAR (Synthetic Aperture Radar) systems and measurements, and numerical solutions to electromagnetics and Electronic/Optical device problems.

An Equivalent Dipole-Moment Method Based Multilevel Fast Multipole Algorithm for Dielectric Objects

Xinlei Chen, Changqing Gu, Ji Ding, Xiaoqiao Deng, Zhenyi Niu, and Zhuo Li

College of Electronic and Information Engineering
Nanjing University of Aeronautics and Astronautics, Nanjing 210016, China
chenxl@nuaa.edu.cn, gucq@nuaa.edu.cn, dingji@nuaa.edu.cn

Abstract — An equivalent dipole-moment method (EDM) based multilevel fast multipole algorithm (MLFMA), namely EDM-MLFMA, is proposed for the electromagnetic scattering from three-dimensional (3D) dielectric objects. In this scheme, the MLFMA is employed to accelerate the interactions of equivalent dipoles in the far regions by expanding the 3D dyadic Green's function into a multipole expression. The memory requirement and CPU time of the conventional EDM are reduced from $O(N^2)$ to $O(N \log N)$, where N is the number of unknowns. Numerical results are presented to validate the efficiency and accuracy of this method.

Index Terms — Equivalent dipole-moment method (EDM), multilevel fast multipole algorithm (MLFMA), volume integral equation (VIE).

I. INTRODUCTION

The scattering of electromagnetic (EM) waves from dielectric materials is an important research area because of the wide applications in dielectric radomes, anisotropic substrates, absorbing materials, etc. [1-2]. In the method of moments (MoM), the volume integral equation (VIE) is generally appropriate for dielectric objects with inhomogeneity and anisotropy. However, the conventional MoM converts the VIE to a dense matrix equation, which is very expensive and formidable especially for large scale EM targets. The $O(N^2)$ memory and computational complexity for iterative solvers is required for both computing the MoM impedance matrix elements and solving this dense matrix equation, where N is the number of unknowns.

More recently, the equivalent dipole-moment method (EDM) [3-4] has been developed to efficiently generate the impedance matrix elements for surface integral equation (SIE). Later, the EDM was extended to deal with the isotropic media [5] and anisotropic media [6-7]. The EDM is based on the commonly used Rao-Wilton-Glisson (RWG) [8] and Schaubert-Wilton-Glisson (SWG) [9] basis functions. In the EDM, each RWG triangle pair or SWG tetrahedron pair is viewed as a dipole model with an equivalent dipole moment. The main advantage of the EDM is that the impedance matrix element can be expressed in an extremely simplified form. However, the memory requirement and the matrix-solve time do not change, and the complexities are still $O(N^2)$.

In this article, the EDM is speeded up by the multilevel fast multipole algorithm (MLFMA) [10-16] for solving the EM scattering from three-dimensional (3D) dielectric materials in free-space. All the SWG basis functions are modeled as equivalent dipole models and divided into multilevel cubical groups. Through expanding the 3D dyadic Green's function [12] in the formulation of the EDM using the addition theorem [17-18], the interactions between the source and field equivalent dipoles in nonnearby groups are transformed into aggregation, translation and disaggregation operators. Benefiting from the octree-structured grouping, the interpolation and antinterpolation, only $O(N)$ impedance elements at the finest level should be calculated and stored, and the computation complexity as well as the memory requirement of the conventional EDM are reduced from $O(N^2)$ to $O(N \log N)$.

The remainder of the paper is organized as follows. In Section II, the EDM is briefly presented for the VIE. Then we describe how the MLFMA is used to accelerate the EDM in detail. In Section III, some numerical results about the bistatic radar cross section (RCS) are given to verify the efficiency and accuracy of the method. Finally, conclusions are drawn in Section IV.

II. FORMULATIONS

A. Basic principles of the EDM

Considering an arbitrarily shaped 3D scattering target, which consists of electric anisotropic material characterized by permittivity tensor $\bar{\bar{\epsilon}}(\mathbf{r})$.

The VIE can be constructed by

$$\mathbf{E}^i(\mathbf{r}) = \bar{\bar{\epsilon}}^{-1}(\mathbf{r}) \cdot \mathbf{D}(\mathbf{r}) + j\omega\mathbf{A}(\mathbf{r}) + \nabla\phi(\mathbf{r}), \quad (1)$$

where

$$\mathbf{A}(\mathbf{r}) = \mu_0 \int_V \mathbf{J}(\mathbf{r}') G(\mathbf{r}, \mathbf{r}') dv', \quad (2)$$

$$\phi(\mathbf{r}) = -\frac{1}{j\omega\epsilon_0} \int_V \nabla' \cdot \mathbf{J}(\mathbf{r}') G(\mathbf{r}, \mathbf{r}') dv'. \quad (3)$$

$\mathbf{E}^i(\mathbf{r})$ denotes the incident electric field. $\mathbf{D}(\mathbf{r})$ denotes the total electric flux density. $\mathbf{J}(\mathbf{r})$ is the equivalent volume current. ϵ_0 and μ_0 are the free-space permittivity and permeability, respectively. $G(\mathbf{r}, \mathbf{r}') = e^{-jk|\mathbf{r}-\mathbf{r}'|} / (4\pi|\mathbf{r}-\mathbf{r}'|)$ stands for the free-space scalar Green's function.

The unknown equivalent volume current $\mathbf{J}(\mathbf{r})$ can be expanded by a set of SWG basis functions as

$$\mathbf{J}(\mathbf{r}) = j\omega\bar{\bar{\mathbf{K}}}(\mathbf{r}) \cdot \mathbf{D}(\mathbf{r}) = \sum_{n=1}^N I_n \bar{\bar{\mathbf{K}}}_n \cdot \mathbf{f}_n(\mathbf{r}), \quad (4)$$

where $\mathbf{f}_n(\mathbf{r})$ represents the n th SWG basis function which is defined on two adjoining tetrahedron elements T_n^\pm sharing the n th face S_n in the volume mesh. I_n is the unknown expansion coefficient. N is the number of the faces in the volume mesh. $\bar{\bar{\mathbf{K}}}(\mathbf{r}) = \bar{\mathbf{I}} - \bar{\bar{\epsilon}}_r^{-1}(\mathbf{r})$ is the contrast ratio [19]. $\bar{\mathbf{I}}$ is the unit tensor.

Substituting Eq. (2) - Eq. (4) into Eq. (1) and using the Galerkin's method, finally the matrix equation of the VIE can be obtained by

$$\sum_{n=1}^N Z_{mn} I_n = V_m, m = 1 \sim N, \quad (5)$$

where

$$Z_{mn} = j\omega \langle \mathbf{f}_m(\mathbf{r}), \mathbf{A}_n(\mathbf{r}) \rangle + \langle \mathbf{f}_m(\mathbf{r}), \nabla\phi_n(\mathbf{r}) \rangle + \frac{1}{j\omega\epsilon_0} \langle \mathbf{f}_m(\mathbf{r}), \bar{\bar{\epsilon}}_r^{-1} \cdot \mathbf{f}_n(\mathbf{r}) \rangle, \quad (6)$$

are the impedance matrix elements.

$$V_m = \langle \mathbf{f}_m(\mathbf{r}), \mathbf{E}^i(\mathbf{r}) \rangle, \quad (7)$$

are the right-hand side vector elements.

In the conventional MoM, the multipoint Gaussian quadrature is usually used to calculate Eq. (6). However, this process can be simplified in the EDM. The basic idea of the EDM is that the fields radiated by the current in a SWG element are approximated as the fields due to an infinitely small dipole with an equivalent moment [5]. Based on this assumption, the interaction of two basis functions can be replaced by the interaction of two infinitely small dipoles, except they are very close to each other.

The equivalent dipole moment in the n th SWG element can be obtained by the integration of the volume current over the tetrahedron pair T_n^\pm [6].

$$\mathbf{m}_m = \int_{T_n^\pm} \bar{\bar{\mathbf{K}}}_n \cdot \mathbf{f}_n(\mathbf{r}') dv' \approx a_n \bar{\bar{\mathbf{K}}}_n^+ \cdot (\mathbf{r}_{ns}^c - \mathbf{r}_n^{c+}) + a_n \bar{\bar{\mathbf{K}}}_n^- \cdot (\mathbf{r}_n^{c-} - \mathbf{r}_{ns}^c), \quad (8)$$

where $\mathbf{r}_n^{c\pm}$ and \mathbf{r}_{ns}^c are the position vectors of the centroid of T_n^\pm and the centroid of the common face S_n , respectively.

The impedance elements Z_{mn} can be expressed in a very simple form [5-6]

$$Z_{mn} = \frac{\eta e^{-jkR}}{4\pi} \left[\mathbf{m}'_m \cdot \mathbf{m}_n \left(\frac{jk}{R} + C \right) - (\mathbf{m}'_m \cdot \hat{\mathbf{R}}) (\hat{\mathbf{R}} \cdot \mathbf{m}_n) \left(\frac{jk}{R} + 3C \right) \right], \quad (9)$$

where $\mathbf{R} = \mathbf{r}_{mn} = \mathbf{r}_m - \mathbf{r}_n$ is the vector from the center point \mathbf{r}_n of the n th equivalent dipole to the center point \mathbf{r}_m of the m th equivalent dipole. $R = |\mathbf{R}|$, $\hat{\mathbf{R}} = \mathbf{R}/R$. η is the intrinsic impedance of medium in free-space, and $C = [1 + 1/(jkR)]/R^2$.

$$\mathbf{m}'_m = a_m (\mathbf{r}_m^{c-} - \mathbf{r}_m^{c+}), \quad (10)$$

is the moment of the SWG basis function [9].

It should be mentioned that the matrix elements are computed by the EDM directly when the distance of two SWG elements is greater than the critical distance $0.2\lambda_0$ in this paper.

B. Acceleration of the EDM using the MLFMA

Although the mutual impedance elements can be calculated by the EDM efficiently, the computational complexity for performing a matrix vector product (MVP) is still $O(N^2)$ for iterative methods and all the impedance elements must be stored. So the EDM is limited to solve electrically small targets. In this work, the MLFMA is employed to accelerate the MVP and reduce the memory requirement.

To employ the MLFMA, the entire target needs multilevel grouping first, then nonempty cubes are recorded using octree-structured data at all levels. We consider two dipoles m and n , which belong to two far groups j and i , respectively. Equation (9) of the impedance element Z_{mn} can be rewritten as

$$Z_{mn} = jk\eta\mathbf{m}'_m \cdot \bar{\mathbf{G}}(\mathbf{r}_m, \mathbf{r}_n) \cdot \mathbf{m}_n, \quad (11)$$

where

$$\bar{\mathbf{G}}(\mathbf{r}_m, \mathbf{r}_n) = [\bar{\mathbf{I}}(1+C) - \hat{\mathbf{R}}\hat{\mathbf{R}}(1+3C)]G(\mathbf{r}_m, \mathbf{r}_n), \quad (12)$$

is the dyadic Green's function in free-space, in which

$$C = \frac{1}{jkR} + \frac{1}{(jkR)^2}. \quad (13)$$

In addition, the vector $\mathbf{R} = \mathbf{r}_{mn}$ can be rewritten as $\mathbf{R} = \mathbf{r}_{ji} + \mathbf{r}_{mj} - \mathbf{r}_{ni}$, in which $\mathbf{r}_{ji} = \mathbf{r}_{o_j} - \mathbf{r}_{o_i}$, $\mathbf{r}_{mj} = \mathbf{r}_m - \mathbf{r}_{o_j}$, $\mathbf{r}_{ni} = \mathbf{r}_n - \mathbf{r}_{o_i}$. \mathbf{r}_{o_i} and \mathbf{r}_{o_j} are the center positions of group i and j , respectively. Since the two groups are the far group pair, the addition theorem can be used to expand the dyadic Green's function as [12]

$$\bar{\mathbf{G}}(\mathbf{r}_m, \mathbf{r}_n) \approx \int [\bar{\mathbf{I}} - \hat{\mathbf{k}}\hat{\mathbf{k}}] e^{-jk(\mathbf{r}_{mj} - \mathbf{r}_{ni})} T_L(\mathbf{k}, \mathbf{r}_{ji}) d^2\hat{\mathbf{k}}, \quad (14)$$

where

$$T_L(\mathbf{k}, \mathbf{r}_{ji}) = \frac{k}{16\pi^2} \sum_{l=0}^{L_i} (-j)^{l+1} (2l+1) h_l^{(2)}(kr_{ji}) P_l(\hat{\mathbf{k}} \cdot \mathbf{r}_{ji}) \quad (15)$$

$h_l^{(2)}(\cdot)$ is the spherical Hankel function of the second kind, and $P_l(\cdot)$ is the Legendre function of order l .

Substituting Eq. (14) into Eq. (11), and using the identity of $(\bar{\mathbf{I}} - \hat{\mathbf{k}}\hat{\mathbf{k}}) = (\bar{\mathbf{I}} - \hat{\mathbf{k}}\hat{\mathbf{k}}) \cdot (\bar{\mathbf{I}} - \hat{\mathbf{k}}\hat{\mathbf{k}})$, the impedance element Z_{mn} can be represented by

$$Z_{mn} = jk\eta \int \mathbf{R}_m(\hat{\mathbf{k}}) \cdot T_L(\mathbf{k}, \mathbf{r}_{ji}) \mathbf{F}_n(\hat{\mathbf{k}}) d\hat{\mathbf{k}}, \quad (16)$$

in which the vectors $\mathbf{F}_n(\hat{\mathbf{k}})$ and $\mathbf{R}_m(\hat{\mathbf{k}})$ are radiation function and receive function, respectively and are given by

$$\mathbf{F}_n(\hat{\mathbf{k}}) = \mathbf{m}_n \cdot (\bar{\mathbf{I}} - \hat{\mathbf{k}}\hat{\mathbf{k}}) e^{jk\mathbf{r}_{ni}}, \quad (17)$$

$$\mathbf{R}_m(\hat{\mathbf{k}}) = \mathbf{m}'_m \cdot (\bar{\mathbf{I}} - \hat{\mathbf{k}}\hat{\mathbf{k}}) e^{-jk\mathbf{r}_{mj}}. \quad (18)$$

Physical interpretation of this expansion is that a spherical wave from a dipole in free space is expanded by the sum of an infinite number of plane waves. Using Eq. (16), then the MVP can be computed fast through an aggregation-translation-disaggregation form. The complexities of computation and memory requirement can achieve $O(N \log N)$ profiting from the interpolation, antepolation, and the grid-tree data structure [10-11]. At the finest level, only $O(N)$ impedance elements should be calculated and stored. Further more, part of them can be efficiently calculated by the EDM.

III. NUMERICAL RESULTS

In this section, we present some numerical results to validate the efficiency and accuracy of the new method. In the following examples, all the simulations are performed on a personal computer with the Pentium(R) Dual CPU E5500 with 2.80 GHz (only one core is used) and 2.0 GB RAM. The GMRES iterative solver is employed to obtain an identical residual error ≤ 0.001 and the block diagonal preconditioner is used.

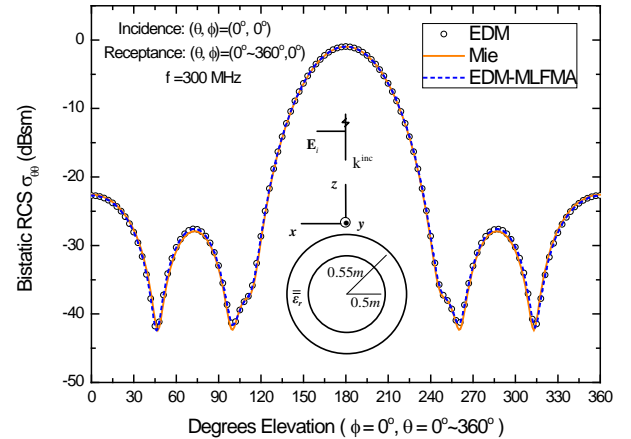


Fig. 1. Bistatic RCSs in $\theta\theta$ polarization of a spherical dielectric shell illuminated by a uniform plane wave with the incident direction of $(\theta, \phi) = (0^\circ, 0^\circ)$.

First, we consider the scattering problem of a spherical dielectric shell. The shell's inner and outer radii are 0.5 m and 0.55 m and the relative permittivity of the shell is $\bar{\epsilon}_r = 1.5 \bar{\mathbf{I}}$, as shown in the inset of Fig. 1. The shell is discretized into 5309 tetrahedrons, and the total number of unknowns is 12213. The size of the finest group is set to 0.15 m and a 3-level EDM-MLFMA is used. The bistatic RCS for $\theta\theta$ polarization calculated by the EDM-MLFMA agrees well with the conventional EDM and the Mie series solution shown in Fig. 1. At 180° , the RCS value of the Mie series is -0.97987 dBsm, and the results obtained by the EDM-MLFMA and the conventional EDM are -0.97359 and -0.97464 dBsm, respectively. The root mean square (rms) errors of the EDM-MLFMA and the conventional EDM are 0.448 and 0.441 dBsm, respectively.

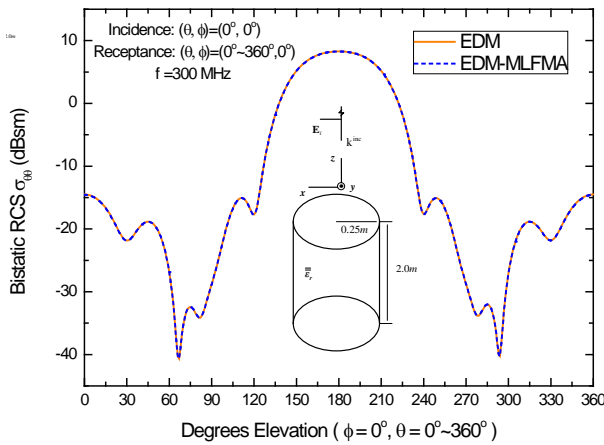


Fig. 2. Bistatic RCSs in $\theta\theta$ polarization of a dielectric cylinder illuminated by a uniform plane wave with the incident direction of $(\theta, \phi) = (0^\circ, 0^\circ)$.

Then the bistatic RCS of a dielectric cylinder is considered. The radii and height of the cylinder are 0.25 m and 2.0 m. The relative permittivity of the cylinder is $\bar{\epsilon}_r = 1.5 \bar{\mathbf{I}}$. The target is discretized into 5668 tetrahedrons, and the total number of unknowns is 11897. A 4-level EDM-MLFMA is used and the size of the group at the finest level is 0.15 m. The bistatic RCS in $\theta\theta$ polarization obtained by the EDM-MLFMA agrees well with the conventional EDM shown in Fig. 2.

Finally the bistatic RCS of an anisotropic dielectric target is considered. The target is constituted by 5 small slabs with the same size $1.0 \text{ m} \times 4.0 \text{ m} \times 0.05 \text{ m}$, but the 5 small slabs have

different relative permittivities (see Fig. 3, $\bar{\epsilon}_{r,1} = [1.5, j, 0; -j, 1.5, 0; 0, 0, 2.0]$, $\bar{\epsilon}_{r,2} = (1.75 - 0.5j) \bar{\mathbf{I}}$ and $\bar{\epsilon}_{r,3} = [2.0, j, 0; -j, 2.0, 0; 0, 0, 1.5]$). The target is discretized into 49470 tetrahedrons, and the total number of unknowns is 115620. A 6-level EDM-MLFMA is used and the group at the finest level is also with the size of 0.15 m. The bistatic RCS in $\theta\theta$ polarization obtained by the EDM-MLFMA is shown in Fig. 3. This target could not be calculated by the conventional EDM, because the memory is not enough. The conventional EDM is estimated to require about 100 GB memory and 4 h CPU time.

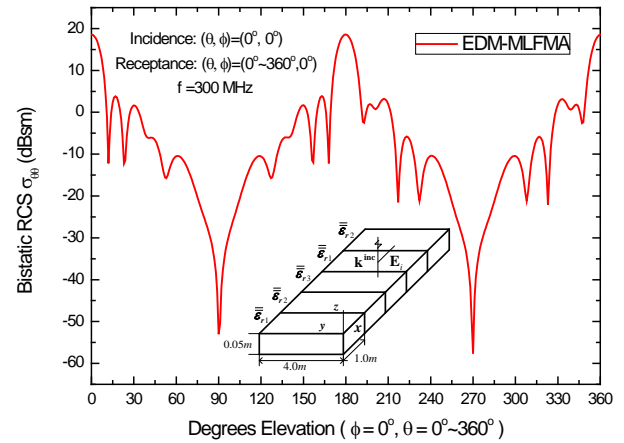


Fig. 3. Bistatic RCSs in $\theta\theta$ polarization of an anisotropic dielectric target illuminated by a uniform plane wave with the incident direction of $(\theta, \phi) = (0^\circ, 0^\circ)$.

Table 1 summarizes the CPU time and memory requirement of the above simulations. It can be seen that the EDM-MLFMA saves much CPU time and memory than the conventional EDM.

Table 1: Comparison of CPU time and memory requirement of the conventional EDM and EDM-MLFMA

Method	EDM		EDM-MLFMA	
	Time	Memory	Time	Memory
Problem 1	132 s	1188 MB	51 s	145 MB
Problem 2	138 s	1128 MB	58 s	171 MB
Problem 3	-	-	520 s	1390 MB

IV. CONCLUSION

In this article, the EDM based MLFMA is introduced and applied to solve the VIE in the electromagnetic scattering of dielectric targets.

The new method can reduce both the CPU time and memory requirement of the conventional EDM to $O(N\log N)$. In the future, this method will be extended and applied to solve surface integral equation (SIE) and volume-surface integral equation (VSIE).

ACKNOWLEDGMENT

The work was supported by the National Nature Science Foundation of China under Grant No. 61071019 and the Funding of Jiangsu Innovation Program for Graduate Education under Grant No. CXZZ11_0229.

REFERENCES

- [1] D. Ding, J. Ge, and R. Chen, "Well-Conditioned CFIE for Scattering from Dielectric Coated Conducting Bodies Above a Half-Space," *Applied Computational Electromagnetics Society (ACES) Journal*, vol. 25, no. 11, pp. 936-946, Nov. 2010.
- [2] J.-Y. Li, J.-L. Guo, Y.-L. Zou, Q.-Z. Liu, "Analysis of a Cylindrical Dielectric Radome Covering Omnidirectional Waveguide Slot Antennas," *Applied Computational Electromagnetics Society (ACES) Journal*, vol. 23, no. 2, pp. 166-173, Jun. 2008.
- [3] S. N. Makarov, *Antenna and EM Modeling with MATLAB*, Wiley, New York, 2002.
- [4] J. Yeo, S. K. Öksoy, V. V. S. Prakash, and R. Mittra, "Efficient Generation of Method of Moments Matrices Using the Characteristic Function Method," *IEEE Trans. Antennas Propag.*, vol. 52, no. 12, pp. 3405-3410, Dec. 2004.
- [5] J. D. Yuan, C. Q. Gu, and G. D. Han, "Efficient Generation of Method of Moments Matrices Using Equivalent Dipole-Moment Method," *IEEE Antennas and Wireless Propag. Lett.*, vol. 8, pp. 716-719, 2009.
- [6] J. D. Yuan, C. Q. Gu, and Z. Li, "Electromagnetic Scattering by Arbitrarily Shaped Stratified Anisotropic Media Using the Equivalent Dipole Moment Method," *International Journal of RF and Microwave Computer-Aided Engineering*, vol. 20, no. 4, pp. 416-421, 2010.
- [7] X. Deng, C. Gu, and Y. Zhou, "Electromagnetic Scattering by Arbitrarily Shaped Three-Dimensional Conducting Objects Covered with Electromagnetic Anisotropic Materials," *Applied Computational Electromagnetics Society (ACES) Journal*, vol. 26, no. 11, pp. 886-892, November 2011.
- [8] S. M. Rao, D. R. Wilton, and A. W. Glisson, "Electromagnetic Scattering by Surfaces of Arbitrary Shape," *IEEE Trans. Antennas Propag.*, vol. AP-30, no. 3, pp. 409-418, May 1982.
- [9] D. H. Schaubert, D. R. Wilton, and A. W. Glisson, "A Tetrahedral Modeling Method for Electromagnetic Scattering by Arbitrarily Shaped Inhomogeneous Dielectric Bodies," *IEEE Trans. Antennas Propag.*, vol. AP-32, no. 1, pp. 77-85, Jan. 1984.
- [10] J. M. Song and W. C. Chew, "Multilevel Fast-Multipole Algorithm for Solving Combined Field Integral Equations of Electromagnetic Scattering," *Microwave Opt. Technol. Lett.*, vol. 10, no. 1, pp. 14-19, Sept. 1995.
- [11] J. M. Song, C. C. Lu, and W. C. Chew, "Multilevel Fast Multipole Algorithm for Electromagnetic Scattering by Large Complex Objects," *IEEE Trans. Antennas Propag.*, vol. 45, no. 10, pp. 1488-1493, Oct. 1997.
- [12] W. C. Chew, J. M. Jin, E. Michielssen, and J. M. Song, *Fast and Efficient Algorithms in Computational Electromagnetics*, MA: Artech House, Boston, 2001.
- [13] M. Li, H. Chen, C. Li, R. Chen, and C. Ong, "Hybrid UV/MLFMA Analysis of Scattering by PEC Targets Above a Lossy Half-Space," *Applied Computational Electromagnetics Society (ACES) Journal*, vol. 26, no. 1, pp. 17-25, Jan. 2011.
- [14] M. Chen, R. S. Chen, and X. Q. Hu, "Augmented MLFMM for Analysis of Scattering from PEC Object with Fine Structures," *Applied Computational Electromagnetics Society (ACES) Journal*, vol. 26, no. 5, pp. 418-428, May 2011.
- [15] M. Chen, R. Chen, Z. Fan, and D. Ding, "Accelerating the Multilevel Fast Multipole Method with Parallel Preconditioner for Large-Scale Scattering Problems," *Applied Computational Electromagnetics Society (ACES) Journal*, vol. 26, no. 10, pp. 815-822, Oct. 2011.
- [16] H. Fangjing, N. Zaiping, and H. Jun, "An Efficient Parallel Multilevel Fast Multipole Algorithm for Large-Scale Scattering Problems," *Applied Computational Electromagnetics Society (ACES) Journal*, vol. 25, no. 4, pp. 38-387, Apr. 2010.
- [17] R. Coifman, V. Rokhlin, and S. Wandzura, "The Fast Multipole Method for the Wave Equation: A Pedestrian Prescription," *IEEE Ant. Propag. Mag.*, vol. 35, pp. 7-12, Jun. 1993.
- [18] M. Abramowitz and I. A. Stegun, *Handbook of Mathematical Functions*, New York: Dover Publication, 1972.
- [19] G. Kobidze and B. Shanker, "Integral Equation Based Analysis of Scattering from 3-D Inhomogeneous Anisotropic Bodies," *IEEE Trans. Antennas Propag.*, vol. 52, no. 10, pp. 2650-2658, Oct. 2004.

Improved Weakly Conditionally Stable Finite-Difference Time-Domain Method

Juan Chen

School of Electronic and Information Engineering, Xi'an Jiaotong University, Xi'an 710049, China
chenjuan0306@yahoo.com.cn

Abstract — To circumvent the inaccuracy in the implementation of the perfect-electric-conductor (PEC) condition in the weakly conditionally stable finite-difference time-domain (WCS-FDTD) method, an improved weakly conditionally stable (IWCS) FDTD method is presented in this paper. In this method, the solving of the tridiagonal matrix for the magnetic field component is replaced by the solving of the tridiagonal matrix for the electric field components; thus, the perfect-electric-conductor (PEC) condition for the electric field components is implemented accurately. The formulations of the IWCS-FDTD method are given, and the stability condition of the IWCS-FDTD scheme is presented analytically. Compared with the WCS-FDTD method, this new method has higher accuracy in the implantation of the PEC condition, which is demonstrated through numerical examples.

Index Terms — FDTD method, perfect-electric-conductor (PEC) condition, weakly conditionally stable FDTD method.

I. INTRODUCTION

To overcome the Courant limit on the time step size of the FDTD method [1,2], unconditionally stable methods such as the alternating-direction implicit FDTD (ADI-FDTD) scheme [3-12] and a weakly conditionally stable finite-difference time-domain (WCS-FDTD) method has been developed recently [13,14]. In the WCS-FDTD method, the CFL condition is not removed totally, but being weaker than that of the conventional FDTD method. The time step in this scheme is only determined by one space discretization, which is extremely useful for problems where a very fine mesh is needed in one

or two directions. The WCS-FDTD method has better accuracy and higher computation efficiency than the ADI-FDTD method, especially for larger field variation.

However, in the WCS-FDTD method, updating of H_y component needs the unknown E_x and E_z components at the same time step, thus, the H_y component has to be updated implicitly by solving tridiagonal matrix [10], which results in a large inaccuracy in the implementation of the perfect-electric-conductor (PEC) condition for the E_x and E_z components. To circumvent this problem, an improved weakly conditionally stable finite-difference time-domain (IWCS-FDTD) is presented in this paper. In this method, the solving of the tridiagonal matrix for the H_y component is replaced by the solving the tridiagonal matrix of the E_x and E_z components; thus, the perfect-electric-conductor (PEC) condition for the E_x and E_z components is implemented easily. The formulations of the IWCS-FDTD method are presented, and the final updating equations are given. The stability condition of the IWCS-FDTD scheme is presented analytically. Compared with the WCS-FDTD method, this new method has higher accuracy in the implantation of the PEC condition, which is demonstrated through numerical examples.

II. FORMULATION FOR THE IWCS-FDTD METHOD

In a linear, non-dispersive, and lossless medium, the 3D WCS-FDTD scheme in reference [10] can be written as:

$$E_x^{n+1} = E_x^n + 2aD_y H_z^{n+1/2} - aD_z (H_y^{n+1} + H_y^n) \quad (1)$$

$$E_z^{n+1} = E_z^n - 2aD_y H_x^{n+1/2} + aD_x (H_y^{n+1} + H_y^n) \quad (2)$$

$$H_y^{n+1} = H_y^n + bD_x (E_z^{n+1} + E_z^n) - bD_z (E_x^{n+1} + E_x^n) \quad (3)$$

$$H_x^{n+3/2} = H_x^{n+1/2} - 2bD_y E_z^{n+1} + bD_z (E_y^{n+3/2} + E_y^{n+1/2}) \quad (4)$$

$$H_z^{n+3/2} = H_z^{n+1/2} + 2bD_y E_x^{n+1} - bD_x (E_y^{n+3/2} + E_y^{n+1/2}) \quad (5)$$

$$E_y^{n+3/2} = E_y^{n+1/2} - aD_x (H_z^{n+3/2} + H_z^{n+1/2}) + aD_z (H_x^{n+3/2} + H_x^{n+1/2}) \quad (6)$$

here, $a = \Delta t/2\varepsilon$, $b = \Delta t/2\mu$, $D_w = \partial/\partial w$ ($w = x, y$) represents the first derivative operator with respect to w . ε is the permittivity and μ is the permeability of the medium, n and Δt are the index and size of time-step.

Obviously, updating of H_y component, as shown in eq. (3), needs the unknown E_x and E_z components at the same time step. In the WCS-FDTD scheme, the H_y component is updated by substituting eqs. (1) and (2) into eq. (3) [10] directly. This results in a broadly band matrix equation which is updated by solving two tri-diagonal matrix equation.

Here, we apply a new technique to solve eqs. (1)-(3). For simplicity, we write eqs. (1)-(3) in a new form as,

$$E_x^{n+1} = E_x^* - aD_z H_y^{n+1} \quad (7)$$

$$E_z^{n+1} = E_z^* + aD_x H_y^{n+1} \quad (8)$$

$$H_y^{n+1} = H_y^* + bD_x E_z^{n+1} - bD_z E_x^{n+1} \quad (9)$$

where,

$$E_x^* = E_x^n + 2aD_y H_z^{n+1/2} - aD_z H_y^n \quad (10)$$

$$E_z^* = E_z^n - 2aD_y H_x^{n+1/2} + aD_x H_y^n \quad (11)$$

$$H_y^* = H_y^n + bD_x E_z^n - bD_z E_x^n \quad (12)$$

Obviously, updating of E_x and E_z components, as shown in eqs. (7) and (8), needs the unknown H_y component at the same

time step. By substituting eq. (9) into eqs. (7) and (8) we can obtain,

$$(1 - abD_{2z}) E_x^{n+1} = E_x^* - aD_z H_y^* - abD_z D_x E_z^{n+1} \quad (13)$$

$$(1 - abD_{2x}) E_z^{n+1} = E_z^* + aD_x H_y^* - abD_z D_x E_x^{n+1} \quad (14)$$

Multiplying eq.(13) by factor $(1 - abD_{2x})$, and subtracting $(abD_z D_x) \times$ eq.(14), we have,

$$(1 - abD_{2x} - abD_{2z}) E_x^{n+1} = (1 - abD_{2x}) E_x^* - aD_z H_y^* - abD_z D_x E_z^* \quad (15)$$

The left side of eq. (15) is a broadly-banded matrix equation which is solved expensively. To improve the computation efficiency, new terms are added at the both side of eq.(15),

$$(1 - abD_{2x} - abD_{2z} + a^2 b^2 D_{2x} D_{2z}) E_x^{n+1} = (1 - abD_{2x}) E_x^* - aD_z H_y^* - abD_z D_x E_z^* + a^2 b^2 D_{2x} D_{2z} E_x^n \quad (16)$$

It is equivalent to the following,

$$(1 - abD_{2x})(1 - abD_{2z}) E_x^{n+1} = (1 - abD_{2x}) E_x^* - aD_z H_y^* - abD_z D_x E_z^* + a^2 b^2 D_{2x} D_{2z} E_x^n \quad (17)$$

Dividing eq. (17) into two sub-steps, we have,

$$(1 - abD_{2x}) e_x = a^2 b^2 D_{2x} D_{2z} E_x^n - aD_z H_y^* - abD_z D_x E_z^* \quad (18.a)$$

$$(1 - abD_{2z}) E_x^{n+1} = e_x + E_x^* \quad (18.b)$$

With this manipulation, the updating of the E_x component requires the solution of two tri-diagonal matrices (18.a) and (18.b).

In a similar way, updating of E_z component can be written as,

$$(1 - abD_{2z}) e_z = a^2 b^2 D_{2x} D_{2z} E_z^n + aD_x H_y^* - abD_z D_x E_x^* \quad (19.a)$$

$$(1 - abD_{2x})E_z^{n+1} = e_z + E_z^* \quad (19.b)$$

After the solving of the E_x^{n+1} and E_z^{n+1} components, the H_y component can be updated using equation (3) explicitly, thus, the solving of the tridiagonal matrix for the H_y component in the WCS-FDTD method is replaced by the solving of the tridiagonal matrix for the E_x and E_z components here.

Approximating each derivative in space by centered second-order finite differences, we can obtain the final updating equations for E_x , E_z and H_y components. Such as, the updating equations for E_x component are as follows,

$$\begin{aligned} & \left(1 + \frac{2ab}{\Delta x^2}\right) e_x \left(i + \frac{1}{2}, j, k\right) \\ & - \frac{ab}{\Delta x^2} e_x \left(i + \frac{3}{2}, j, k\right) - \frac{ab}{\Delta x^2} e_x \left(i - \frac{1}{2}, j, k\right) \\ & = \frac{a^2 b^2}{\Delta z^2 \Delta x^2} \left[\begin{array}{l} E_x^n \left(i + \frac{3}{2}, j, k + 1\right) - E_x^n \left(i + \frac{1}{2}, j, k + 1\right) \\ - E_x^n \left(i + \frac{1}{2}, j, k + 1\right) + E_x^n \left(i - \frac{1}{2}, j, k + 1\right) \end{array} \right] \\ & - \frac{2a^2 b^2}{\Delta z^2 \Delta x^2} \left[\begin{array}{l} E_x^n \left(i + \frac{3}{2}, j, k\right) - E_x^n \left(i + \frac{1}{2}, j, k\right) \\ - E_x^n \left(i + \frac{1}{2}, j, k\right) + E_x^n \left(i - \frac{1}{2}, j, k\right) \end{array} \right] \\ & + \frac{a^2 b^2}{\Delta z^2 \Delta x^2} \left[\begin{array}{l} E_x^n \left(i + \frac{3}{2}, j, k - 1\right) - E_x^n \left(i + \frac{1}{2}, j, k - 1\right) \\ - E_x^n \left(i + \frac{1}{2}, j, k - 1\right) + E_x^n \left(i - \frac{1}{2}, j, k - 1\right) \end{array} \right] \\ & - a \frac{H_y^* \left(i + \frac{1}{2}, j, k + \frac{1}{2}\right) - H_y^* \left(i + \frac{1}{2}, j, k - \frac{1}{2}\right)}{\Delta z} \\ & - \frac{ab}{\Delta z \Delta x} \left[\begin{array}{l} E_z^* \left(i + 1, j, k + \frac{1}{2}\right) - E_z^* \left(i, j, k + \frac{1}{2}\right) \\ - E_z^* \left(i + 1, j, k - \frac{1}{2}\right) + E_z^* \left(i, j, k - \frac{1}{2}\right) \end{array} \right] \end{aligned} \quad (20.a)$$

$$\begin{aligned} & \left(1 + \frac{2ab}{\Delta z^2}\right) E_x^{n+1} \left(i + \frac{1}{2}, j, k\right) \\ & - \frac{ab}{\Delta z^2} E_x^{n+1} \left(i + \frac{1}{2}, j, k + 1\right) \\ & - \frac{ab}{\Delta z^2} E_x^{n+1} \left(i + \frac{1}{2}, j, k - 1\right) \\ & = e_x \left(i + \frac{1}{2}, j, k\right) + E_x^* \left(i + \frac{1}{2}, j, k\right) \end{aligned} \quad (20.b)$$

where,

$$\begin{aligned} H_y^* \left(i + \frac{1}{2}, j, k + \frac{1}{2}\right) & = H_y^n \left(i + \frac{1}{2}, j, k + \frac{1}{2}\right) \\ & + b \left[\begin{array}{l} \frac{E_z^n \left(i + 1, j, k + \frac{1}{2}\right) - E_z^n \left(i, j, k + \frac{1}{2}\right)}{\Delta x} \\ - \frac{E_x^n \left(i + \frac{1}{2}, j, k + 1\right) - E_x^n \left(i + \frac{1}{2}, j, k\right)}{\Delta z} \end{array} \right] \end{aligned} \quad (21)$$

$$\begin{aligned} E_z^* \left(i + 1, j, k + \frac{1}{2}\right) & = E_z^n \left(i + 1, j, k + \frac{1}{2}\right) \\ & + a \frac{H_y^n \left(i + \frac{3}{2}, j, k + \frac{1}{2}\right) - H_y^n \left(i + \frac{1}{2}, j, k + \frac{1}{2}\right)}{\Delta x} \\ & - \frac{2a}{\Delta y} \left[\begin{array}{l} H_x^{n+1/2} \left(i + 1, j + \frac{1}{2}, k + \frac{1}{2}\right) \\ - H_x^{n+1/2} \left(i + 1, j - \frac{1}{2}, k + \frac{1}{2}\right) \end{array} \right] \end{aligned} \quad (22)$$

$$\begin{aligned} E_x^* \left(i + \frac{1}{2}, j, k\right) & = E_x^n \left(i + \frac{1}{2}, j, k\right) \\ & - a \frac{H_y^n \left(i + \frac{1}{2}, j, k + \frac{1}{2}\right) - H_y^n \left(i + \frac{1}{2}, j, k - \frac{1}{2}\right)}{\Delta z} \\ & + \frac{2a}{\Delta y} \left[\begin{array}{l} H_z^{n+1/2} \left(i + \frac{1}{2}, j + \frac{1}{2}, k\right) \\ - H_z^{n+1/2} \left(i + \frac{1}{2}, j - \frac{1}{2}, k\right) \end{array} \right] \end{aligned} \quad (23)$$

The solving of the E_y component, same as that in the WCS-FDTD method, is updated implicitly by substituting eqs. (4) and (5) into eq. (6),

$$\begin{aligned} & (1 - abD_{2x} - abD_{2z})E_y^{n+3/2} \\ & = (1 + abD_{2x} + abD_{2z})E_y^{n+1/2} \\ & - 2aD_x H_z^{n+1/2} + 2aD_z H_x^{n+1/2} \\ & - 2abD_x D_y E_x^{n+1} - 2abD_y D_z E_z^{n+1} \end{aligned} \quad (24)$$

The left side of eq. (24) is also a broadly-banded matrix equation. Adding new terms at the both side of eq.(24) and dividing it into two sub-steps, we can obtain the updating of the E_y component as follows,

$$\begin{aligned} & (1 - abD_{2x})e_y \\ & = (1 + abD_{2x})(1 + abD_{2z})E_y^{n+1/2} \\ & - 2aD_x H_z^{n+1/2} + 2aD_z H_x^{n+1/2} \end{aligned} \quad (25.a)$$

$$\begin{aligned} & - 2abD_x D_y E_x^{n+1} - 2abD_y D_z E_z^{n+1} \\ & (1 - abD_{2z})E_y^{n+3/2} = e_y. \end{aligned} \quad (25.b)$$

Thus, at each time step the IWCS-FDTD method requires the solution of six tridiagonal matrices and two explicit equations.

III. WEAKLY CONDITIONAL STABILITY OF THE IWCS-FDTD METHOD

The relations between the field components of the IWCS-FDTD method can be represented in matrix forms,

$$[A][\Lambda]^{n+1} = [B][\Lambda]^* + [C][\Lambda]^n \quad (26)$$

where,

$$[A] = \begin{bmatrix} S & 0 & 0 & 0 & 0 & 0 \\ 2abD_x D_y & S & 2abD_z D_y & 0 & 0 & 0 \\ 0 & 0 & S & 0 & 0 & 0 \\ 0 & -bD_z & 2bD_y & 1 & 0 & 0 \\ bD_z & 0 & -bD_x & 0 & 1 & 0 \\ -2bD_y & bD_x & 0 & 0 & 0 & 1 \end{bmatrix}$$

$$[B] = \begin{bmatrix} 1 - abD_{2x} & 0 & -abD_z D_x & 0 & -aD_z & 0 \\ 0 & 0 & 0 & 0 & 0 & 0 \\ -abD_z D_x & 0 & 1 - abD_{2z} & 0 & aD_x & 0 \\ 0 & 0 & 0 & 0 & 0 & 0 \\ 0 & 0 & 0 & 0 & 0 & 0 \\ 0 & 0 & 0 & 0 & 0 & 0 \end{bmatrix}$$

$$[C] = \begin{bmatrix} a^2 b^2 D_{2x} D_{2z} & 0 & 0 & 0 & 0 & 0 \\ 0 & S_2 & 0 & 2aD_z & 0 & -2aD_x \\ 0 & 0 & a^2 b^2 D_{2x} D_{2z} & 0 & 0 & 0 \\ 0 & bD_z & 0 & 1 & 0 & 0 \\ -bD_z & 0 & bD_x & 0 & 1 & 0 \\ 0 & -bD_x & 0 & 0 & 0 & 1 \end{bmatrix}$$

$$[\Lambda]^{n+1} = [E_x^{n+1} \ E_y^{n+3/2} \ E_z^{n+1} \ H_x^{n+3/2} \ H_y^{n+1} \ H_z^{n+3/2}]'$$

$$[\Lambda]^* = [E_x^* \ E_y^* \ E_z^* \ H_x^* \ H_y^* \ H_z^*]'$$

$$S = 1 - abD_{2x} - abD_{2z} + a^2 b^2 D_{2x} D_{2z}$$

$$S_2 = 1 + abD_{2x} + abD_{2z} + a^2 b^2 D_{2x} D_{2z}$$

According eqs. (10)-(12), we have,

$$[\Lambda]^* = [D][\Lambda]^n \quad (27)$$

with,

$$[D] = \begin{bmatrix} 1 & 0 & 0 & 0 & -aD_z & 2aD_y \\ 0 & 0 & 0 & 0 & 0 & 0 \\ 0 & 0 & 1 & -2aD_y & aD_x & 0 \\ 0 & 0 & 0 & 0 & 0 & 0 \\ -bD_z & 0 & bD_x & 0 & 1 & 0 \\ 0 & 0 & 0 & 0 & 0 & 0 \end{bmatrix}$$

Substituting eq. (27) into eq. (26), we obtain,

$$[\Gamma][\Lambda]^n = 0 \quad (28)$$

here,

$$\begin{aligned} [\Gamma] & = [A]\zeta - [B][D] - [C] \\ & = \begin{bmatrix} (S\zeta - S_1) & 0 & 2abD_z D_x - 2a^2 b f & 2aD_z & f_x \\ 2abD_x D_y \zeta & (S\zeta - S_2) & 2abD_z D_y \zeta - 2aD_z & 0 & 2aD_x \\ 2abD_z D_x & 0 & (S\zeta - S_3) & f_z & -2aD_x 2a^2 b f \\ 0 & -L_z & 2bD_y \zeta & \zeta - 1 & 0 & 0 \\ L_z & 0 & -L_x & 0 & \zeta - 1 & 0 \\ -2bD_y \zeta & L_x & 0 & 0 & 0 & \zeta - 1 \end{bmatrix} \end{aligned}$$

and

$$\begin{aligned} S_1 &= 1 - abD_{2x} + abD_{2z} + a^2b^2D_{2x}D_{2z} \\ S_3 &= 1 + abD_{2x} - abD_{2z} + a^2b^2D_{2x}D_{2z}; \\ f &= D_x D_y D_z; \\ f_z &= 2a D_y (1 - abD_{2z}); \\ f_x &= -2a D_y (1 - abD_{2x}); \\ L_w &= b D_w (\xi + 1), w = x, z. \end{aligned}$$

For a nontrivial solution of eq. (28), the determinant of the coefficient matrix in eq. (28) should be zero,

$$|\Gamma| = 0 \quad (29)$$

By solving eq. (29), we have,

$$(\zeta - 1)^2 (M^2 \zeta^2 - 2N\zeta + M^2) (M\zeta^2 - 2P\zeta + M) = 0 \quad (30)$$

here,

$$\begin{aligned} M &= (1 - abD_{2x})(1 - abD_{2z}) \\ N &= (1 + abD_{2x})(1 + abD_{2z})(1 - abD_{2x})(1 - abD_{2z}) \\ &+ 2abD_{2y}(1 - abD_{2x} - abD_{2z})(1 + a^2b^2D_{2x}D_{2z}) \\ P &= (1 + abD_{2x})(1 + abD_{2z}) + 2abD_{2y} \end{aligned}$$

The growth factor ζ is obtained,

$$\zeta_{1,2} = 1 \quad (31)$$

$$\zeta_{3,4} = \left(N \pm \sqrt{N^2 - M^4} \right) / M^2 \quad (32)$$

$$\zeta_{5,6} = \left(P \pm \sqrt{P^2 - M^2} \right) / M \quad (33)$$

To satisfy the stability condition during the field advancement, the module of growth factor ζ can't be larger than 1. It is evident that the module of $\zeta_{1,2}$ is unity.

For the values of $\zeta_{3,4}$ and $\zeta_{5,6}$, when the conditions $M^4 \geq N^2$ and $M^2 \geq P^2$ are satisfied, $|\zeta_{3,4}| = |\zeta_{5,6}| = 1$ can be obtained. Approximating each derivative in space by centered second-order finite differences, we can obtain the limitation for time-step size in the IWCS-FDTD method as follows,

$$\Delta t \leq \Delta y / c \quad (34)$$

where $c = 1/\sqrt{\epsilon\mu}$ is the speed of light in the medium.

The stable condition of the IWCS-FDTD method is same as that of WCS-FDTD method. The maximum time-step size for IWCS-FDTD method is only determined by one spatial increment Δy . This is due to that the explicit difference is only used in the y direction.

IV. NUMERICAL VALIDATION

To demonstrate the accuracy and efficiency of the proposed theory, a numerical example is presented here. A metal plate with dimension 60mm \times 60mm is shown in Fig.1. Twenty five apertures of 2 mm length and 2 mm width are cut on the plate. All the distances between the apertures are 10 mm. A uniform plane wave polarized along the z -direction, is normally incident on the aperture, and the time dependence of the excitation function is as follows,

$$E_z(t) = \exp[-4\pi(t - t_0)^2 / T] \quad (35)$$

where T and t_0 are constants, and both equal to 2×10^{-9} . In such a case, the highest frequency of interest is 1 GHz. The observation point is set at the back of the plate and is 50mm far from the plate.

Applying the FDTD method to compute the time domain electric field component E_z at the observation point, to simulate the apertures precisely, the cell size around the aperture must be small. We choose $\Delta x = \Delta z = 0.5$ mm around the apertures. The cell size Δy is set to be 25mm. To satisfy the stability condition of the FDTD algorithm, the time-step size for the conventional FDTD is $\Delta t \leq 1.17$ ps. For the WCS-DTD and IWCS-FDTD scheme, the maximum time increment is only related to the space increments Δy , that is, $\Delta t \leq 83.33$ ps. Five-cell-thick CPML layers are used to terminate the grid, and are placed five cells from the metal plate on all sides. The implementation of the plane wave is same as that of conventional FDTD method. The metal plate is viewed as a perfect electronic conductor and the tangential electric field values at the metal plate should to be zeros.

In the WCS-FDTD method, the E_x and E_z components at the metal plate are set zeros directly after they are updated by using eqs. (2) and (3); while in the IWCS-FDTD method, the

PEC boundary condition for the E_x and E_z components are implemented following the strategy described in reference [8], by incorporating the PEC condition into the solving of the tri-diagonal matrices.

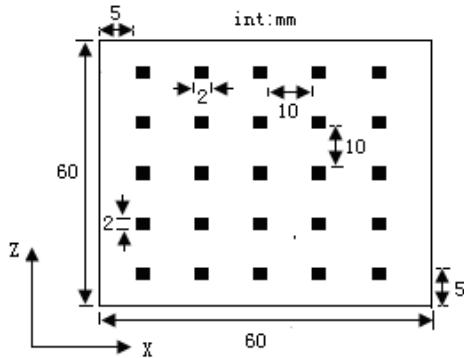


Fig. 1. Geometric configuration of the metal plate.

We perform the numerical simulation for an 83 ns time history by using the IWCS-FDTD method under time step size 83.33ps. The result is shown in Fig. 2. The total time steps are almost 1,000. It can be seen from Fig.1 that no instability problem is observed, which numerically validates the stability condition of eq. (34).

To demonstrate the high computational efficiency and accuracy of the IWCS-FDTD method, we perform the numerical simulations for a 5 ns time history by using the conventional FDTD, WCS-FDTD, and IWCS-FDTD methods, and compare the computation times and accuracy of these methods. In the conventional FDTD method, the time-step size keeps a constant of 1.17 ps, while in the WCS-FDTD and IWCS-FDTD methods, we use time-step size 83.33 ps.

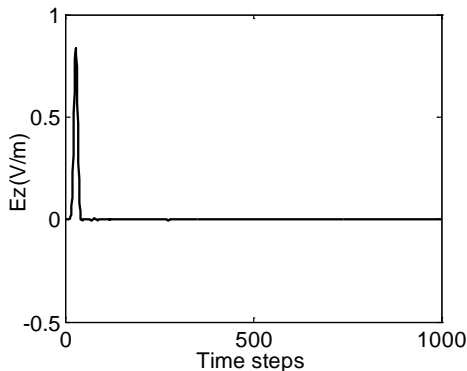


Fig. 2. Numerical result using IWCS-FDTD method with time step size 83.33ps.

Figure 3 shows the electric field component E_z at observation point calculated by using the conventional FDTD, WCS-FDTD, and IWCS-FDTD methods. It can be seen from this figure that only the result calculated by the IWCS-FDTD method agrees well with the result calculated by the conventional FDTD method. The result calculated by the WCS-FDTD method deviates from that of the conventional FDTD method significantly.

It is apparent that the IWCS-FDTD method has higher accuracy than the WCS-FDTD method in the implementation of the PEC condition. The reason for the inaccuracy of WCS-FDTD method is that, in the WCS-FDTD method, updating of H_y component needs the unknown E_x and E_z components at the same time step, thus, implementation of the PEC condition for the E_x and E_z components must be incorporated into the solving of the H_y component. The WCS-FDTD method neglects this and results in serious error in the implementation of the PEC condition.

To complete this simulation, the computation times for the conventional FDTD method, WCS-FDTD method and IWCS-FDTD method are 41.18, 5.05, and 5.37 minutes, respectively. Due to large time step size applied, the CPU time for the WCS-FDTD and IWCS-FDTD methods are almost 1/8 of that for the conventional FDTD method.

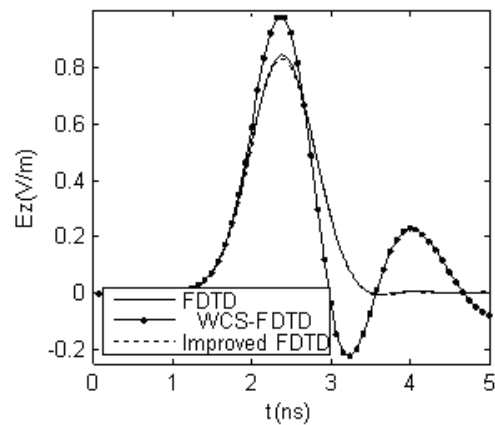


Fig. 3. The comparison of the results calculated by using the conventional FDTD, WCS-FDTD, and IWCS-FDTD methods

V. CONCLUSION

An improved weakly conditionally stable FDTD method is presented in this paper to circumvent the inaccuracy in the implementation of the perfect-electric-conductor condition in the WCS-FDTD method. The stability condition of the IWCS-FDTD scheme is presented analytically and the numerical performance of the proposed method over the WCS-FDTD method is demonstrated through numerical example.

ACKNOWLEDGMENT

This work was supported by National Natural Science Foundations of China (No. 61001039), and also supported by the Research Fund for the Doctoral Program of Higher Education of China (No.20090201120030)

REFERENCES

- [1] K. S. Yee, "Numerical Solution of Initial Boundary Value Problems Involving Maxwell's Equations in Isotropic Media," *IEEE Trans. Antennas Propagat.*, vol. 14, pp. 302-307, 1966.
- [2] A. Taflove, *Computational Electrodynamics*, Norwood, MA: Artech House, 1995.
- [3] F. Zheng, Z. Chen, and J. Zhang, "A Finite-Difference Time-Domain Method Without the Courant Stability Conditions," *IEEE Microwave Guided Wave Lett.*, vol. 9, pp. 441-443, 1999.
- [4] T. Namiki, "3-D ADI-FDTD Method-Unconditionally Stable Time-Domain Algorithm for Solving Full Vector Maxwell's Equations," *IEEE Trans. Microwave Theory Tech.*, vol. 48, pp. 1743-1748, 2000.
- [5] G. Sun and C. W. Trueman, "Some Fundamental Characteristics of the One-Dimensional Alternate-Direction-Implicit Finite-Difference Timedomain Method," *IEEE Trans. Microwave Theory Tech.*, vol. 52, pp. 46-52, 2004.
- [6] M. Darms, R. Schuhmann, H. Spachmann, and T. Weiland, "Dispersion and Asymmetric Effects of ADI-FDTD," *IEEE Microwave Wireless Components Lett*, vol. 12, pp. 491-493, 2002.
- [7] N. V. Kantartzis, "Multi-Frequency Higher-Order ADI-FDTD Solvers for Signal Integrity Predictions and Interference Modeling in General EMC Applications," *Applied Computational Electromagnetic Society (ACES) Journal*, vol. 25, pp. 1046-1060, 2010.
- [8] J. Chen and J. Wang, "An Unconditionally Stable Subcell Model for Thin Wires in the ADI-FDTD Method," *Applied Computational Electromagnetic Society (ACES) Journal*, vol. 25, pp. 659-664, 2010.
- [9] G. Sun and C. W. Trueman, "Accuracy of Three Unconditionally-Stable FDTD Schemes for Solving Maxwell's Equations," *Applied Computational Electromagnetic Society (ACES) Journal*, vol. 18, pp. 41-47, 2003.
- [10] G. Sun and C. W. Trueman, "An Unconditionally-Stable FDTD Method Based on the Crank-Nicolson Scheme for Solving the Three-Dimensional Maxwell's Equations," *Electron. Lett.*, vol. 40, pp. 589-590, 2004.
- [11] J. Chen and J. Wang, "PEC Condition Implementation for the ADI-FDTD Method," *Microwave Opt. Technol. Lett.*, vol. 49, pp. 526-530, 2007.
- [12] I. Ahmed and Z. Chen, "Error Reduced ADI-FDTD Methods," *IEEE Antennas Wireless Propag. Lett*, vol. 4, pp. 323-325, 2005.
- [13] J. Chen and J. Wang, "Weakly Conditionally Stable Finite-Difference Time-Domain Method", *IET Microwaves, Antennas & Propagation*, vol. 4, pp. 1927-1936, 2010.
- [14] J. Chen and J. Wang, "A Frequency-Dependent Weakly Conditionally Stable Finite-Difference Time-Domain Method for Dispersive Materials," *Applied Computational Electromagnetic Society (ACES) Journal*, vol. 25, pp. 665-671, 2010.



Juan Chen was born in Chongqing, China, in 1981. She received the Ph.D. degree in Electromagnetic Field and Microwave Techniques at the Xi'an Jiaotong University, Xi'an, China, in 2008. She now serves as an associate professor at Xi'an Jiaotong University. Her research interests are the numerical electromagnetic methods, antenna designs, and electromagnetic compatibility.

Dual Band-Notch Small Square Monopole Antenna with Enhanced Bandwidth Characteristics for UWB Applications

M. Ojaroudi ¹, N. Ojaroudi ², and Y. Ebazadeh ³

¹ Young Research Group
Ardabil Branch, Islamic Azad University, Ardabil, Iran
m.ojaroudi@iauardabil.ac.ir

² Department of Electrical Engineering
Ardabil Branch, Islamic Azad University, Ardabil, Iran
n.ojaroudi@yahoo.com

³ Department of Computer Engineering
Germi Branch, Islamic Azad University, Germi, Iran
y.ebazadeh@iaugermi.ac.ir

Abstract — This article proposes a novel printed monopole antenna for ultra wideband applications with dual band-notch function. The antenna consists of a square radiating patch with four rectangular slits and a ground plane with a pair of T-shaped parasitic structures, which provides a wide usable fractional bandwidth of more than 165% (2.79-14.83 GHz). In order to generate single band-notch characteristics, we use two rectangular slits in the corners of square radiating patch. By adding two rectangular slits in the center of the modified radiating patch, a dual band notch function is achieved and also by inserting a pair of T-shaped parasitic structures in the ground plane, additional resonances are excited and hence much wider impedance bandwidth can be produced, especially at the higher band. The measured results reveal that the presented dual band-notch monopole antenna offers a very wide bandwidth with two notched bands, covering all the 5.2/5.8GHz WLAN, 3.5/5.5 GHz WiMAX and 4-GHz C bands. The designed antenna has a small size of $12 \times 18 \text{ mm}^2$.

Index Terms — Dual band notch function, square monopole antenna, ultra-wideband (UWB) applications.

I. INTRODUCTION

In UWB communication systems, one of the key issues is the design of a compact antenna while providing wideband characteristic over the whole operating band. Consequently, a number of microstrip antennas with different geometries have been experimentally characterized. Moreover, other strategies to improve the impedance bandwidth which do not involve a modification of the geometry of the planar antenna have been investigated [1-4].

The frequency range for UWB systems between 3.1 to 10.6 GHz will cause interference to the existing wireless communication systems, such as, the wireless local area network (WLAN) for IEEE 802.11a operating in 5.15–5.35 GHz and 5.725–5.825 GHz bands, WiMAX (3.3–3.6 GHz and C-band (3.7–4.2 GHz), so the UWB antenna with a single and dual band-stop performance is required. Recently to generate the frequency band-notch function, modified planar monopoles have been recently proposed [5-10]. In [5] and [6], different shapes of the slits (i.e., W-shaped and folded trapezoid) are used to obtain the desired band notched characteristics. Multiple [7] half-wavelength U-shaped slits are embedded in the radiation patch to generate the single and multiple

band-notched functions, respectively. In [8], band-notch function is achieved by using a T-shaped coupled-parasitic element in the ground plane.

In this paper, a new dual band-notched printed monopole antenna with multi resonance performance is presented. In the proposed structure, single band-notch function is provided by cutting two rectangular slits in the corners of the square radiating patch and dual band-notch characteristic is obtained by cutting four rectangular slits in the radiating patch. Finally by inserting a pair of T-shaped parasitic structures on the ground plane, additional resonances are excited and the bandwidth is improved that achieves a fractional bandwidth with multi resonance performance of more than 165%.

II. ANTENNA DESIGN

As shown in Fig. 1, the proposed monopole antenna is fed by a microstrip line and it is printed on a FR4 substrate of thickness 1.6 mm. As shown in Fig. 1, the proposed antenna consists of a square radiating patch with four rectangular slits and a ground plane which is partially modified with two T-shaped parasitic structures. The basic antenna structure consists of a square patch, a feedline, and a ground plane. The square patch has a width W . As can be seen in Fig. 1, the width and length of the feed line, which is connected to the patch are W_f and L_f , respectively. On the other side of the substrate, a conducting ground plane of width W_{sub} and length L_{gnd} is placed. The width W_f of the microstrip feedline is fixed at 2 mm. The proposed antenna is connected to a 50Ω SMA connector for signal transmission.

In this study, four modified rectangular slits with variable dimensions are used in order to generate the dual frequency band-stop performance, as displayed in Fig. 1. These slits can create additional surface current paths in the antenna therefore perturb the resonant response [7]. At the notch frequencies, the current flows are more dominant around these slits, and they are oppositely directed between the slits edges [10]. Also T-shaped parasitic structures play an important role in the broadband characteristics of this antenna because they can achieve additional resonances and improve the bandwidth [10]. In other words, the impedance bandwidth is effectively improved at the upper frequency that

can be regarded as a parasitic resonator electrically to the square monopole.

The optimal dimensions of the designed antenna are as follows: $W_{sub} = 12\text{mm}$, $L_{sub} = 18\text{mm}$, $h_{sub} = 1.6\text{mm}$, $W = 10\text{mm}$, $W_f = 2\text{mm}$, $L_f = 7\text{mm}$, $W_{S3} = 0.5\text{mm}$, $L_S = 8.75\text{mm}$, $W_{S1} = 2\text{mm}$, $L_{S1} = 9\text{mm}$, $L_X = 0.5\text{mm}$, $W_X = 1\text{mm}$, $W_P = 1.2\text{mm}$, $L_P = 8\text{mm}$, $W_{P1} = 2.75\text{mm}$, $L_{P1} = 3.5\text{mm}$, $W_{P2} = 0.5\text{mm}$ and $L_{gnd} = 3.5\text{mm}$.

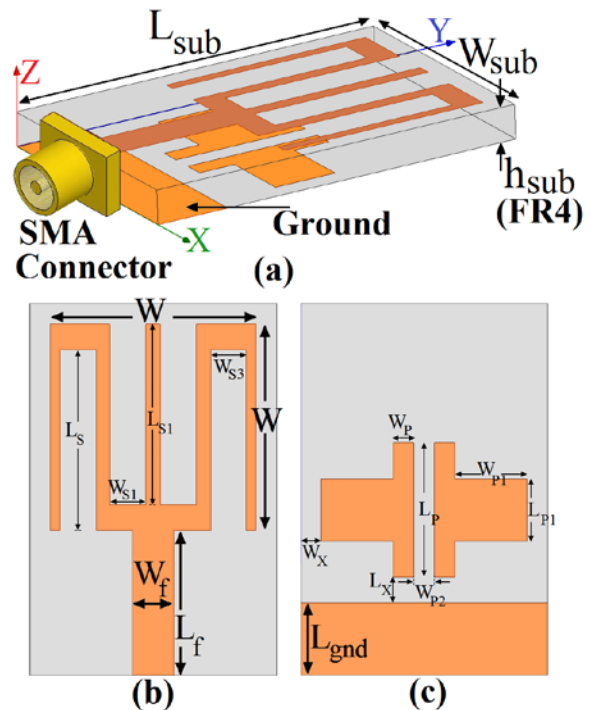


Fig. 1. Geometry of proposed antenna with four rectangular slits and a pair of T-shaped parasitic structures, (a) side view, (b) top view, (c) bottom view.

III. RESULTS AND DISCUSSIONS

The microstrip-fed monopole antenna was constructed and studied to demonstrate the effect of the proposed dual band-notch function and bandwidth enhancement technique. The numerical and experimental results of the input impedance and radiation characteristics are presented and discussed. The parameters of this proposed antenna are studied by changing one or two parameters at a time and while others are fixed.

The simulated results are obtained using the Ansoft simulation software high-frequency structure simulator (HFSS) [12].

Figure 2 shows the structures of various antennas used for simulation studies. Return loss characteristics for ordinary square patch antennas (Fig. 2(a)), with a pair of rectangular slits (Fig. 2(b)), and with four rectangular slits (Fig. 2(c)) are compared in Fig 3. As shown in Fig. 3, in the proposed antenna configuration, the ordinary square monopole can provide the fundamental and next higher resonant radiation band at 4.3 and 8.2 GHz, respectively. In order to generate single band-notch characteristics, two rectangular slits are used at the corners of square radiating patch. By adding two rectangular slits in the center of modified radiating patch a dual band-notch function is achieved that covering all the 5.2/5.8GHz WLAN, 3.5/5.5 GHz WiMAX and 4-GHz C bands. Also the input impedance of the proposed antenna structure and the various monopole antenna structures that are shown in Fig. 2, are shown in Fig. 4.

To understand the phenomenon behind this dual band-notch performance, the simulated current distribution on the modified radiating patch for the proposed antenna without T-shaped parasitic structures at the notch frequencies of 3.8 GHz and 5.5 GHz is presented in Fig. 5(a) and 5(b), respectively. As it can be observed in Fig. 5(a), 5(b), the current is concentrated on the edges of the interior and exterior of the rectangular slits at 3.8 GHz and 5.5 GHz. Therefore, the antenna impedance changes at these frequencies due to the band-notch properties of the rectangular slits.

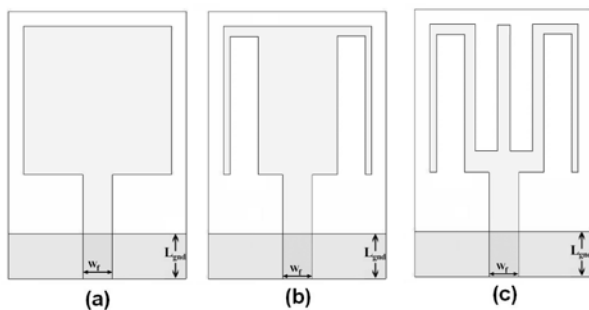


Fig. 2. (a) The ordinary square antenna, (b) the square antenna with two rectangular slit in corners, (c) the square antenna with four rectangular slits.

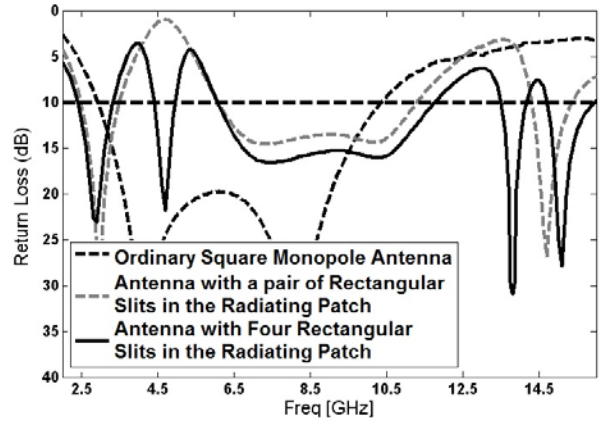


Fig. 3. Simulated return loss characteristics for antennas shown in Figure 2.

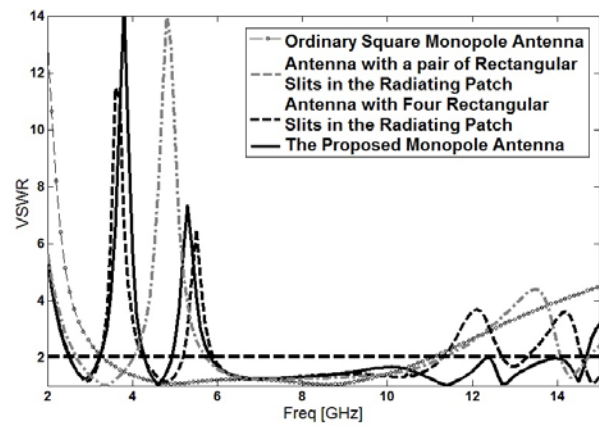


Fig. 4. Simulated VSWR characteristics for the proposed antenna structure and antennas shown in Figure 2.

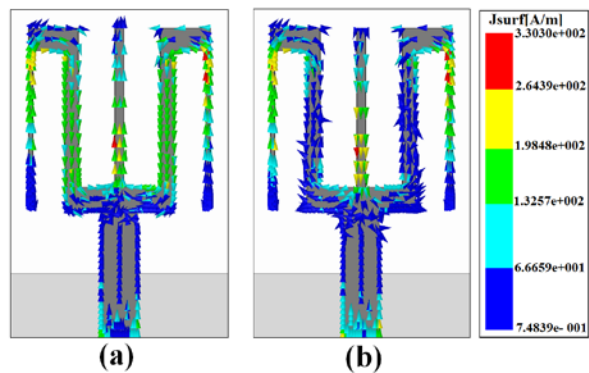
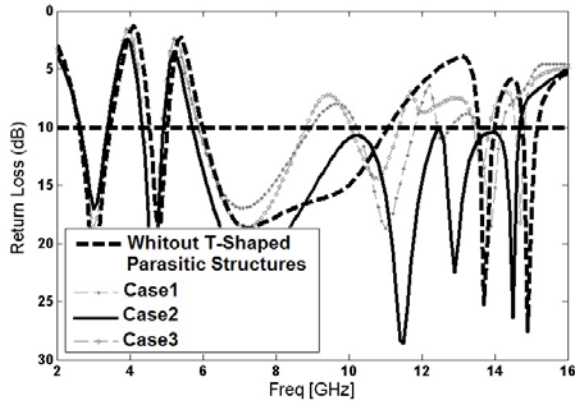


Fig. 5. Simulated surface current distributions on the radiating patch for (a) the proposed antenna without T-shaped parasitic structures at first band-notch central frequency (3.8 GHz), (b) the proposed antenna without T-shaped parasitic structures at second band-notch central frequency (5.5 GHz).

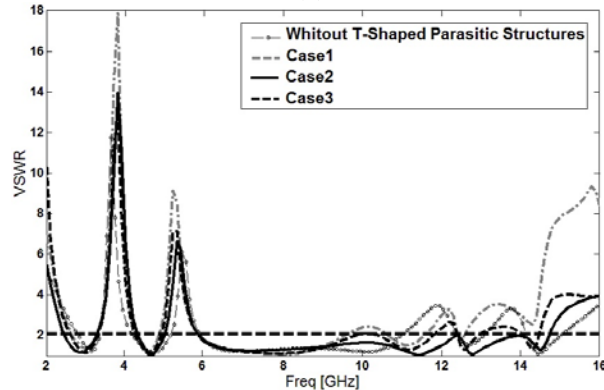
In order to increase the upper frequency bandwidth, two T-shaped parasitic structures are inserted in the ground plane of the proposed antenna, as displayed in Fig. 1. Three such T-shaped parasitic structures with different sizes are specified in Table I as cases 1, 2 and 3.

Table 1: Three cases of proposed antenna with different values of T-shaped parasitic structures

Case	L_{P1} (mm)	L_P (mm)	W_{P1} (mm)	W_P (mm)
1	3	9	3.5	1
2	3.5	8	2.75	1.2
3	5	7	1	1.5



(a)



(b)

Fig. 6. Simulated return loss and VSWR characteristics for the proposed antenna without T-shaped parasitic structures and three cases 1, 2 and 3 with it as shown in Table 1.

Figure 6 shows the effects of T-shaped parasitic structures with different values on the impedance matching in comparison with the same antenna without them. It is found that by inserting the T-

shaped parasitic structures with suitable dimensions in the ground plane additional resonances are excited and hence much wider impedance bandwidth with multi-resonance characteristics can be produced, especially at the higher frequencies.

The simulated VSWR curves with different values of L_S are plotted in Fig. 7. As shown in Fig. 6, when the height of the slits increases from 5.25 to 9.25 mm, the center of lower notch frequency is decreased from 4.8 to 3.45 GHz and also the center of higher notch frequency is decreased from 6.5 to 4.9 GHz. From these results, we can conclude that the notch frequency is controllable by changing the interior height of the corner slit.

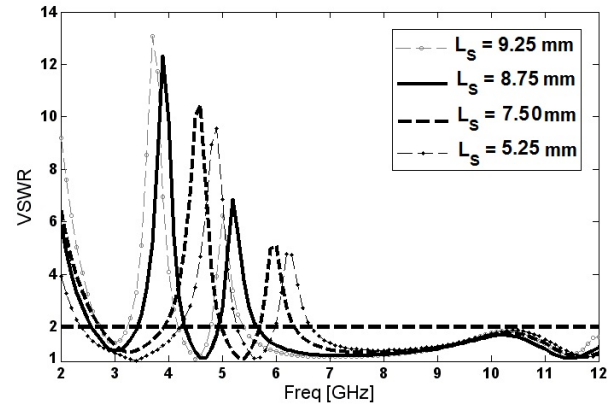


Fig. 7. Simulated VSWR characteristics for various values of L_S .

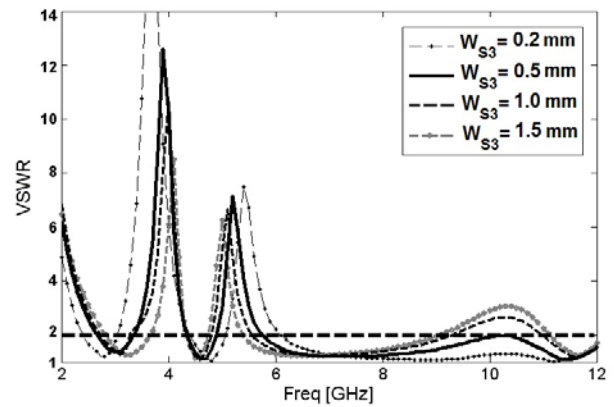


Fig. 8. Simulated VSWR characteristics for various values of W_{S3} .

Figure 8 illustrates the simulated VSWR characteristics with various values of W_{S3} . As the

width W_{S3} increases from 0.2 to 1.5 mm, the filter bandwidth is varied from 0.6 to 1.3 GHz for lower notch frequency and also varied from 0.8 to 1.2 GHz for higher notch frequency.

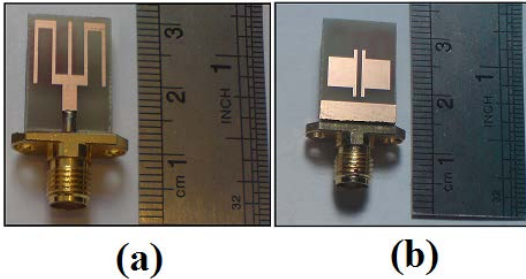


Fig. 9. Photograph of the realized antenna, (a) top view, (b) bottom view.

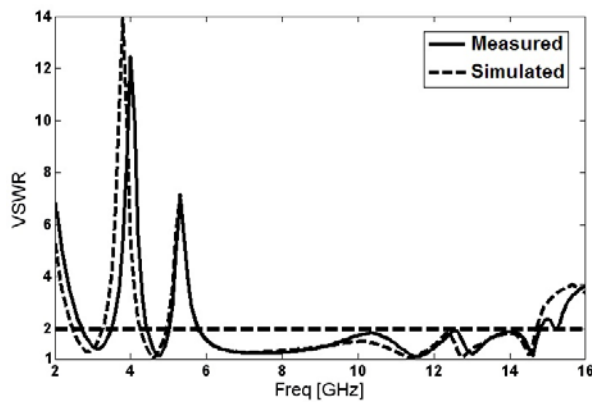


Fig. 10. Measured and simulated VSWR for the proposed antenna.

A prototype of the proposed monopole antenna, as shown in Fig. 9, was fabricated and tested in the Antenna Laboratory at Microwave Technology Company (MWT), and the VSWR were measured using a HP 8720ES network analyzer in an anechoic chamber. Figure 10 shows the measured and simulated VSWR characteristics of the proposed antenna. The fabricated antenna has the frequency band of 2.79 to over 14.83 GHz with two rejection bands around 3.45-4.23 and 5.07–5.89 GHz. As shown in Fig. 10, there exists a discrepancy between measured data and the simulated results which could be due to the effect of the SMA port. In order to confirm the accurate return loss characteristics for the designed antenna, it is recommended that the manufacturing and measurement processes need to be performed carefully.

The difference in the measured and simulated results in Fig. 10 can also be due to the use of FR4. The designed and fabricated FR4 substrate might not have the same dielectric constant value. As in reality the dielectric constant of an FR4 substrate usually can be anything from 4.1 - 4.9 GHz.

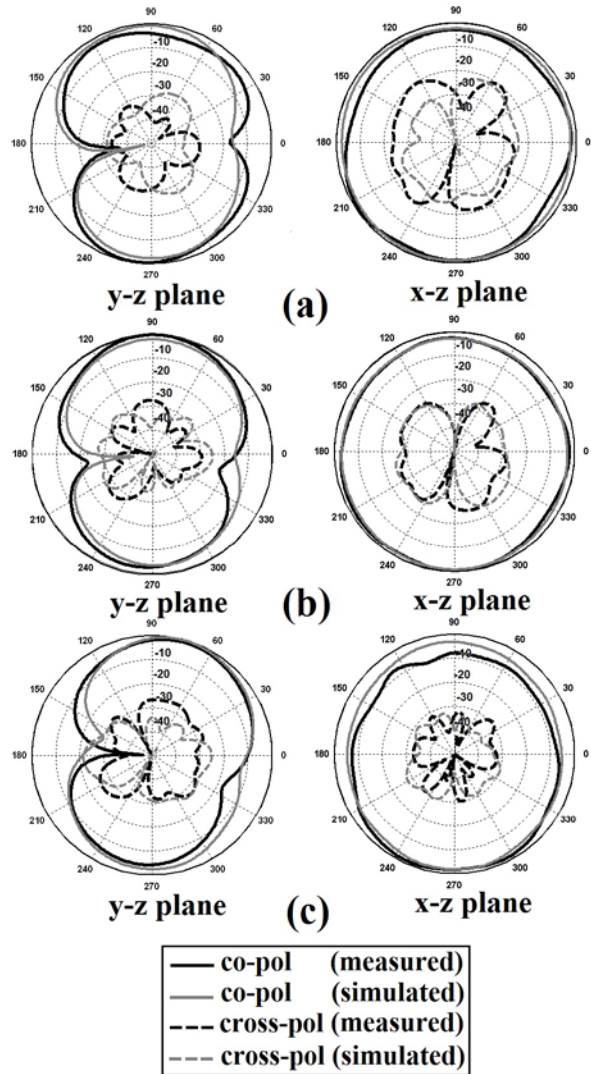


Fig. 11. Measured and simulated radiation patterns of the proposed antenna. (a) 4.8 GHz, (b) 7.5 GHz, and (c) 10 GHz.

The radiation patterns have been measured inside an anechoic chamber. Figure 11 shows the measured and simulated radiation patterns including the co-polarization and cross-polarization in the H -plane (x - z plane) and E -plane (y - z plane). The main purpose of the radiation patterns is to demonstrate that the antenna actually

radiates over a wide frequency band. It can be seen that the radiation patterns in x - z plane are nearly omnidirectional for the three frequencies. As shown in Fig. 11, the measured radiation patterns agree very well with the simulated results at the three frequencies.

Figure 12 shows the effects of the rectangular slits, and T-shaped parasitic structures on the maximum gain in comparison with the same antenna without them. As shown in Fig. 12, the basic antenna has a gain that is low at 2 GHz and increases with frequency. It is found that the gain of the square antenna is decreased with the use of the rectangular slits, and T-shaped parasitic structures. It can be observed in Fig. 12 that by using a square radiating patch with a four rectangular slits and two T-shaped parasitic structures, two sharp decrease of maximum gain in the notched frequencies band at 3.9 and 5.5 GHz are shown. For other frequencies outside the notched frequencies band, the antenna gain with the filter is similar to those without it. A two-antenna technique is used to measure the radiation gain. It can be seen that for the frequency notch band the gain is negative, which is expected based on the return loss and VSWR measurements.

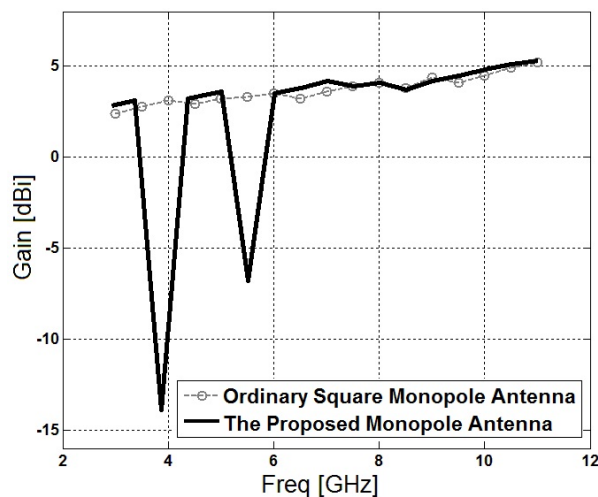


Fig. 12. Measured maximum gain comparisons for the ordinary square antenna and the proposed antenna.

V. CONCLUSION

In this paper, a novel compact wideband planar monopole antenna (PMA) with variable single and dual band-notched characteristics has been proposed for various UWB applications. The

fabricated antenna has the frequency band of 2.79 to over 14.83 GHz with two rejection bands around 3.3-4.23 and 5.07-5.89 GHz. By cutting four rectangular slits with variable dimensions on the square radiating patch, dual band-notch characteristics generated and also by inserting two inverted T-shaped conductor-backed plane, additional resonances are excited and hence much wider impedance bandwidth can be produced, especially at the higher band. The proposed antenna has a simple configuration and is easy to fabricate. Experimental results show that the proposed antenna could be a good candidate for UWB applications.

ACKNOWLEDGMENT

The authors are thankful to Microwave Technology (MWT) Company staff for their beneficial and professional help (www.microwave-technology.com).

REFERENCES

- [1] M. Ojaroudi, Sh. Yzdanifard, N. Ojaroudi, and M. Nasser-Moghaddasi, "Small Square Monopole Antenna with Enhanced by Using Inverted T-Shaped Slot and Conductor-Backed Plane," *IEEE Transactions on Antenna and Propagation*, vol. 59, no. 2, pp. 670-674, February 2011.
- [2] A. T. Mobashsher, M. T. Islam, N. Misran, "Wideband Compact Antenna with Partially Radiating Coplanar Ground Plane," *Applied Computational Electromagnetics Society (ACES) Journal*, vol. 26, no. 1, pp. 73-81, January 2011.
- [3] M. Ojaroudi, Ch. Ghobadi, and J. Nourinia, "Small Square Monopole Antenna with Inverted T-Shaped Notch in the Ground Plane for UWB Application," *IEEE Antennas and Wireless Propagation Letters*, vol. 8, no. 1, pp. 728-731, 2009.
- [4] J. William, R. Nakkeeran, "A New UWB Slot Antenna with Rejection of WiMax and WLAN Bands," *Applied Computational Electromagnetics Society (ACES) Journal*, vol. 25, no. 9, pp. 787-793, September 2010..
- [5] Sh. Yazdanifard, R. A. Sadeghzadeh, and M. Ojaroudi, "Ultra-Wideband Small Square Monopole Antenna with Variable Frequency Band-Notch Function," *Progress In Electromagnetics Research C*, vol. 15, pp. 133-144, 2010.
- [6] M. Ojaroudi, Gh. Ghanbari, N. Ojaroudi, and Ch. Ghobadi, "Small Square Monopole Antenna for UWB Applications with Variable Frequency Band-Notch Function," *IEEE Antennas and Wireless Propagation Letters*, vol. 8, pp. 1061-1064, 2009.

- [7] K. Chung, S. Hong, and J. Choi, "Ultrawideband Printed Monopole Antenna with Band-Notch Filters," *Microw. Antennas, Prorag.*, vol. 1, no. 2, pp. 518-522, Apr. 2007.
- [8] M. Ojaroudi, Sh. Yzdanifard, N. Ojaroudi, and R. A. Sadeghzadeh, "Band-Notched Small Square-Ring Antenna with a Pair of T-Shaped Strips Protruded Inside the Square Ring for UWB Applications," *IEEE Antennas and Wireless Propagation Letters*, vol. 10, pp. 227-230, 2011.
- [9] Q. Wu, R. Jin, J. Geng, and J. Lao, "Ultra-Wideband Rectangular Disk Monopole Antenna with Notch Ground," *Electron. Lett.*, vol. 43, no. 11, pp. 1100-1101, May 2007.
- [10] D. S. Javan, O. H. Ghouchani, "Cross Slot Antenna with U-Shaped Tuning Stub for Ultra Wideband Applications," *Applied Computational Electromagnetics Society (ACES) Journal*, vol. 24, no. 4, pp. 427-432, August 2009.
- [11] M. Naghshvarian-Jahromi, N. Komjani-Barchloui, "Analysis of the Behavior of Sierpinski Carpet Monopole Antenna," *Applied Computational Electromagnetics Society (ACES) Journal*, vol. 24, no. 1, pp. 32-36, February 2009.
- [12] Ansoft High Frequency Structure Simulation (HFSS), Ver. 13, Ansoft Corporation, 2010.



Mohammad Ojaroudi was born on 1984 in Germe, Iran. He received his B.Sc. degree in Power Electrical Engineering from Azad University, Ardabil Branch and M.Sc. degree in Telecommunication Engineering from Urmia University. From 2010, he is working toward the

Ph.D. degree at Shahid Beheshti University. From 2007 until now, he is an Teaching Assistant with the Department of Electrical Engineering, Islamic Azad University, Ardabil Branch, Iran. Since March 2008, he has been a Research Fellow (Chief Executive Officer) in the Microwave Technology Company (MWT), Tehran, Iran. His research interests include analysis and design of microstrip antennas, design and modeling of microwave structures, radar systems, and electromagnetic theory. He is author and coauthor of more than 60 journal and international conference papers.



Nasser Ojaroudi was born on 1986 in Germe, Iran. He received his B.Sc. degree in Electrical Engineering from Azad University, Ardabil Branch. From 2011, he is working toward the M.Sc. degree in Telecommunication Engineering at Shahid Rajae Teacher Training

University. Since March 2008, he has been a Research Fellow in the Microwave Technology Company (MWT), Tehran, Iran. His research interests include monopole antenna, slot antennas, microstrip antennas for radar systems, ultra-wideband (UWB) and small antennas for wireless communications, microwave passive devices and circuits, and microwave/millimeter systems.



Yaser Ebazadeh was born on 1981 in Germe, Iran. He received his B.Sc. degree in software Engineering from Tabriz University. From 2011, he is working toward the M.Sc. degree in Computer Engineering at Azarbayjan Shraghi Branch,

Science and Research, Islamic Azad University, Tabriz, Iran. He is IT manager of Germe Branch, Islamic Azad University, Germe, Iran. His research interests include Information Security Systems, WiMAX technology simulation in ns-2 simulator and advanced antenna technology in WiMAX.

Optimal Design of an Ultra-Wideband Antenna with the Irregular Shape on Radiator using Particle Swarm Optimization

Wei-Chung Weng

Department of Electrical Engineering
National Chi Nan University, Puli 54561, Taiwan
wcweng@ncnu.edu.tw

Abstract — An ultra-wideband antenna with an irregular shape radiator for ultra-wideband applications has been designed by particle swarm optimization along with the simulator, HFSS. The proposed antenna design process is automated. Also, the better results can be obtained efficiently. The proposed antenna is fed by a coplanar waveguide line. The optimized antenna has a compact substrate size of 34.0 mm by 33.35 mm. Results show that the optimized irregular shape of the proposed antenna outperforms the antennas with uniform rectangular shapes in impedance matching. The optimized antenna can cover the spectrum of ultra-wideband (3.1 GHz - 10.6 GHz). The current distributions are investigated for describing the antenna characteristics. Moreover, the proposed UWB antenna has good characteristics of radiation, transmission, and impedance bandwidth.

Index Terms — Optimization, planar antennas, PSO, ultra-wideband.

I. INTRODUCTION

Ultra-wideband (UWB) [1] antennas have been received much attention from antenna designers and researchers. Many UWB antennas were designed using planar structure due to advantages of low profile, low cost, light weight, and easy fabrication. The dimensions and geometry of the radiator largely affect the impedance matching. To achieve the design goal, some of planar UWB antennas adopted different shapes such as rectangle [2, 3], circle [4], triangle [5], and octagon [6] as the radiators. Other studies used the staircase-shape on the edges of the

radiators [7, 8]. However, those shapes have uniform or smooth edges on the radiator and the dimensions of the radiator were determined by experimental efforts.

This study uses the particle swarm optimization (PSO) method, combined with the finite element method based simulator, HFSS, to design and optimize the proposed UWB antenna. The radiator of the proposed UWB antenna consists of five rectangular patches. The dimension of each rectangular patch can be arbitrarily adjusted by the PSO method to achieve the design goal. Hence, the shape of the optimized radiator would be various. The developed PSO method can control the HFSS and can change the antenna dimensions without any manual adjustments during the optimization process. In this way, optimized results are obtained automatically. The main advantage of the proposed approach is that it reduces the time required to solve an electromagnetic problem. The better results can be obtained efficiently. Compared with the studies shown in [2-8], the irregular shape radiator obtained by the proposed approach can be considered as novel.

The PSO is an effective algorithm which was proposed in 1995 by James Kennedy and Russell Eberhart jointly [9]. Many electromagnetic problems [10-12] have been designed using PSO. The basic concept of PSO is from the study on animals' group behaviors, such as a swarm of birds randomly searching for food. The birds (particles) distribute randomly and fly with random direction and velocity in a finite area initially. If one of the birds finds a location close to the food (the optimum), the bird changes its flying direction and velocity toward the food.

Simultaneously, the bird tells other birds to fly around the bird. The other birds would change their direction and velocity to get closer to the food. The birds search for the entire space until one of them finds the food. The PSO algorithm is inspired from this model. For the sake of brevity, other detailed concepts of PSO are excluded here and they can be found in [13].

Optimized dimensions of the proposed planar UWB antenna is fabricated on a cheap FR4 substrate. The antenna radiator is fed by a coplanar waveguide (CPW) line [14]. A good impedance matching is obtained in the UWB spectrum. Moreover, a reasonable agreement between simulated reflection coefficient and measured one is observed. Simulated results show that near omnidirectional radiation patterns are achieved. A parametric study was performed by simulation. This result shows that the optimized irregular shape of the proposed antenna outperforms the antennas with uniform rectangular shapes on the radiators in impedance matching. Good frequency-domain characteristics of maximum gain, group delay and phase of S_{21} were measured. The results verified that the proposed UWB antenna can apply to any short- or long-range communication systems.

Table 1: The dimensions and optimization ranges of the initial antenna (Unit: mm)

Parameter	Size	Optimization range
L0	5.0	0.5 - 7.0
Lg	15.0	9.0 - 17.0
Wg	15.0	16.0 - 26.0
L1	5.0	1.0 - 7.0
W1	4.4	0.5 - 8.0
L2	5.0	1.0 - 7.0
W2	4.6	0.5 - 8.0
L3	5.0	1.0 - 7.0
W3	4.8	0.5 - 8.0
L4	5.0	1.0 - 7.0
W4	5.0	0.5 - 8.0
L5	5.0	1.0 - 7.0
W5	5.2	0.5 - 8.0

II. PSO AND ANTENNA DESIGN

Figure 1 shows the geometry of the initial antenna whose radiator consisting of five different rectangular patches. Before the optimization, the initial antenna was created in the full-wave

electromagnetic simulator, HFSS. In the PSO optimization, the optimizer has more flexibility when there are more numbers of parameters to be optimized. At the same time, more numbers of EM simulations is required in iteration. To compromise the order of complexity and flexibility, five rectangular patches of the radiator are adopted in this study. Table 1 lists the dimensions of the initial antenna. Five rectangular patches are denoted L1 to L5 and W1 to W5. The sizes of them are used for creating the initial antenna only. The initial values of five rectangular patches do not affect the optimization result since the PSO is a global optimizer. It is not required using any starting points in the optimization process of the PSO. The gap between the radiator and ground is L0. The length and width of the ground plane are Lg and 2Wg, respectively. The W0 (4.2 mm) and G (0.3 mm) are the width and the gap of the 50 Ω CPW, respectively. The W0 and G are fixed during optimization. The proposed antenna is to be fabricated on an FR4 substrate with thickness of 0.8 mm, relative permittivity of 4.4, and loss tangent of 0.02. In this optimization, thirteen parameters, L0, Lg, Wg, L1 to L5, and W1 to W5 are to be optimized within their optimization range to achieve the UWB specification. If the designer wants the antenna to

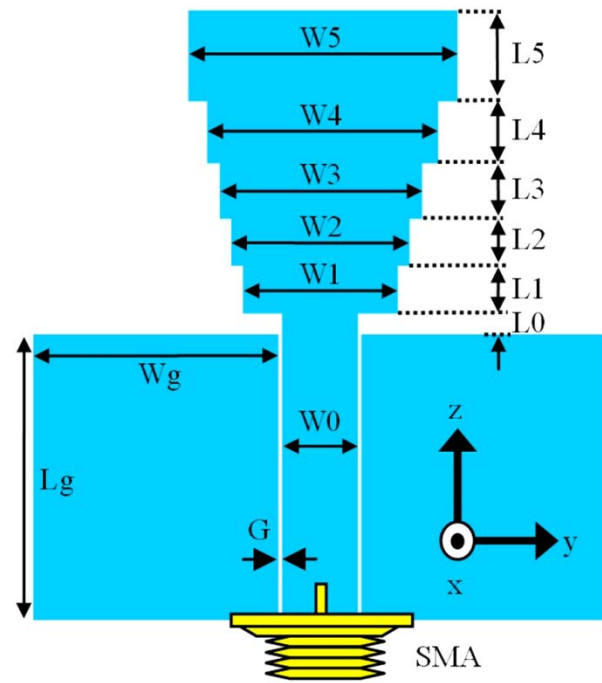


Fig. 1. The geometry of the initial antenna.

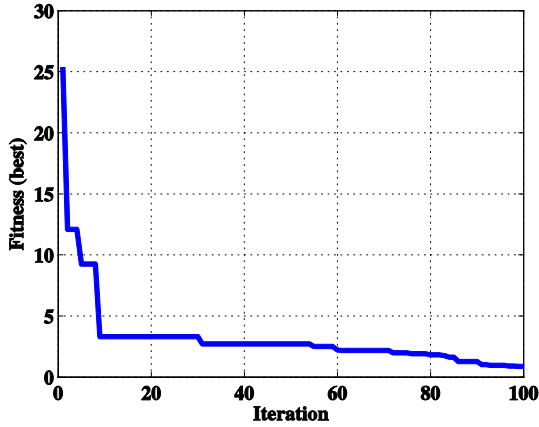


Fig. 2. The best fitness versus iteration.

Table 2: The dimensions of the optimized antennas (Unit: mm)

Parameter	Size	Parameter	Size
W0	4.2	L0	1.35
Wg	14.28	Lg	15.87
W1	13.97	L1	2.67
W2	12.77	L2	2.66
W3	15.49	L3	3.0
W4	16.0	L4	3.79
W5	11.29	L5	4.66

be compact, the designer may limit the optimization ranges of parameters. The reflection coefficient $|S_{11}|$ of the optimized antenna should be below -10 dB in the UWB spectrum (frequency between 3.1 GHz to 10.6 GHz).

To optimize the proposed antenna using PSO and HFSS, the first step is to create a script of HFSS. The HFSS script is recorded while creating the geometry of the initial antenna. The PSO serves as an external optimizer to control the HFSS. The next step is to modify the value of each parameter in the script. The PSO code can identify and modify the dimension of each parameter in the script. The HFSS simulates the antenna using the modified geometry to obtain the simulated results. The fitness is then used to evaluate the obtained results for PSO optimization process. In this study, the obtained $|S_{11}|$ is used to calculate the fitness using (1).

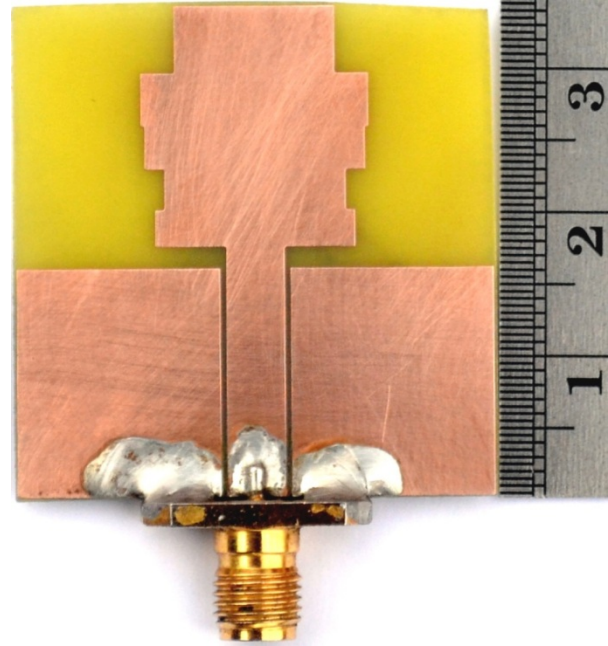


Fig. 3. The fabricated antenna on an FR4 substrate with the antenna size of 34.0 mm by 33.35 mm.

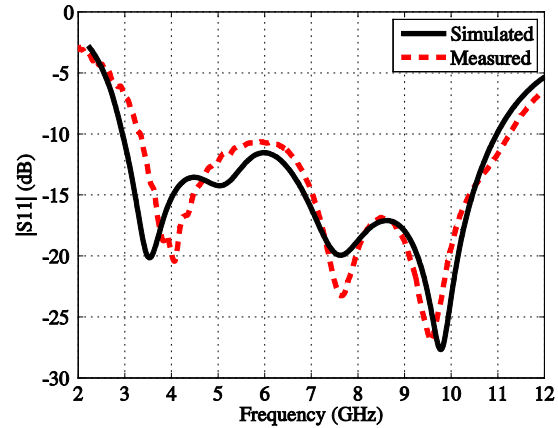


Fig. 4. The measured and simulated reflection coefficients $|S_{11}|$ of the proposed antenna.

$$\text{Fitness} = \sum (|S_{11}(f)| - |S_{11,d}(f)|) \left[\frac{1 + \text{sgn}(|S_{11}(f)| - |S_{11,d}(f)|)}{2} \right] \Delta f,$$

$$|S_{11,d}(f)| = -12 \text{ dB}, \text{ for } 2.8 \text{ GHz} \leq f \leq 11.0 \text{ GHz}. \quad (1)$$

Where, the Δf is frequency interval set to 0.01 GHz. The $|S_{11,d}|$ is the desired reflection coefficient, which is stricter than that of the UWB

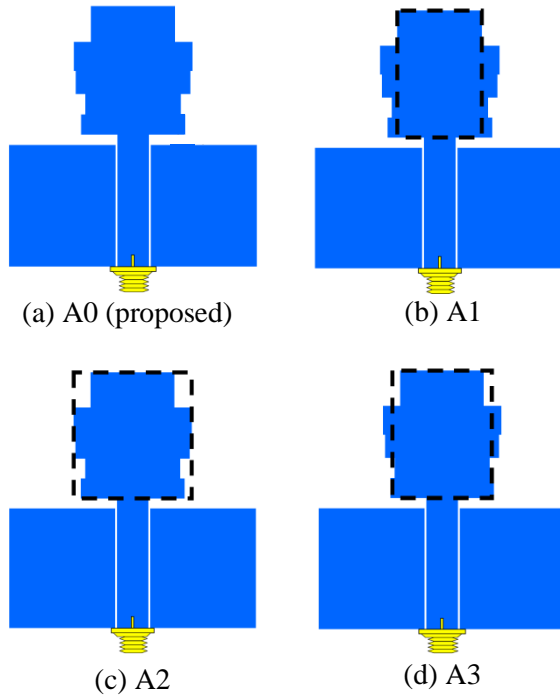


Fig. 5. The geometry of four different widths on the radiator of the UWB antennas.

specification. The fitness is the different area between $|S_{11}|$ and $|S_{11,d}|$ that should be as small as possible during optimization. The smaller the fitness is, the better optimization result obtained. The PSO optimization process is terminated when the maximum number of iterations is reached or when the fitness goes to zero. In the PSO setting, the maximum number iteration is set to 100. The reflecting boundary condition [13] and 27 particles and are used.

III. RESULTS AND DISCUSSIONS

The PSO optimization process is ended after the maximum number of iterations, 100, is reached. Figure 2 shows the curve of the best fitness versus iteration. The fitness value is dropped significantly during the first ten iterations. Then, the fitness slowly decreases as the number of iteration increases. The optimized dimensions of the global best are used to fabricate the proposed UWB antenna. Table 2 lists the optimized dimensions of the proposed antenna. Figure 3 reveals the picture of the antenna fabricated on an FR4 substrate with the antenna size of 34.0 mm by 33.35 mm. The measured

$|S_{11}|$ is obtained using an Agilent N5230A vector network analyzer (VNA). Figure 4 shows the curves of measured and simulated $|S_{11}|$. A reasonable agreement between them is observed. The impedance bandwidth of the simulated $|S_{11}|$ is 8.04 GHz (2.94 - 10.98 GHz below -10 dB).

To compare the performance of the proposed antenna with that of the UWB antenna with a uniform shape of the radiator, a parametric study was performed in this study. The proposed antenna has five different widths, W_1 to W_5 , on its radiator as shown in Table 2. The proposed antenna is denoted A0 as shown in Fig. 5(a). The minimum value of W_1 to W_5 is W_5 (11.29 mm). The widths of the radiator are uniformed to W_5 , and the antenna is denoted as A1, which can be seen in Fig. 5(b). The lengths, L_1 to L_5 , are fixed as those of A0. The other two antennas, A2 and A3, can be done by the similar way. The antenna, A2, has a uniform width W_4 (16.0 mm, the maximum value of W_1 to W_5) of its radiator as shown in Fig. 5(c). The antenna, A3, has a uniform width (13.91 mm, the mean of W_1 to W_5) of its radiator as shown in Fig. 5(d).

Figure 6 shows the simulated reflection coefficients $|S_{11}|$ of A0 to A3. Poor $|S_{11}|$ of A1 and A2 can be found. After comparing A0 to A3, the results show that the two curves are almost the same below 4.0 GHz; whereas, the $|S_{11}|$ of A0 is better than that of A3 in the frequencies between 4.0 GHz and 10.5 GHz. However, the A3 has a higher cut-off frequency (below -10 dB) at 11.28 GHz.

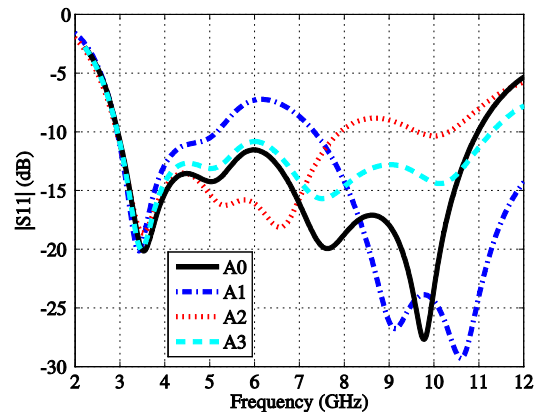


Fig. 6. The comparison of the antennas, A0 to A3, on simulated reflection coefficients $|S_{11}|$.

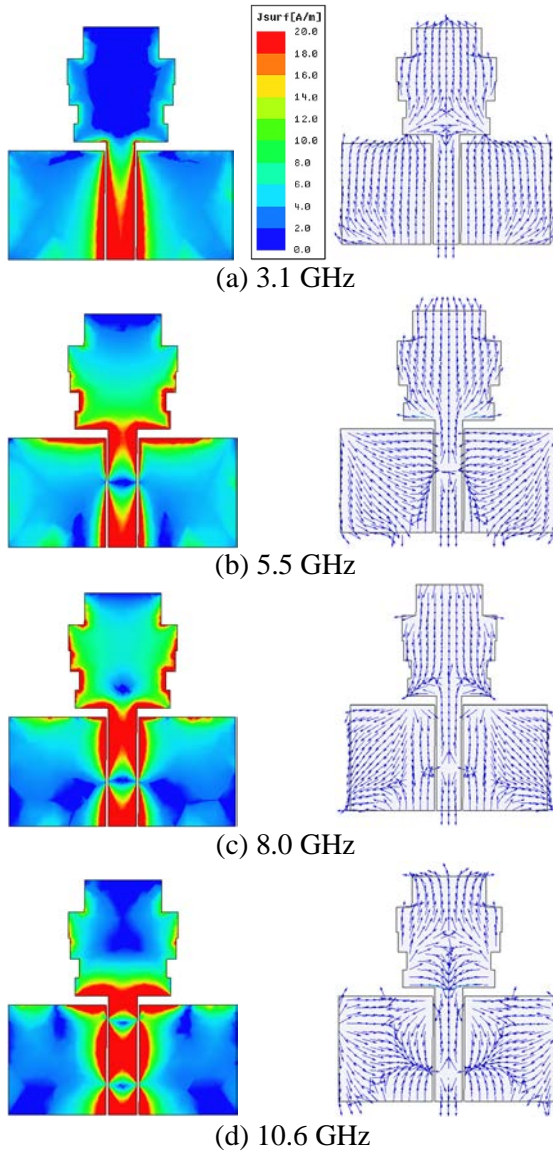


Fig. 7. The current distributions of the proposed UWB antennas at (a) 3.1 GHz, (b) 5.5 GHz, (c) 8.0 GHz, and (d) 10.6 GHz. The figures on the left-hand side and the right-hand side are magnitudes and directions, respectively.

Figure 7 shows the magnitudes and directions of current distributions of the proposed UWB antennas at 3.1, 5.5, 8.0, and 10.6 GHz, respectively. The current distributions are kept symmetrical about the z-axis at all frequencies. The current densities are much stronger near the edges of the ground plane and the radiator. The currents on the irregular edges of the radiator increase the path length of the currents. It makes the antenna size reduction. Moreover, the irregular

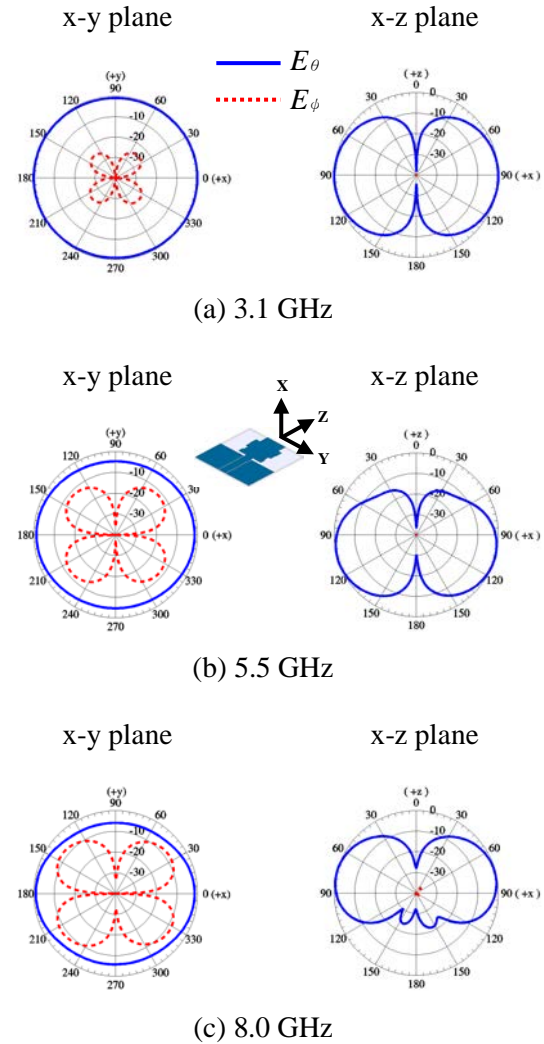


Fig. 8. Simulated radiation patterns (normalized) of the proposed antenna at (a) 3.1 GHz, (b) 5.5 GHz, and (c) 8.0 GHz.

edges affect the impedance matching especially at higher frequencies as the results also can be confirmed and shown in Fig. 6. Figure 8 shows normalized E_θ and E_ϕ in the x-y and x-z planes at frequencies of 3.1 GHz, 5.5 GHz, and 8.0 GHz. The E_θ is near omni-directional in the x-y plane at these three frequencies. The cross-polar component E_ϕ is very small (less than -40 dB) in the x-z plane. The results indicate that the proposed antenna is a good candidate for UWB applications. Figure 9 shows the measured maximum gain of the proposed antenna. The maximum gain increases as the frequency increases. The gain is 1.82 dBi at 3.0 GHz; whereas, the gain is 4.92 dBi at 11.0 GHz.

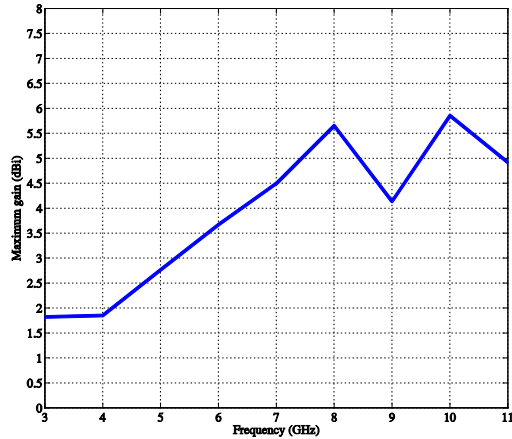
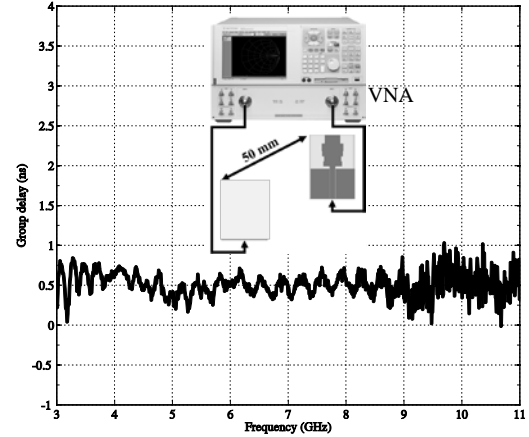


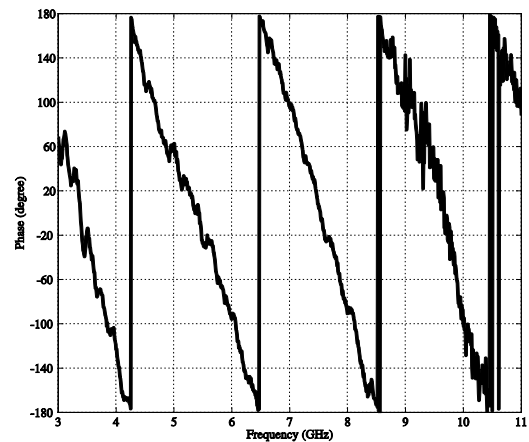
Fig. 9. The measured maximum gain of the proposed antenna.

To measure the dispersion and linearity of the proposed antenna, two identical proposed UWB antennas are placed in a face to face orientation (co-polarized direction) as shown in Fig. 10 (a). The two antennas are connected to port 1 and port 2 of the VNA (Agilent N5230A), respectively and fed by the low power 0 dBm coming from the two VNA ports. The two antennas are separated at a distance of 50 mm from each other. This short distance ensures a pure transmission relationship between two transmitted and received antennas. Other factors interfering with the transmission can be viewed as minor. Under this placement, the group delay was measured for the property of dispersion and measured the phase of the $|S_{21}|$ for the property of linearity. Figure 10 (a) shows the measured group delay of the proposed antenna. The variation of the group delay is less than 1 ns in the UWB spectrum. The result shows that a pulse distortion does not occur and a good linearity can be ensured in far-field region [7]. Figure 10 (b) shows the measured phase of $|S_{21}|$.

A good linearity of the $|S_{21}|$ phase is observed between 3.0 GHz and 8.5 GHz. If the frequencies are larger than 8.5 GHz, the variation of the $|S_{21}|$ phase becomes large. The loss becomes larger in the higher frequencies due to using a high loss FR4 substrate in this study such that the linearity of the $|S_{21}|$ phase becomes a little poor. However, the proposed UWB antenna still has good properties of dispersion and linearity in the band of interest.



(a)



(b)

Fig. 10. Measured results of the proposed antenna, (a) group delay and (b) $|S_{21}|$ phase.

VI. CONCLUSION

This study presents a planar ultra-wideband antenna with an irregular shape on its radiator for UWB applications. The particle swarm optimization combined with the finite element method based simulator, HFSS to design and optimize the proposed antenna. The antenna design process is automated and better results can be obtained efficiently. The proposed approach successfully obtains the desired goal. The antenna has a compact substrate size of 34.0 mm by 33.35 mm. Optimization results indicate that the proposed antenna has good characteristics of impedance bandwidth and radiation pattern in the band of interest. The parametric study of the proposed antenna shows that the optimized irregular shape of the proposed antenna

outperforms the antennas with uniform rectangular shapes in impedance matching in the UWB spectrum. The current distributions have been used to interpret the antenna characteristics. Measured results of the maximum gain, group delay, and phase of $|S_{21}|$ demonstrate good transmission properties of the proposed antenna. To sum up, the proposed antenna is suitable for UWB applications.

ACKNOWLEDGMENT

This work was supported by the National Science Council under Grants 100-2221-E-260-036 and 97-2218-E-260-003.

REFERENCES

- [1] Fed. Commun. Comm., Washington, DC, *First Report and Order, Revision of Part 15 of the Commission's Rule Regarding Ultra-Wideband Transmission System FCC 02-48*, Federal Communications Commission, 2002.
- [2] M. J. Ammann and Z. N. Chen, "Wideband Monopole Antennas for Multi-Band Wireless Systems," *IEEE Trans. Antennas Propagat. Mag.*, vol. 45, pp. 146-150, Apr. 2003.
- [3] W.-C. Weng, F. Yang, and A. Z. Elsherbeni, "Design of an Ultra-Wideband Antenna Using Taguchi's Optimization Method," *24th Annual Review of Progress in Applied Computational Electromagnetics*, Niagara Falls, Canada, pp. 304-309, April 2008.
- [4] J. Liang, C. C. Chiau, X. Chen, and C. G. Parini, "Printed Circular Disc Monopole Antenna for Ultra-Wideband Applications," *Electronics. Letter*, vol. 40, no. 20, September 2004.
- [5] H. Elsadek and D. M. Nashaat, "Multiband and UWB V-Shaped Antenna Configuration for Wireless Communications Applications," *IEEE Antennas and Wireless Propagation Letters*, vol. 7, pp. 89-91, 2008.
- [6] C. Y. D. Sim, W. T. Chung, and C. H. Lee, "Novel Band-notch UWB Antenna Design with Slit Ground Plane," *Microwave Opt. Technol. Lett.*, vol. 50, no. 8, pp. 2229-2233, August 2008.
- [7] Y. J. Cho, K. H. Kim, D. H. Choi, S. S. Lee, and S. O. Park, "A Miniature UWB Planar Monopole Antenna with 5-GHz Band-Rejection Filter and the Time-Domain Characteristics," *IEEE Trans. Antennas Propag.*, vol. 54, pp. 1453-1460, 2006.
- [8] V. A. Shameena, M. N. Suma, K. R. Rohith, P. C. Bybi, and P. Mohanan, "Compact Ultra-Wideband Planar Serrated Antenna with Notch Band ON/OFF Control," *Electron. Lett.*, 42, (23), pp. 1323-1324, 2006.
- [9] J. Kennedy and R. C. Eberhart, "Particle Swarm Optimization," in *Proc. IEEE Conf. Neural Networks IV, Piscataway, NJ*, 1995.
- [10] C. Huang, C. Chen, C. Chiu, and C. Li, "Reconstruction of the Buried Homogenous Dielectric Cylinder by FDTD and Asynchronous Particle Swarm Optimization," *Applied Computational Electromagnetic Society (ACES) Journal*, vol. 25, no. 8, pp. 672-681, 2010.
- [11] E. Di Giampaolo, F. Forni, and G. Marrocco, "RFID-Network Planning by Particle Swarm Optimization," *Applied Computational Electromagnetic Society (ACES) Journal*, vol. 25, no. 3, pp. 263-272, 2010.
- [12] M. Farmahini-Farahani, R. Faraji-Dana, and M. Shahabadi, "Fast and Accurate Cascaded Particle Swarm Gradient Optimization Method for Solving 2-D Inverse Scattering Problems," *Applied Computational Electromagnetic Society (ACES) Journal*, vol. 24, no. 5, pp. 511-517, 2009.
- [13] J. Robinson and Y. Rahmat-Samii, "Particle Swarm Optimization in Electromagnetics," *IEEE Trans. Antennas Propag.*, vol. 52, no. 2, pp. 397-407, Feb. 2004.
- [14] C. P. Wen, "Coplanar Waveguide: A Surface Strip Transmission Line Suitable for Nonreciprocal Gyromagnetic Device Application," *IEEE Trans. Microwave Theory Tech.*, vol. 17, pp. 1087-1090, Dec. 1969.



Wei-Chung Weng received the B.S. degree in Electronic Engineering from the National Changhua University of Education, Changhua, Taiwan, in 1993, the M.S. degree in Electrical Engineering from I-Shou University, Kaohsiung, Taiwan, in 2001, and the Ph.D. degree in Electrical Engineering from The University of Mississippi, USA, in 2007. Since August 2008, he has been an Assistant Professor in the Department of Electrical Engineering, National Chi Nan University, Puli, Taiwan. From 2004 to 2007, he was a Graduate Research Assistant in the Department of Electrical Engineering, The University of Mississippi. From 1993 to 2004 and 2007 to 2008, he was a Teacher in the Department of Computer Science, Kaohsiung Vocational Technical School, Kaohsiung, Taiwan. His research interests include antennas and microwave circuits design, computational electromagnetics, electromagnetic compatibility, and optimization techniques in electromagnetics. He has

served many journals as a reviewer for several years. He is the coauthor of the book entitled *Electromagnetics and Antenna Optimization Using Taguchi's Method* (Morgan & Claypool, 2008). Dr. Weng is a member of the Applied Computational Electromagnetic Society, the IEEE Antennas and Propagation Society and the Microwave Theory and Techniques Society, and a member of the Institute of Antenna Engineers of Taiwan.

A Novel Harmonic Suppression Antenna with Both Compact Size and Wide Bandwidth

Zhi-Li Zhou, Li Li, Jing-Song Hong, and Bing-Zhong Wang

Institute of Applied Physics

University of Electronic Science and Technology, Chengdu, 610054, China

zhouzhili003@163.com, liliangirl@126.com, cemlab@uestc.edu.cn, bzwang@uestc.edu.cn

Abstract — A novel CPW-fed harmonic suppression antenna with both compact size and wide bandwidth is proposed and investigated in this paper. The second and third harmonic frequencies are suppressed effectively with square-shaped lattices inserted in the ground plane. Furthermore, by exploiting the Vivaldi-shaped structure and two simple rectangular slots, wide bandwidth (1.86GHz) ranging from 1.9GHz to 3.76GHz is also obtained with rather compact size of $10\text{mm} \times 10\text{mm}$, which is much smaller than that have ever been reported before. Eventually, the measured results confirmed the simulated dates.

Index Terms — Compact size, harmonic suppression, PBG, Vivaldi shaped structure, wide bandwidth.

I. INTRODUCTION

The harmonic suppressed antenna (HSA), due to its great advantages such as low cost, small size, and easy integration, has become more and more attractive for various applications, such as wireless communications and microwave power transmission (MPT) [1-4]. Usually, a harmonic suppression filter will be required in those systems to avoid the harmonic influence on the overall system performance. However, it is bulky, expensive and hard to be integrated in monolithic microwave integrated (MMIC) devices. To overcome these defects, HSAs have been widely investigated these years: shorting pin [5], tuning stub [6], defected ground plane structure (DGS) [7], photonic band gap (PBG) [8], and the electromagnetic band gap structure (EBG) [9] can

all suppress the harmonic effectively. Besides, considerable research efforts have been made towards the miniaturization and broadband of HSAs. In [10], by inserting symmetrical slots in the ground plane of an open-ended CPW-fed transmission line, fairly compact dimensions, $26\text{mm} \times 15\text{mm}$ in physical size, and $0.3\lambda_g \times 0.17\lambda_g$ (λ_g is the wavelength in the substrate at the resonant frequency) in electrical size was obtained. In [11], a broadband HSA, with a 10-dB impedance bandwidth spanning from 1.56 GHz to 2.88 GHz (1.32GHz), was achieved by exploiting PBG structures with cross-shaped lattices. However, the compact HSA suffers a quite narrow bandwidth of 200 MHz, and the broadband HSA is very limited by its rather big size of about $50\text{mm} \times 60\text{mm}$.

In this paper, a novel harmonic suppression antenna with both compact size and wide bandwidth is presented. To suppress harmonics, PBG structures with square-shaped lattices were exploited. On the other hand, by employing the Vivaldi-shaped structure and two rectangular slots, a rather compact and small dimensions, $10\text{mm} \times 10\text{mm}$ in physical size, and $0.1\lambda_g \times 0.1\lambda_g$ in electrical size, is achieved with a wide bandwidth of 1.86 GHz spanning from 1.9 GHz to 3.76 GHz. Eventually, the experiment results agree well with the simulated dates.

II. ANTENNA DESIGN

The existing planar microstrip antennas are mostly in symmetrical structures, especially the printed monopoles antennas [12-13]. For those symmetrical structures their half formats have all the necessary dimension features for the resonant

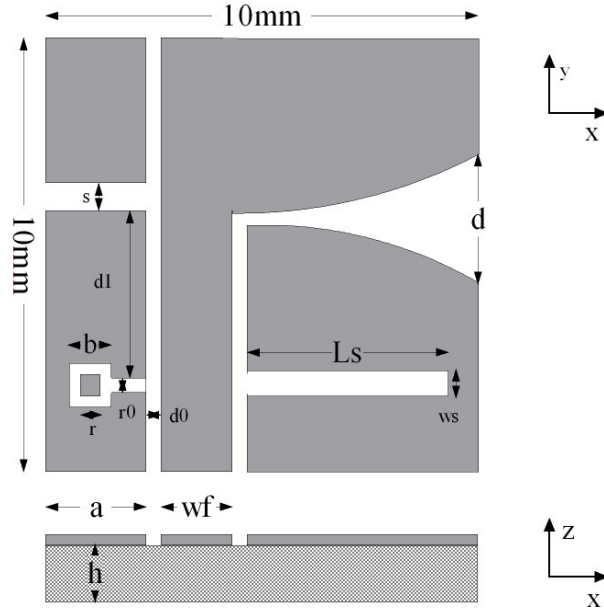


Fig. 1. Geometry of the proposed HSA.

frequencies. Therefore, it is expected that the miniaturized half structures of these symmetrical printed monopole antennas can achieve similar impedance features as the un-miniaturized full structures. Particularly, by simply exploiting its structural symmetry, 40% reduction in size was realized in [14]. Accordingly, similar but modified technology is applied to reduce the total size of the proposed harmonic suppression antenna at the beginning design, and then the PBG structure is used to suppress the harmonic frequencies.

Figure 1 shows the geometry of the proposed compact HSA with wide bandwidth. This antenna is printed on the RO4003C substrate with size of $10\text{mm} \times 10\text{mm}$, thickness of 0.5mm, and dielectric constant of 3.38. The width of the coplanar waveguide feeding line w_f is fixed at 1.6mm and the gap d_0 is fixed at 0.1mm to achieve 50Ω characteristic impedance.

Half structures of a Vivaldi-shaped printed monopole antenna, which is formed by the index gradient curve, are exploited at first. In order to further reduce the antenna size, a rectangular ground plane with a rectangular slot was added to the left side of the coplanar waveguide feeding line. Moreover, another rectangular slot was etched in the right ground plane. On the other hand, to suppress the harmonic frequencies, PBG structures with square-shaped lattices were inserted only in the left ground plane. Particularly,

the two rectangular slots, which can control the strength of coupling and guide the current distribution, are critical to the design and need to be carefully adjusted. At last, a fairly compact size and harmonic suppression as well as wide bandwidth are obtained at the same time.

III. RESULTS AND DISCUSSION

The proposed harmonic suppression antenna with both compact size and wide bandwidth are constructed, and the numerical and experimental results are presented and discussed. The parameters of this proposed antenna are studied by changing one parameter at a time and fixing the others. To fully understand the behavior of the antenna's structure and to determine the optimum parameters, the antenna was analyzed using the business software CST. And the prototype of the proposed antenna with optimal design, i.e. $a=2\text{mm}$, $s=0.3\text{mm}$, $w_s=0.5\text{mm}$, $d=5\text{mm}$, $d_1=4.5\text{mm}$, $L_s=6\text{mm}$, $b=1\text{mm}$, $r_0=0.1\text{mm}$, $r=0.4\text{mm}$, is shown in Fig. 2.



Fig. 2. Prototype of the proposed HSA.

In order to minimize the physical size of the proposed antenna, a rectangular slot is introduced into the right ground plane to alter the input impedance characteristics. As illustrated in Fig. 3, the slot can effectively lengthen the equivalent electrical length and the resonant frequency goes lower when the length of the slot L_s increases gradually.

Figure 4 exhibits the effects of the PBG on the impedance matching in comparison to the same antenna without PBG and three cases with PBG. It is found that the PBG structure successfully

suppressed the second and third harmonic frequencies. Furthermore, an extra resonant frequency is excited, thus a much wider impedance bandwidth is obtained. Also, from the results shown in Fig. 4, it can be observed that the parameter b have only impact on the extra resonant frequency. As the parameter b decreases from 1.1mm to 0.9mm gradually, the second resonant frequency increases correspondingly, while the first resonant frequency almost remains still.

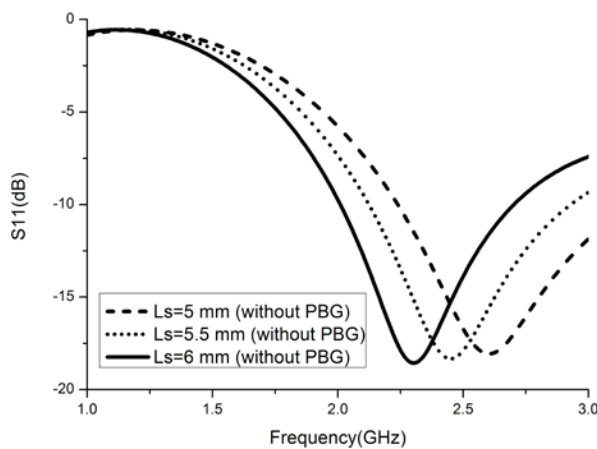


Fig. 3. Simulated S11 curves for the proposed antenna with different length of L_s .

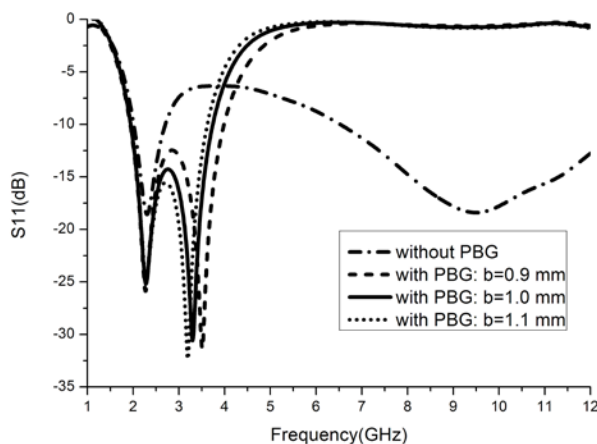


Fig. 4. Simulated S11 curves for the proposed antenna without PBG and with different PBG dimension of b .

Similarly, the S11 curves for various distance d_1 are plotted in Fig. 5. It can be observed that the parameter d_1 also mainly affects the second resonant frequency. And as d_1 increases from 3.5mm to 4.5mm, the second resonant frequency

shifts left. However, as shown in Fig. 6, the width w_s not only has impact on the second frequency but also the first one. The first resonant frequency decreases when the width w_s increases, while the second resonant frequency increases.

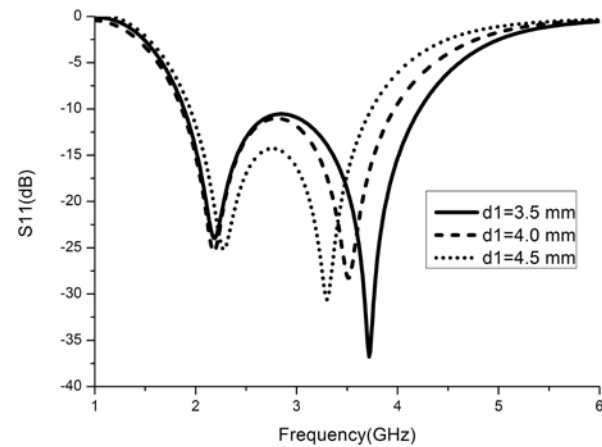


Fig. 5. Simulated S11 curves for various distance d_1 .

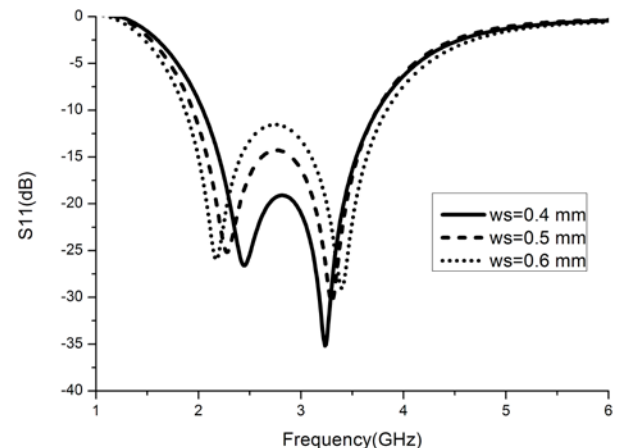


Fig. 6. Simulated S11 curves for various width w_s .

Eventually, the simulated and measured S11 of the proposed harmonic suppression antenna with optimized design are demonstrated in Fig. 7. Because FEKO is mostly used for large electrical size problems and the proposed antenna is very small, only CST, HFSS as well as IE3D were used to validate the results. Compared with the HFSS solver which is based on frequency domain, the transient solver of CST is based on time domain; thus, it is more suitable for wideband simulation cases. Therefore, the simulated results by the CST are quite similar to the measured results. Besides, the IE3D is based on the MOM algorithm, and it's

more suitable for planar structures. From the results in Fig. 7, it can be seen that the three results are similar and the -10dB impedance bandwidth of the proposed HSA is ranging from 1.9GHz to 3.76GHz, which is almost the maximum bandwidth since the lowest second harmonic frequency is 3.8GHz. The experiment results validate the design with only a slight shift. Furthermore, it is also noticed that the antenna is only 10mm × 10mm in physical size and $0.11 \lambda_g \times 0.11 \lambda_g$ in electrical size, which is much smaller than that have ever been reported before. Compared with the above mentioned compact HSA and the broadband HSA, this compact broadband harmonic suppression antenna proposed in this paper offers an even smaller size and broader bandwidth, e.g. about 76% and 96% reduction in size, 830% and 41% enhancement in bandwidth, respectively.

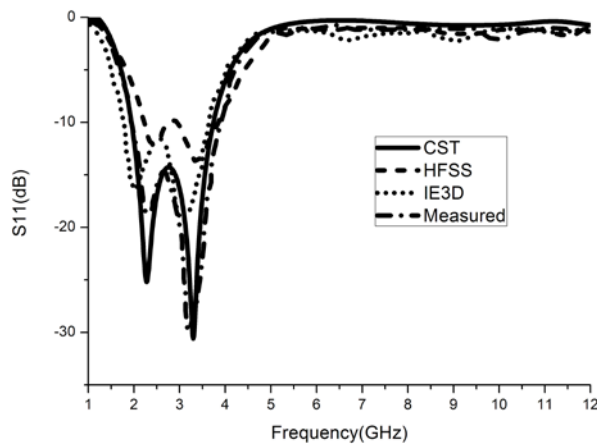


Fig. 7. The simulated and measured S11 for the proposed HSA with PBG structure.

Furthermore, as a very important aspect of a practical antenna, the efficiency of the proposed antenna is also investigated. The efficiency of the proposed HSA with PBG structure is shown in Fig. 8. And the efficiency of the reference antenna without the PBG structure is also shown for comparison. It can be observed that the reference antenna without the PBG structure is below 50% in the bandwidth since the total antenna size is rather small. Moreover, the suppression of the harmonics affects the antenna efficiency a lot. In the working band from 1.9GHz to 3.76GHz, the antenna efficiency almost remains the same. However, compared with the antenna without harmonics suppression, the antenna efficiency

with harmonics suppression goes much lower in the harmonics bands.

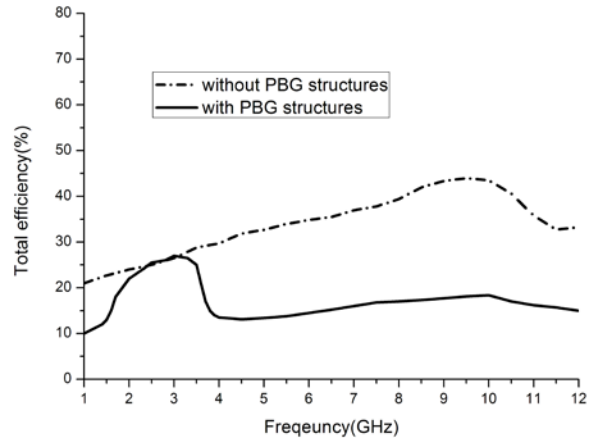


Fig. 8. The efficiency of the proposed HSA with PBG structure and the reference antenna without PBG structure.

Additionally, the radiation patterns of the proposed HSA with PBG structure and the reference antenna without PBG structure at 3GHz, 6GHz, and 9GHz are shown in Fig. 9 (a), (b), and (c), respectively. It illustrates that compared with the reference antenna, the proposed HSA could suppress the second and the third harmonics without deteriorating the fundamental radiation patterns.

IV. CONCLUSION

In this paper, a novel CPW-fed antenna with harmonic suppression is proposed and investigated. Both compact size and wide bandwidth are achieved by employing both the Vivaldi-shaped and PBG structures along with two simple rectangular slots. Particularly, it exhibits a smallest dimension up to now, 10mm × 10mm in physical size, and $0.11\lambda_g \times 0.11\lambda_g$ in electrical size, with a rather wide bandwidth spanning from 1.9 GHz to 3.76 GHz. With all these promising features, the proposed HSA is very attractive for wireless communication and microwave power transmission applications.

ACKNOWLEDGMENT

This work was supported by the National Natural Science Foundation of China (No. 61172115 and No. 60872029), the High-Tech Research and Development Program of China (No. 2008AA01Z206), the Aeronautics Foundation of

China (No. 20100180003), and the Fundamental Research Funds for the Central Universities (No. ZYGX 2009J037).

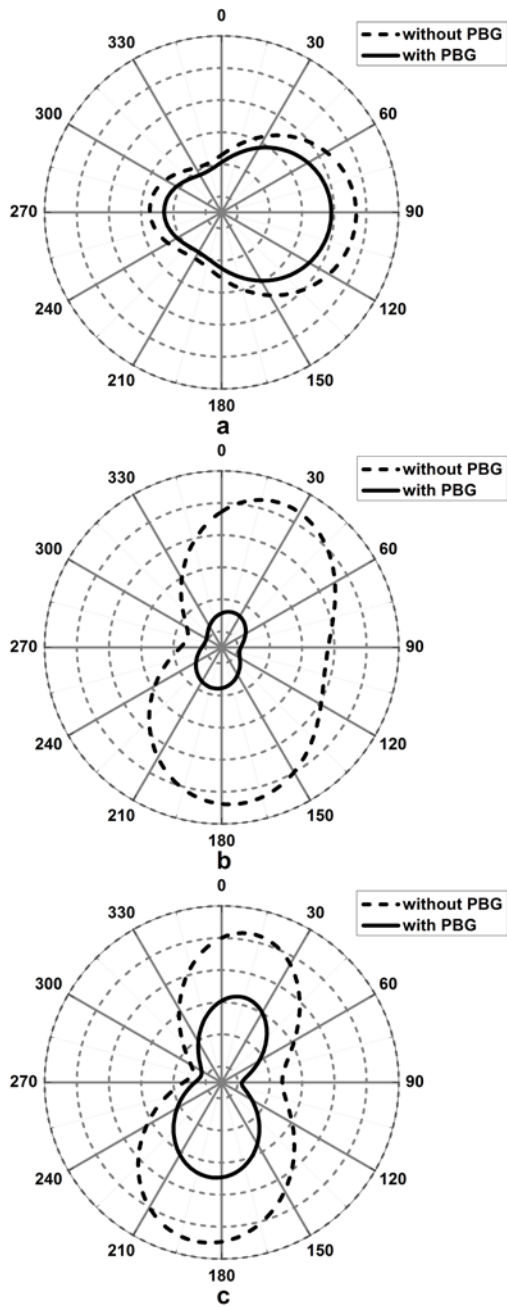


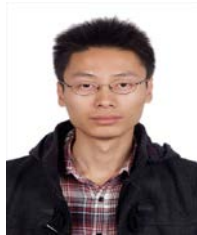
Fig. 9. The radiation patterns of the proposed HSA with PBG structure and the reference antenna without PBG structure at a) 3GHz, b) 6GHz, and c) 9GHz.

REFERENCES

- [1] H. Takhedmit, L. Cirio, B. Merabet, B. Allard, F. Costa, C. Vollaie, and O. Picon, "Efficient 2.45 GHz Rectenna Design Including Harmonic Rejecting Rectifier Device", *Electronics Letters*, vol. 10, pp.122-124, Jun. 2010.
- [2] R. Sujith, S. Mridula, P. Binu, D. Laila, and R. Dinesh, "Compact CPW-fed Ground Defected H-Shaped Slot Antenna with Harmonic Suppression and Stable Radiation Characteristics", *Electronics Letters*, vol.12, pp. 811-812, Jun. 2010.
- [3] D. Zayniyev and D. Budimir, "Dual-Band Microstrip Antenna Filter for Wireless Communications", *Antennas and Propagation Society International Symposium (APSURSI)*, vol. 2, pp. 1-4, Aug. 2010.
- [4] J.-Y. Park, Student Member, IEEE, S.-M. Han, Member, IEEE, and T. Itoh, Fellow, IEEE, "A Rectenna Design With Harmonic-Rejecting Circular-Sector Antenna", *IEEE Antennas and Propagation Letters*, vol. 3, pp. 52-54, Feb. 2004.
- [5] S. Kwon, H. K. Yoon, and Y. J. Yoon, "Harmonic Tuning Antennas Using Slots and Short-Pins", *IEEE Antennas and Propagation Society International Symposium*, vol. 1, pp. 117-118, July 2001.
- [6] F.-F. Hsiao, T.-W. Chiou, and K.-L. Wong, "Harmonic Control of a Square Microstrip Antenna Operated at the 1.8 GHz Band", *IEEE Proceedings of APMC2005*, Taipei, Taiwan, R.O.C., pp. 1052-1054, 2005.
- [7] F. Karshenas, A. R. Mallahzadeh, and J. Rashed-Mohassel, "Size Reduction and Harmonic Suppression of Parallel Coupled Line Bandpass Filter Using Defected Ground Structure", *Applied Computational Electromagnetic Society (ACES) Journal*, vol. 25, no. 2, pp.149-155, February 2010.
- [8] R. N. Baral and P. K. Singhal, "Design and Analysis of Microstrip Photonic Band Gap Filter for Suppression of Periodicity", *Applied Computational Electromagnetic Society (ACES) Journal*, vol. 25, no. 2, pp. 156-159, February 2010.
- [9] Y. R. Samii, "The Marvels of Electromagnetic Band Gap (EBG) Structures", *Applied Computational Electromagnetic Society (ACES) Journal*, vol. 18, no. 3, pp. 1-4, November 2003.
- [10] H. Kim and Y. J. Yoon, Member, IEEE, "Microstrip-Fed Slot Antennas with Suppressed Harmonics", *IEEE transactions on Antennas and Propagation*, vol. 53, no. 9, September 2005.
- [11] H. Kim and Y. J. Yoon, "A Novel Wideband Dual-Slot Antenna with Harmonic Suppression," in

Proc. IEEE Antennas Propagation Soc. Int. Symposium, vol. 4, pp. 3709–3712, Jun. 2004.

- [12] J. Liang, L. Guo, C. C. Chiau, and X. Chen, “CPW-Fed Circular Disc Monopole Antenna for UWB Applications,” *the Proc. IEEE Int. Workshop on Antenna Technology: Small Antennas and Novel Metamaterials, Singapore*, Mar. 7-9, 2005.
- [13] R. A. Sadeghzadeh-Sheikhan, M. Naser-Moghadasi, E. Ebadifallah, H. Rousta, M. Katouli, and B. S. Virdee, “Planar Monopole Antenna Employing Back-Plane Ladder-Shaped Resonant Structure for Ultra-Wideband Performance,” *IET Microwave. Antennas Propagation*, vol. 4, pp. 1327-1335, 2010.
- [14] M. Sun, Member, IEEE, Y. P. Zhang, Fellow, IEEE, and Y. Lu, Member, IEEE, “Miniaturization of Planar Monopole Antenna for Ultra Wideband Radios,” *IEEE Trans. Antennas and Propagation*, vol. 58, no. 7, pp. 2420-2425, July 2010.



Zhi-Li Zhou was born in Chongqing, China. He received his B.S. degree in Electronics Information and Engineering from Sichuan University, China, in 2009. He is now working toward his M.S. degree in Radio Physics from the University of Electronic Science and Technology of China (UESTC). His research interests include antennas for wireless communication and microwave power transmission.



Li Li was born in Meishan, China. She received her B.S. degree in Physics from Leshan Normal University in 2009. She is now a graduate student major in Radio Physics in University of Electronic Science and Technology of China (UESTC). Her interests include antenna technology and wireless communication technology.



Jing-Song Hong received the B.S. degree in Electromagnetic from Lanzhou University, China, in 1991, and the M.S. and Ph. D. degrees in Electrical Engineering from the University of Electronic Science and Technology of China (UESTC), in 2000 and 2005, respectively. He is now a professor with UESTC. His research interest includes the use of numerical techniques in electromagnetic and the use of microwave methods for materials characterization and processing.



Bing-Zhong Wang (M'06) received the Ph.D. degree in Electrical Engineering from the University of Electronic Science and Technology of China (UESTC), Chengdu, China, in 1988. In 1984, he joined UESTC, where he is currently a Professor. He has been a Visiting Scholar with the University of Wisconsin–Milwaukee, a Research Fellow with the City University of Hong Kong, and a Visiting Professor with the Electromagnetic Communication Laboratory, Pennsylvania State University, and University Park. His current research interests are in the areas of computational electromagnetic, antenna theory and techniques, electromagnetic compatibility analysis, and computer-aided design for passive microwave integrated circuits.

A Novel Circular Disc Monopole Antenna for Dual-Band WLAN Applications

Bing Li, Jing-song Hong, and Bing-Zhong Wang

Institute of Applied Physics
University of Electronic Science and Technology of China, Chengdu, 610054, China
libing0920@gmail.com

Abstract — This paper presents a novel and simple circular disc monopole antenna with a tunable H-shaped ground plane which provides two separate resonant modes to achieve 2.4- and 5.5-GHz dual-band operation for wireless local area network (WLAN) applications. The proposed antenna is printed on a low cost substrate FR4 ($\epsilon_r=4.4$) and excited using a 50Ω microstrip transmission line. Lower resonant mode of the antenna has an impedance bandwidth ($|S_{11}| < -10$ dB) of 700 MHz (2250-2950 MHz), and the upper resonant mode has a bandwidth of 1100 MHz (4900-6000 MHz). For validation purposes, an antenna prototype was fabricated and tested. The measured and simulated results show relatively good agreement and confirm satisfactory radiation characteristics. Effects of varying the widths of the arms of the H-shaped ground plane on antenna performance have also been studied.

Index Terms — Dual-band, H-shaped ground plane, monopole antenna, WLAN.

I. INTRODUCTION

During the recent years, there are rapid developments in wireless local area network (WLAN) applications. In order to satisfy the 2.45 GHz (2400-2483 MHz) band of IEEE 802.11b/g, 5.2 GHz (5150-5350 MHz), and 5.8 GHz (5725-5825 MHz) band of 802.11a WLAN standard, antennas with enhanced dual- or multi-frequency capabilities to meet the IEEE 802.11 WLAN standards in the 2.45/5.2/5.8 GHz operating bands, are in demand for practical WLAN applications. Printed monopole antennas are good candidates owing to their attractive features, e.g. simple

structures, low cost, low profile, light weight, omni-direction radiation patterns, easy realization, and convenience for integrating with microwave monolithic integrated circuit (MMIC) technologies.

Various kinds of printed monopole antennas, such as a microstrip fed printed double-T monopole antenna [1] and antennas with double L-slits [2], G-shaped radiating strip [3], semicircular and rectangular patch with H-shaped ground [4], and other antennas [5-9] have been reported to achieve dual band characteristics, which cover the 2.4- and 5.2- GHz WLAN bands. For the available designs, the antennas reported in [1, 4] can not achieve a dual-band response with sufficiently large bandwidth to cover the 2.45/5.5 GHz (2400–2483/ 5150–5825 MHz) bands. The antenna reported in [2] does not satisfy low-profile configurations. Other antennas mentioned in [3-9] are either large in antenna size or complex in antenna structure. Furthermore, the antennas in [10-12] require a shorting pin for the ground connection inside the printed monopole antenna element. This increases the design complexity as well as the fabrication cost. The antennas mentioned in [13, 14] provide a method to obtain broad bandwidth with a printed circular disc patch, but they are not suitable for WLAN applications. It noted that the longer strip controls the lower band of the antenna, while the shorter strip and the parasitic strip together generate the wide operating band for the upper resonance, so a popular method to obtain broad bandwidth is to use parasitic patches and short the parasitic or the monopole patches. As known, the antenna resonant frequencies depend on more parameters like slot

width, length etc, and thus the complexities of simulation, optimization, and fabrication for antenna increase by adding the parasitic patches.

Based on the background of the researches above, this paper proposes a novel microstrip-fed dual-band monopole antenna with simple structure, small size, and tuneable central frequency ratios. The proposed antenna is comprised of a circular disc patch and an H-shaped ground, it can be easily excited by a 50 Ω microstrip line. By tuning the widths of the arms of the ground plane, the central frequency ratios of the two operating frequencies can be adjusted. This means that the H-shaped ground plane can be a universal structure to design the dual-band printed monopole antenna which can satisfy different demands. Good impedance matching can be obtained for operating frequencies in the 2.45/5.2/5.8 GHz bands. The three-dimensional (3-D) EM simulator HFSS (based on the finite element method) is used. In this paper, 50 Ω wave port, ideal radiation boundary, solution frequency of 2.45 and 5.5 GHz is adopted) is used for design simulation. Design details of the proposed antenna are described, and results of impedance bandwidth, the radiation characteristics and gains are given and discussed in this paper.

This paper is organized as follows. The proposed antenna structure is briefly described in Section II. The measured and simulated results are discussed in Section III. Finally, the implications and significance of this work are briefly discussed in Section IV.

II. THE PROPOSED ANTENNA STRUCTURE AND DESIGN

Shown in Fig. 1 (a) is the schematic of the proposed antenna. The antenna with a radius of R and a 50 Ω microstrip feed line are printed on the same side of the dielectric substrate (in this paper, the FR4 substrate of thickness 1.6 mm and relative permittivity 4.4 was used as a lossless dielectric model). L and W denote the length and the width of the dielectric substrate, respectively. The width of the microstrip feed line is fixed at $W_1 = 3$ mm to achieve 50 Ω impedance. d is the distance of the feed gap between the feed point and the ground plane. On the other side of the substrate, the conducting H-shaped ground plane only covers the section of the microstrip feed line. Shown in Fig. 1

(b) is the return loss of antennas with different patches, the same H-shaped ground plane and the same dielectric substrate. The bandwidth of antenna with circular disc patch is larger and better than that with rectangular patch. The antenna still produces dual-band with the different patches. As a result, a common method to obtain broad bandwidth is to use circular disc patch, and the major effect of the H-shaped ground plane is to make current paths of the two resonant frequencies different, and thus dual resonant modes are excited.

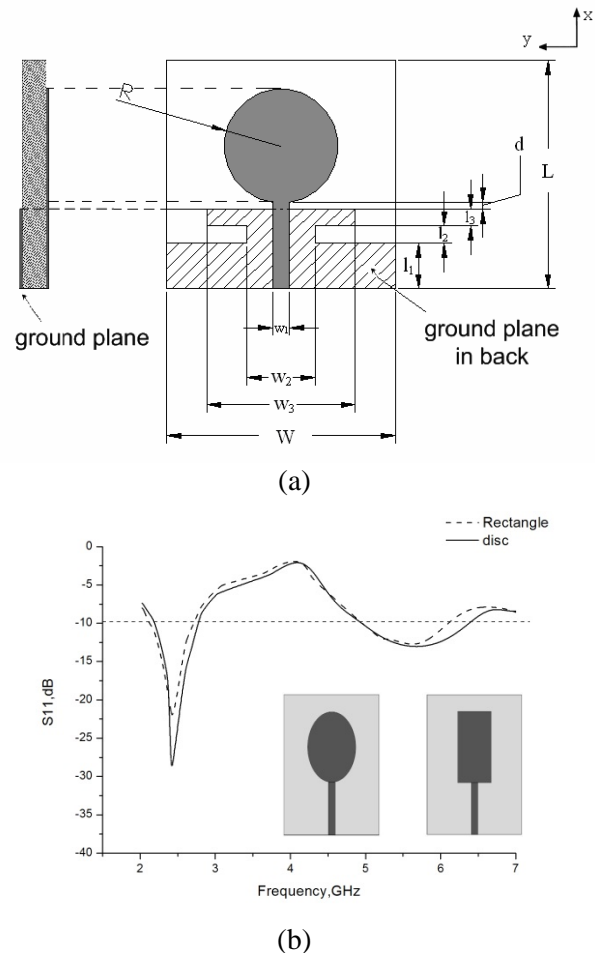


Fig. 1. (a) The configuration of the proposed monopole antenna. (b) The return loss of antennas with rectangular patch and circular disc patch.

In order to obtain the optimal size, the main parameters affecting the antenna bandwidth can be discussed in Fig. 2. The simulated results of three different lengths of $d=0.8, 1.1$ and 1.4 mm, $L_2=2, 3$ and 4 mm, $R_f=8, 10$ and 12 mm are presented in Fig. 2 (a), Fig. 2 (b), Fig. 2 (c), respectively, and

other dimensions of antenna are not changed. For the three cases in Fig. 2 (a), the upper band is narrow and not good enough when a larger or smaller d is selected, and the lower band is narrow when the smaller d is chosen. In Fig. 2 (b) and Fig. 2 (c) show that as the length of L_2 and R_1 increase, the upper band becomes larger and the lower band becomes smaller. As a result, the best size of antenna is presented in Table 1.

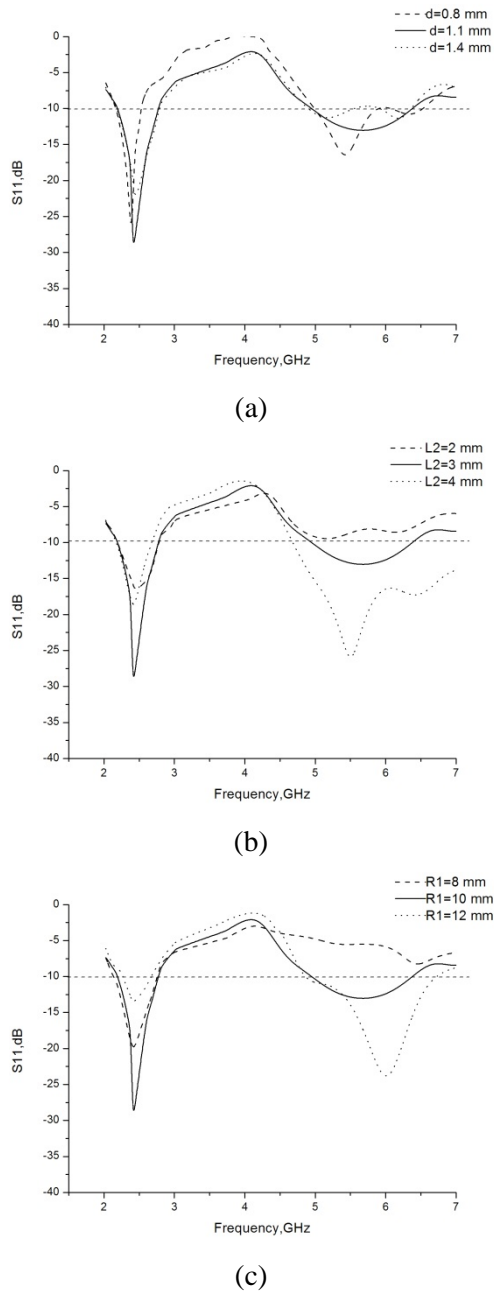


Fig. 2. Simulated reflection coefficient for antennas with various (a) d , (b) L_2 , (c) R_1 .

Table 1: Nominal design parameters of the proposed antenna

Design parameters	Value (mm)
R	10
L	40
l_1	8
l_2	3
l_3	3
d	1.1
W	40
W_1	3
W_2	12
W_3	26

II. RESULTS AND ANALYSIS

A. Radiation characteristic

To investigate the electromagnetic characteristics of the proposed antenna, the excited surface current distributions of the H-shaped ground at the two central resonant frequency 2.45 and 5.5 GHz are simulated, and the sketch is drawn in Fig. 3. It is shown that when the antenna is excited with the same phases and magnitudes, the excited surface current of the lower resonant mode of the antenna is strong in the larger arm of the H-shaped ground plane and weak in the upper arm of the H-shaped ground plane. On the contrary, the excited surface current of the higher resonant mode of the antenna is strong in the upper arm of the H-shaped ground plane and weak in the larger arm of the H-shaped ground plane, and thus the width (W_3) of the upper arm of the H-shaped ground plane controls the second or upper operating band, the width (W) of the larger arm of the H-shaped ground plane controls the first or lower operating band. WLAN bands can be achieved by adjusting the widths of the arms of the H-shaped ground.

To further validate the basic principle of the proposed antenna, a practical example illustrated in Fig. 4 is presented and examined using both simulations and prototype measurements. The dimensions of the antenna are given in Table 1.

The simulated and measured reflection coefficient (dB) of the dual-band antenna is shown in Fig. 5. It is clearly seen that two wide operating bandwidths are obtained, low-frequency bandwidth of the measurement is larger than that of the simulation and high-frequency bandwidth of

the measurement is equal to that of the simulation. The measured lower band achieves a -10 dB impedance bandwidth of 26.9%, ranging from 2.25 GHz to 2.95 GHz, with respecting to the central frequency at 2.6 GHz, and the measured bandwidth for the upper mode reaches 1.1 GHz (4.9–6.0 GHz), or about 20.2%, referred to the central frequency at 5.45 GHz. Obviously, the antenna can operate over the bands which cover the required bandwidths of the IEEE 802.11 WLAN standards in the band at 2.45 GHz (2400–2484 MHz), 5.2 GHz (5150–5350 MHz), and 5.8 GHz (5725–5825 MHz). Although there are some discrepancies between the simulated and measured results, which is probably due to the accuracy issues in making the prototype antenna as well as simulation or measurement errors and the stability of dielectric material, the agreement between the measured data and the simulated results is fairly good.

The simulated radiation patterns of the antenna at the central frequencies of the two WLAN bands are shown in Fig. 6 and Fig. 7, it is seen that the obtained radiation patterns are not as good as those of a conventional ideal monopole antenna, which has a good omni-directional pattern, they are more directional. For the E-plane (xz-plane), the radiation patterns of the proposed antenna are similar at 2.45/5.25/5.75 GHz. For the H-plane (yz-plane), the radiation pattern at 2.45 GHz can also be seen to be more directional than those at 5.25/5.75 GHz, the radiation pattern at 5.25/5.75 GHz has a good omni-direction.

Table 2 shows the antenna gains at lower operating band. In the 2.4 GHz band, the peak gain is 4.8 dBi at 2.8 GHz, 3.5 dBi at 2.4 GHz, and 1.4 dB of gain variation observed. Table 3 shows the antenna gain at upper operating band. In the 5.5 GHz band, the peak gain reaches 4.1 dBi at 6 GHz, 2.9 dBi at 5.2 GHz, and 4.0 dBi at 5.8 GHz, gain variation is less than 1.5 dB. Gain tends to be a constant in the whole band.

Table 2: Realized gain of lower operating band

Frequency (GHz)	2.2	2.4	2.6	2.8	3.0
Gain (dBi)	3.4	3.5	4.3	4.8	4.6

Table 3: Realized gain of upper operating band

Frequency (GHz)	4.9	5.2	5.5	5.8	6.0
Gain (dBi)	3.1	2.9	2.8	4.0	4.1

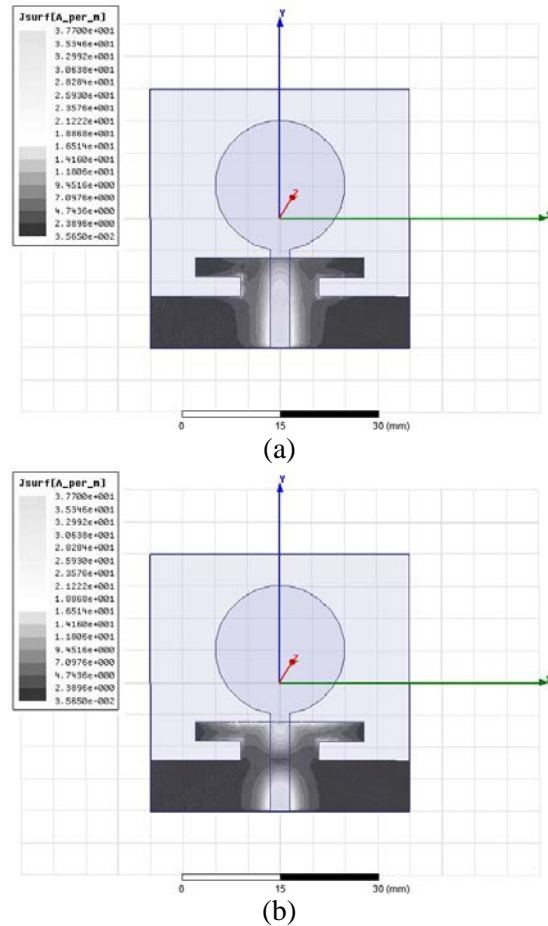


Fig. 3. Simulated surface current distributions of the H-shaped ground plane: (a) at 2.45 GHz, (b) at 5.5 GHz.

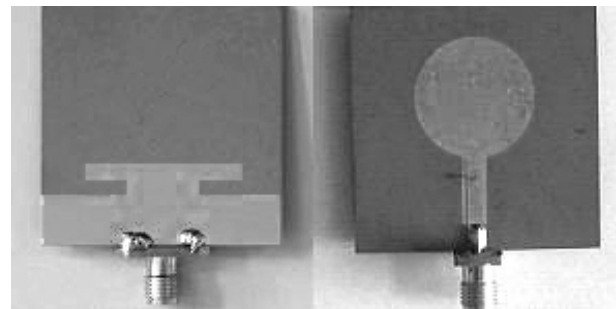


Fig. 4. The photo and configuration of the proposed monopole antenna.

Shown in Fig. 8 is the radiation efficiency for antenna, it can be seen that the radiation efficiency reaches more than 70% at lower operating band, and it is above 75% at upper operating band. In the non-operating band, the radiation efficiency for antenna is below 60%. In the whole band, the antenna obtains a good radiation characteristic.

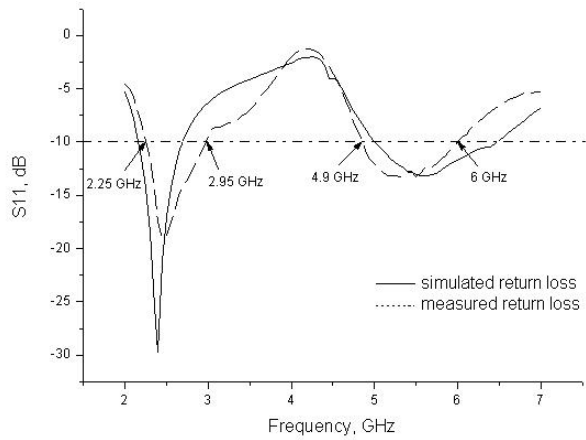


Fig. 5. Reflection coefficient of the antenna.

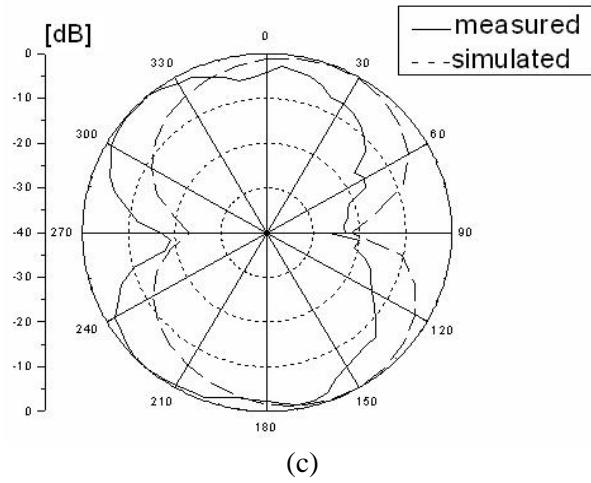
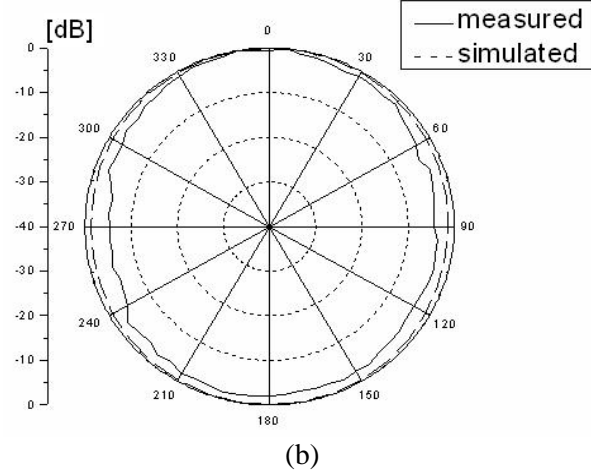
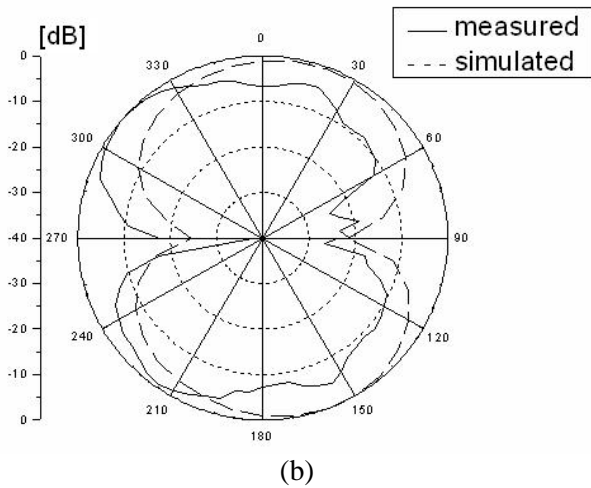
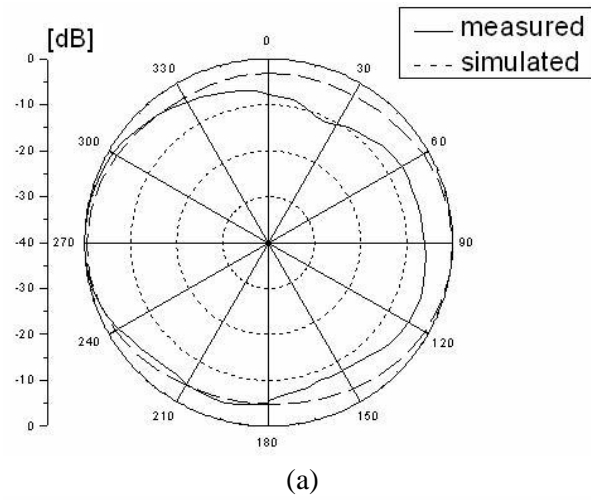
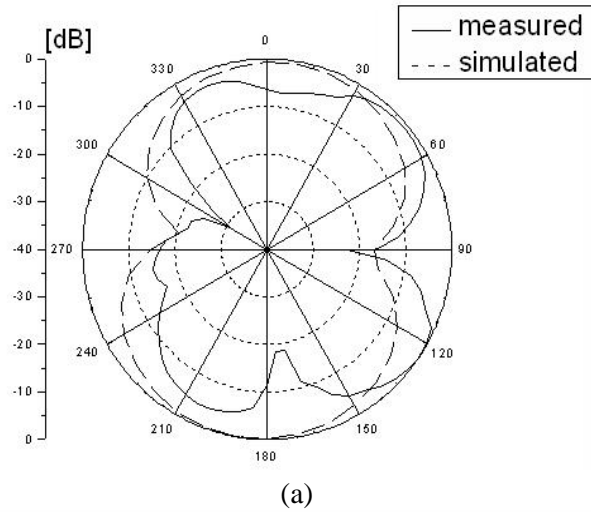


Fig. 6. E-plane radiation patterns of the proposed antenna. (a) 2.45 GHz, (b) 5.25 GHz, (c) 5.75 GHz.



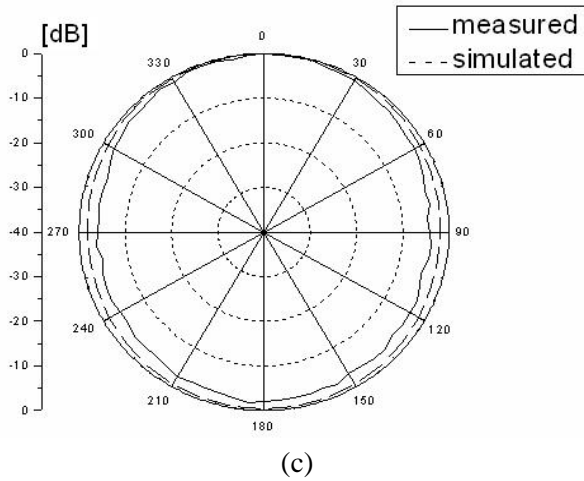


Fig. 7. H-plane radiation patterns of the proposed antenna. (a) 2.45 GHz, (b) 5.25 GHz, (c) 5.75 GHz.

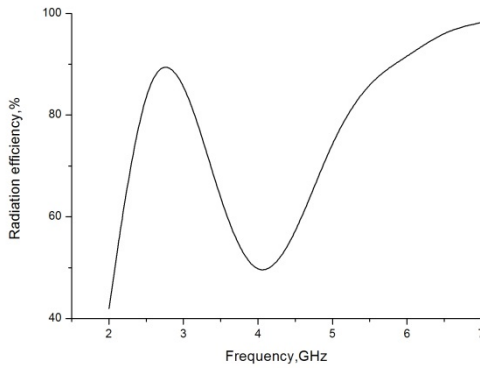


Fig. 8. Simulated radiation efficiency for antenna.

B. Effects of varying the widths of the arms of the ground plane

The parameters effect on the antenna’s resonant frequency and impedance bandwidth are studied.

Figure 9 shows that the central frequency of the higher resonant mode decreases with the increase of the width of the upper arm of the ground plane, while that of the lower resonant mode is nearly unchanged, and both of the impedance bandwidths are almost unchanged. Figure 10 shows that the central frequency of the lower resonant mode decreases with the increase of the width of the larger arm of the ground plane, while that of the higher resonant mode is nearly unchanged, and both of the impedance bandwidths are almost unchanged. This means that by varying the widths of the arms of the H-shaped ground plane, the central frequency ratio of the proposed

antenna can be adjusted. Making a compromise between size and bandwidths of the antenna, the final parameters are shown in Table 1.

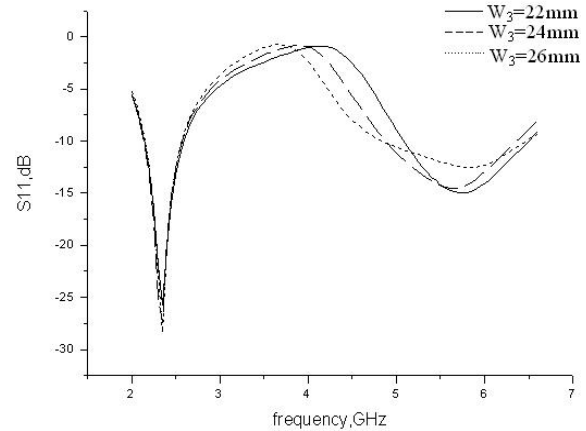


Fig. 9. Simulated reflection coefficient for antennas with various W_3 .

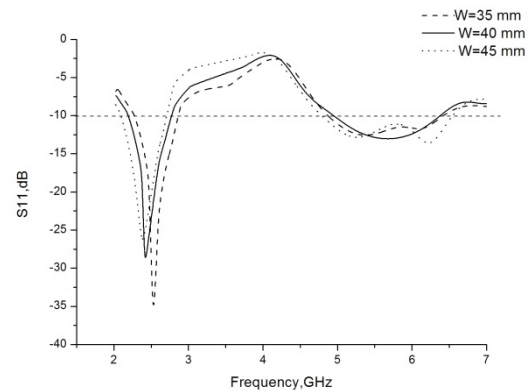


Fig. 10. Simulated reflection coefficient for antennas with various W .

As a result, one of the advantages of the proposed antenna is that it can meet the different bands for communication equipments by changing the widths of the arms of the H-shaped ground plane without changing other parameters.

IV. CONCLUSION

A novel dual-band monopole antenna excited by microstrip has been demonstrated in this paper. The proposed antenna has a simple structure. Moreover, by adjusting the widths of the arms of the H-shaped ground plane, the central frequency ratio of the antenna can be tuned so that the H-shaped ground plane can be used for designing the dual-band printed monopole antennas in order to satisfy different communication needs. After

optimizing the geometric parameters of the antenna, the proposed antenna can provide two discrete operating bands, which cover both 2.45 GHz (2.4-2.484 GHz) and 5 GHz (5.15-5.825 GHz) bands. The final measured results show satisfactory performance. Because the measured and simulated results are found to be in good agreement, the proposed antenna has been successfully designed for use in dual-band WLAN applications.

ACKNOWLEDGMENT

This work was supported by the National Natural Science Foundation of China (No. 60872029 and No. 60872034), the High-Tech Research and Development Program of China (No. 2008AA01Z206), the Aeronautics Foundation of China (No.20100180003), and the Fundamental Research Funds for the Central Universities (No. ZYGX 2009J037).

REFERENCES

- [1] Y. L. Kuo and K. L. Wong, "Printed Double-T Monopole Antenna for 2.4/5.2 GHz Dual-Band WLAN Operations," *Antennas and Propagation, IEEE Transactions on*, 51(9), pp. 2187-2192, 2003.
- [2] T. H. Kim and D. C. Park, "Compact Dual-Band Antenna with Double L-Slits for WLAN Operations," *Antennas and Wireless Propagation Letters, IEEE*, 4, pp. 249-252, 2005.
- [3] C. Y. Pan, C. H. Huang, and T. S. Horng, "A New Printed G - Shaped Monopole Antenna for Dual - Band WLAN Applications," *Microwave and Optical Technology Letters*, 45(4), pp. 295-297, 2005.
- [4] G. M. Zhang, et al., "A Novel Planar Monopole Antenna with an H-Shaped Ground Plane for Dual-Band WLAN Applications," *Journal of Electromagnetic Waves and Applications*, 21(15), pp. 2229-2239, 2007.
- [5] H. Wang and M. Zheng, "An Internal Triple Band WLAN Antenna," *Antennas and Wireless Propagation Letters, IEEE*, 48(5), pp. 829-835, 1999.
- [6] H. Liu, S. Lin, and C. Yang, "Compact Inverted-F Antenna with Meander Shorting Strip for Laptop Computer WLAN Applications," *Antennas and Wireless Propagation Letters, IEEE*, 10, pp. 540-543, 2011.
- [7] S. H. Yeh and K. L. Wong, "Dual-Band F-Shaped Monopole Antenna for 2.4/5.2 GHz WLAN Application," *IEEE Antennas and Propagation Society International Symposium*, 2002.
- [8] C. H. See, et al., "Dual-Frequency Planar Inverted FL-Antenna (PIFLA) for WLAN and Short Range Communication Systems," *Antennas and Propagation, IEEE Transactions on*, 56(10), pp. 3318-3320, 2008.
- [9] H. D. Chen, J. S. Chen, and Y. T. Cheng, "Modified Inverted-L Monopole Antenna for 2.4/5 Ghz Dual-Band Operations," *Electronics Letters*, 39(22), pp. 1567-1568, 2003.
- [10] Y. L. Kuo, T. W. Chiou, and K. L. Wong, "A Novel Dual - Band Printed Inverted - F Antenna," *Microwave and Optical Technology Letters*, 31(5), pp. 353-355, 2001.
- [11] J. Y. Jan and L. C. Tseng, "Planar Monopole Antennas for 2.4/5.2 Ghz Dual-Band Application," *IEEE Antennas and Propagation Society International Symposium*, 2003.
- [12] C. Y. Chiu, P. L. Teng, and K. L. Wong, "Shorted, Folded Planar Monopole Antenna for Dual-Band Mobile Phone," *Electronics Letters*, 39(18), pp. 1301-1302, 2003.
- [13] J. Liang, et al., "Study of a Printed Circular Disc Monopole Antenna for UWB Systems," *Antennas and Propagation, IEEE Transactions on*, 53(11), pp. 3500-3504, 2005.
- [14] S. Dey, N. Saha, and S. Biswas, "Design and Performance Analysis of UWB Circular Disc Monopole Textile Antenna and Bending Consequences," *IEEE*, pp. 1129-1133, 2011.



Bing Li is a graduate student majoring in Radio Physics in the University of Electronic Science and Technology of China now. Her research interests include antenna technology and wireless communication technique.



Jing-song Hong received the B.Sc. degree in Electromagnetics from Lanzhou University, China, in 1991, and the M.Sc. and Ph.D. degrees in Electrical Engineering from the University of Electronic Science and Technology of China (UESTC), in 2000 and 2005, respectively. He is now a professor with UESTC. From 1991 to 1993, he was a Circuit Designer with the Jingjiang Radar Factory, Chengdu, China. From 1993 to 1997, he was a Testing Engineer with SAE Magnetics (HK) Ltd, Guangdong, China. From 1999 to 2002, he was a Research Assistant with the City University of Hong Kong. His research interest includes the use of numerical techniques in electromagnetics and

the use of microwave methods for materials characterization and processing.



Bing-zhong Wang received the B.S.E.E., M.S.E.E., and Ph.D. degrees from the University of Electronic Science and Technology of China (UESTC), Chengdu, in 1982, 1984, and 1988, respectively, all in Electrical Engineering. He joined the

Institute of Applied Physics, UESTC, in 1984. From 1984 to 1988, he was a Research Assistant, and his research dealt with the millimeter-wave transmission lines and millimeter-wave integrated circuits. From 1988 to July 1990, he served as a Lecturer/Research Associate in the Institute of Applied Physics at UESTC, conducting researches in electromagnetic scattering. From August 1990 to January 1992, he was with the Department of Electrical Engineering, University of Wisconsin-Milwaukee, where he was a Visiting Scientist in the Signal Propagation Research Laboratory and engaged in research on the theoretical modeling of the electromagnetic behavior of high-speed integrated circuits. He returned to UESTC in 1992 as an Associate Professor and was promoted as a Full Professor in June 1995. From August 1996 to August 1997, he was a Visiting Research Fellow in the Department of Electronic Engineering at the City University of Hong Kong. From January 2000 to March 2000, he was a Visiting Professor in the Electromagnetic Communication Research Laboratory, Pennsylvania State University, and University Park. His current research interests are in the areas of computational electromagnetics, numerical modeling and simulation of the electromagnetic behavior in high speed integrated circuits and electronic packages, EMC analysis, electromagnetic modeling by artificial neural networks, computer aided design for passive microwave and millimeter wave integrated circuits, and antenna design.

Electric Field Distribution in a Biological Cell for Various Electrode Configurations-A Simulation Study

Md. Osman Goni

Department of Electronics and Communication Engineering
Khulna University of Engineering & Technology
osman_goni@yahoo.com

Abstract— Electroporation or electro-permeabilization (EP) is a non-viral physical process of inducing and/or increasing permeability of biological membranes by the application of high intensity and short duration electrical pulses. The resulting high field strength in the membrane can lead to the formation of regions of increased permeability, often called pores that allow transmembrane transport of macromolecules, such as DNA and chemo drugs. The efficacy of EP depends on a number of parameters, such as electric field strength, duration, number of pulses, size of target cell, and type of drug or DNA to be fed, to mention a few parameters. While electric field strength, duration, and number of pulses are the dominant parameters for the electroporation effect, the electric field distribution also depends on the shape, the size, and the material of electrodes used. The various electrodes used in practice are the parallel plate electrodes, the needle electrodes, the needle array electrodes, and the caliper electrodes. Both six needle array and parallel plate electrodes were used in the skin cancer trials. The electric field distribution varies with the type of electrode. The choice of electrodes depends upon the type of application. For example, parallel plate electrodes produce good results in human clinical trials and the distance between the electrodes can be easily varied. Needle electrodes are the simplest, but due to their configuration, the field distribution is highly nonlinear; there is higher field strength around the needle tip. That is one of the reasons for using multiple needles or needle arrays to make the field distribution as uniform as possible. It is of practical interest to study the electric field distribution of various electrodes to make a more informed choice of which electrodes to use. This

paper presents the results of a study of the electric field distribution in biological tissues for various electrode configurations. Magwel was used in this study. For the same voltage applied, the triangular and arc electrode configuration developed the highest electric field strength. Specifically, we develop simulation results that enhance or enable the acquisition of information from cells.

Index Terms— Cell culture, dielectrophoresis, electrodes, HeLa cell.

I. INTRODUCTION

Electroporation is the physical process of inducing transient permeability of biological membranes by short pulses of electric fields [1-3]. The resulting high field strength in the membrane can lead to the formation of areas of increased permeability, often called pores, which allow transmembrane transport of molecules. This effect has been used in the laboratory for more than a decade as a research tool to facilitate cellular uptake of genetic material in vitro. More recently, electroporation has also been found effective for the intracellular delivery of molecules in living tissues, which led to a variety of medical applications. Some of these applications have already proceeded to clinical trials. The effectiveness of this technique is evidenced by the Phase I and II skin cancer clinical trials [3]. The most important parameters for effective electroporation are the electrical field strength and the length of time the field applied (pulse length) [4, 5]. A number of other parameters can affect the efficacy of electroporation, such as the shape of the electrical pulse, polarity, number of and interval between pulses, size of target cells, and thermal conditions during and after the pulse, as

well as other cellular and environmental factors [4-7]. Electric field in the tissue is generated by a potential difference (voltage) between electrodes surrounding, or adjacent to, the tissue. A wide variety of electrode configurations have been developed, appropriate for each specific therapeutic goal [8, 9].

II. NEED FOR DIFFERENT CONFIGURATIONS OF ELECTRODES

The role of the electrodes is to act as a conduit to transform the voltage pulse from a pulse generator into local electric fields in tissues. The most commonly used electrodes are parallel plate electrodes [3, 8, and 9] and needle electrodes—either a six needle array [3, 8-10] or two needles [11] are used [12].

(a) Parallel plate electrodes. It's the simplest configuration and it produces good results in human clinical trials with tumors close to the surface due to the uniform electric field it develops [8]. With parallel plate electrodes, it is very easy to adjust the distance between them to obtain the desired field strength. However, plate electrodes are less efficacious for deeper tumors, where needle electrodes are more useful [8].

(b) Needle Electrodes. A pair of needles is also a very simple system [8, 11]. However, due to the needle configuration, the field of single-pair-needle electrodes is highly divergent, with high field strength near the needle tip. That is one of the reasons why multiple needles or needle arrays are needed to develop a more even electric field distribution [8]. Apparently, different cross sections of the electrodes will affect the electric field distribution. In this paper, the electric field distributions due to various electrode configurations are studied using Magwel [13].

III. ELECTRODES

To manipulate cells, one must create an electric field of a certain shape and strength. The two approaches to doing this are to either integrate electrodes within the microsystem or have them be external [14].

A. Internal electrodes

Internal electrodes, uncommon in EP systems, are the predominant approach to generating electric fields for dielectrophoresis (DEP), mainly

because of the superior control they offer for locally shaping the field. Electrodes act as equipotential surfaces that shape the field by controlling their location and voltage. Above, we saw that reducing the length of the electrodes favorably affected manipulation forces, and the simplest way to do this is to place electrodes close together. This necessitates electrodes that are internal to the system. The primary consideration that arises when using internal electrodes is that the electrodes can adversely interact with the electrolyte via either gas generation or corrosion. Because current is carried in metals by electrons and in electrolytes by ions, electrochemistry must occur at the electrode-electrolyte interface to transform the electron current into an ion current. The net result can be the production of gas (H_2 , O_2 , etc.) or dissolution of the electrode, both of which can disrupt operation of the device. This is a serious concern at dc, explaining the relative absence of EP systems that use internal electrodes. For DEP systems, electrochemical effects are typically avoided by operating at >10 's kHz in saline (lower frequencies can be tolerated in liquids of lower ionic strength). Gas generation is also voltage dependent, so higher voltages are more likely to lead to deleterious effects. Given that one usually wishes to operate at a high frequency (>100 's kHz) when using DEP with cells, electrochemistry does not pose any practical limitations.

B. External electrodes

The alternate approach is to use external electrodes. Very common in EP systems, external electrodes are rare in DEP systems. One advantage of using external electrodes is that they do not have to be fabricated with the device, resulting in a simpler fabrication process. The electrodes themselves often consist of platinum wires that are inserted into the port holes of the device. The electric field in systems that use external electrodes is shaped by using a straight channel (for EP) or inserting low polarizability obstructions (such as glass or polymer posts [15, 16]) in the channel (for DEP). There is no theoretical limit to the electric fields and forces that can be generated using external electrodes, although there are practical limits. Higher overall fields (such as for EP) are created by increasing the voltage or decreasing the spacing between the

obstructions, limited by the fact that openings cannot be made any smaller than the cells. Additionally, the fields exist throughout the volume of the electrolyte, which can lead to significant heating. Thus, published DEP devices for use with cells have typically used very-low conductivity water to minimize heating [15, 16]. Finally, fairly large voltages (approx. 0.1~1 kV) are needed to generate the required fields, and thus, these devices are limited to dc or low-frequency operation. This is fine for EP, which operates at dc, but restricts DEP manipulations to only the low frequency region of the Clausius-Mossotti (CM) factor. The need to minimize solution conductivity, operate at or near dc, and minimize chamber volume make external electrodes best suited for use with robust cells—such as bacteria—that can tolerate being placed in low-conductivity buffers or as endpoint analysis on cells that are not needed for downstream use.

C. Effects of electric field on cell

Because electrical cell manipulation exposes cells to strong electric fields, one needs to know how these electric fields might affect cell physiology. Ideally, one would like to determine operating conditions that will not affect the cells and use those conditions to constrain the design. Of course, cells are poorly understood complex systems and thus it is impossible to know for certain that one is not perturbing the cell. However, all biological manipulations—cell culture, microscopy, flow cytometry, etc.—alter cell physiology. What is most important is to minimize known influences on cell phenotype and then use controls to account for unknown influences. The known influences of electric fields on cells can be split into the effects due to current flow, which causes heating, and direct interactions of the fields with the cell. We consider each of these in turn.

IV. SIMULATION MODEL

We chose the multiphysics model (conductive and dielectric media dc & electrostatics model) when using Magwel. The general model cell culture system with the HeLa cell is shown in Fig. 1. Tables 1 and 2 give the dimensions and other electrical data used in this simulation, respectively.

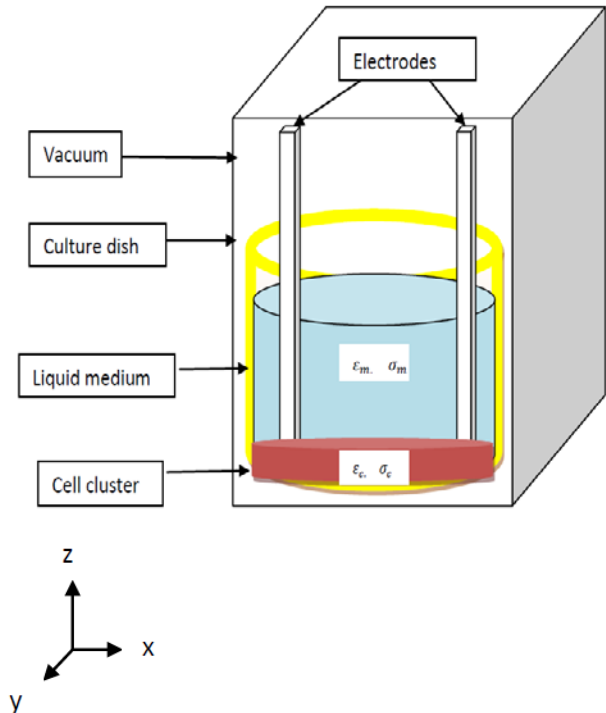


Fig. 1. 3D view of the simulation domain for the cell culture system.

Modeling of cell and medium: Figure 1 shows the schematic view of the cell culture system in which the HeLa cell is considered as a monolayer of cells located at the bottom of the culture dish. The cell is modeled as a homogeneous sphere with a diameter of 35 μm and a thickness of 3 μm . On the other hand, the culture medium is modeled as DMEM with 5 mm of height. Both the cell and the medium have their corresponding electrical parameters at different frequencies as listed in Table 1. The copper electrodes are used to apply electric field into the culture dish and are modeled as internal electrodes. The dimension and shape of the electrodes influence the generation of the E field in the vicinity of the electrodes which in turn induces field in the cell.

Table 1: Simulation parameters

Simulation domain	50 mm X 50 mm X 15 mm
Culture dish	circular type flux, diameter= 35 mm, height= 9.5 mm
Cell culture medium	Dulbecco’s Modified Eagle Medium (DMEM), height=5mm
Cell	Circular, monolayer, diameter= 35 mm, height= 3 μm
Electrodes (internal)	Copper, height=15mm (with different shape)
Spacing between electrodes	1mm
Applied voltage	10 V at f= 100 kHz (small signal)

Table 2: Dielectric properties of the HeLa cell and culture medium [17, 18]

Frequency	Cell E	Cell σ	Medium ε	Medium σ
1Hz	6.0e4	0.0001	80	1.6
100Hz	5.5e4	0.0007	78	1.55
100kHz	5 e4	0.001	76	1.5
1MHz	1.5e4	0.06	74	1.5

A. Angular plate electrodes configuration

The copper electrodes are placed inclined (V-shaped) in the layer of cell and medium as shown in Fig. 2(a). The contact is facilitating the input bias to the electrodes. Here the left electrode has a 10 V dc while the right one is at ground state (0 V). A small signal is also considered to the analysis with ac with frequency of 100 kHz. The small gap (1 mm) is maintained between the lower parts making angular orientation. Figures 2(b), 2(c), and 2(d) show the results with potential distribution, E field distribution, and magnetic vector potential, respectively. The higher electric

field intensity region is clearly observed at the smallest gap between the electrodes.

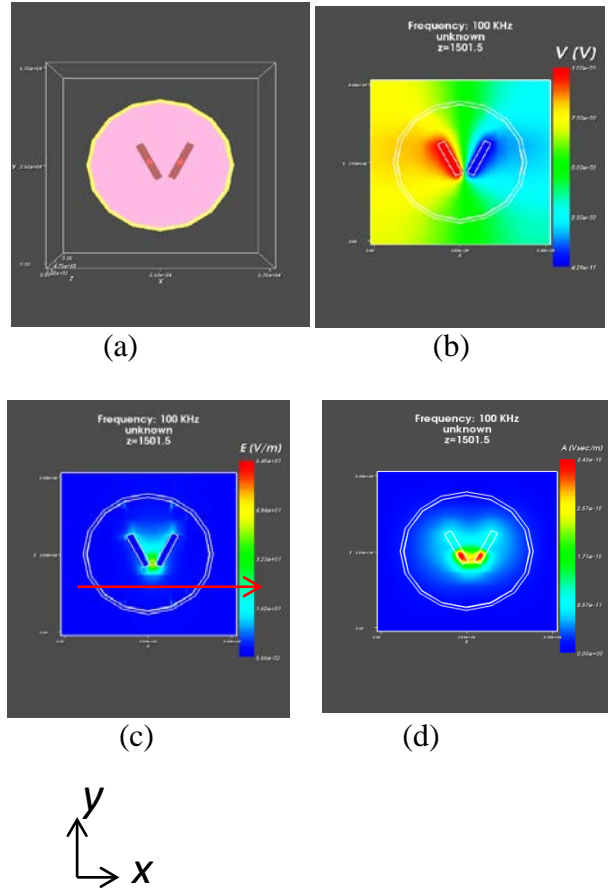


Fig. 2. Simulation model for the HeLa cell using inclined electrodes (x-y plane, at y= 21553 μm and z=1501 μm, at the position of cell layer marked with red arrow) (a) Cell layer view, (b) potential distribution, (c) spatial E field distribution, and (d) magnetic vector potential.

We have plotted the E field intensity in the x direction at y= 21553 μm and z=1501 μm (cell layer) as shown in Fig. 3. The sharp peak electric field strength at the gap of the electrodes is 64.5 V/m which is the actual field strength obtained in the center of the electrodes. The nominal field strength (voltage divided by the distance between the two electrodes) is 10 kV/m.

So, we can tell the actual field strength is much lower than the nominal value. This is true because field will be reduced inside the dielectric bodies as the cell having greater value of permittivity than the outside liquid medium. Two

other minor peaks are also observed at the both side of the main peak. Those are the interfacial field due to the conductor-dielectric interface.

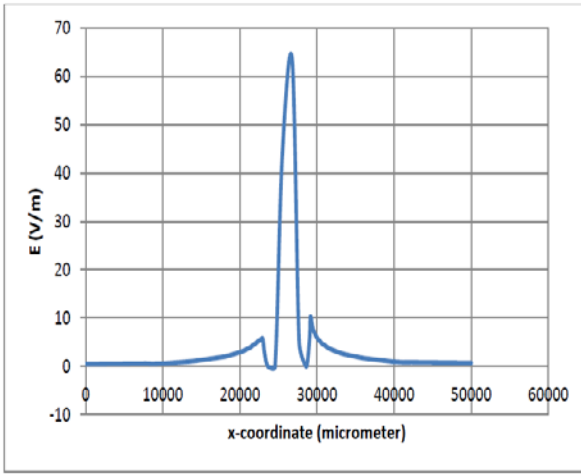


Fig. 3. E field variation along x axis at $y=21553 \mu\text{m}$ and $z=1501 \mu\text{m}$ at $f=100 \text{ kHz}$. $E_{\text{max}}=64.5 \text{ V/m}$ using inclined electrodes as shown in model of Fig 2(a).

B. Triangular electrodes configuration

This model is simulated using two triangular shape electrodes placed at the same gap in between the electrodes. The results of E field distribution are plotted with the function of x-coordinates (micrometer). Figure 5 shows the E field variation along the x axis at $y=26608 \mu\text{m}$ and $z=1501 \mu\text{m}$ at $f=100 \text{ kHz}$. The maximum electric field is found to be 105 V/m right at the gap of the electrodes. The sharp and pointed peak is found due to the symmetry in the discretization of electrodes.

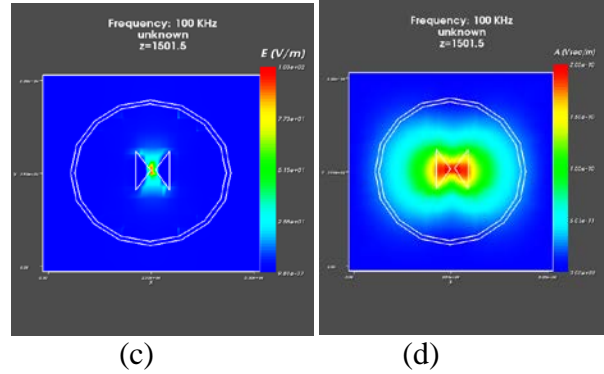
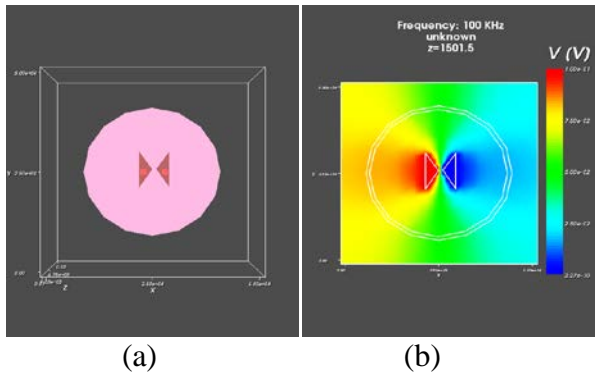


Fig. 4. Simulation model for the HeLa cell using triangular electrodes (a) cell layer view, (b) potential distribution, (c) spatial E field distribution, and (d) magnetic vector potential.

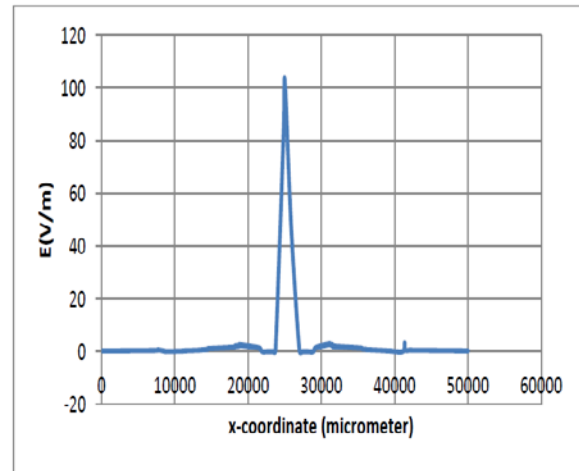


Fig. 5. E field variation along x axis at $y=26608 \mu\text{m}$ and $z=1501 \mu\text{m}$ at $f=100 \text{ kHz}$. $E_{\text{max}}=105 \text{ V/m}$ using inclined electrodes as shown in the model of Fig 4(a).

C. Needle electrodes configuration

The electric field distribution is not smooth near to the gap of electrodes as in Fig 6(a). Because the field is highly non-uniform due to the geometry of electrodes and no linear discretization effect at the electrodes edges that can be seen from Figs. 6(b), 6(c), and 6(d).

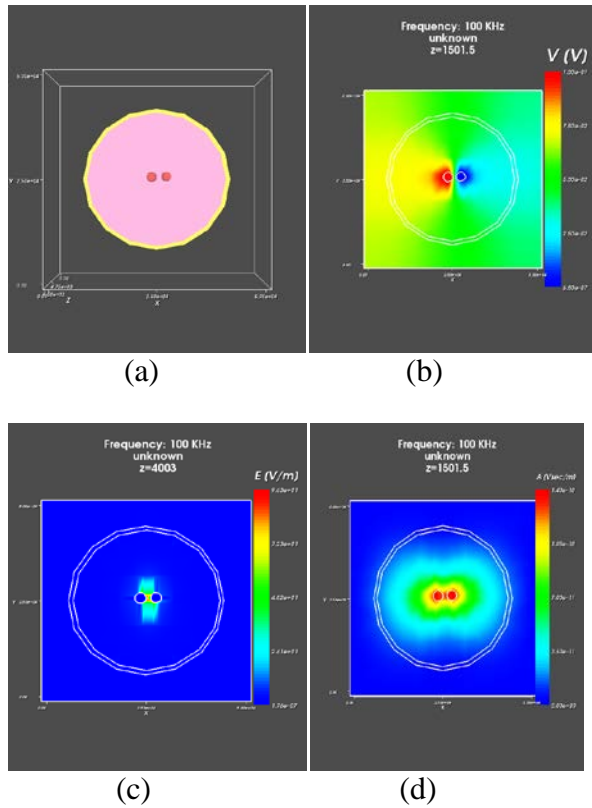


Fig. 6. Simulation model for the HeLa cell using needle electrodes (a) cell layer view, (b) potential distribution, (c) spatial E field distribution, and (d) magnetic vector potential.

Figure 7 shows the variation of E field along the x axis at $y=26045 \mu\text{m}$ and $z=1501 \mu\text{m}$ (cell layer) at $f=100 \text{ kHz}$. The maximum E field is observed to be 96 V/m . The neighboring effect of the conductive electrodes and conductor-dielectric interface would produce such an effect which can be noticed from a small rise-up at both sides of the main peak.

D. Parallel plate electrodes configuration

In this configuration model shown in Fig. 8(a) and the simulation results Figs 8(b), 8(c) and 8(d), the electric field distribution is found quite smooth and comparatively even at the entire gap of electrodes. Because the field is uniform due to the geometry of electrodes and also linear discretization is possible at the electrode edges. The high level electric field strength occurs between the cell and electrodes plates.

Figure 9 shows the variation of E field along x axis at $y=20400 \mu\text{m}$ and $z=1503 \mu\text{m}$ (cell layer) at $f=100 \text{ kHz}$. The maximum E field is observed to

be 96 V/m . The neighboring effect of the conductive electrodes and conductor-dielectric interface produce small rise-up at the both side of the main peak.

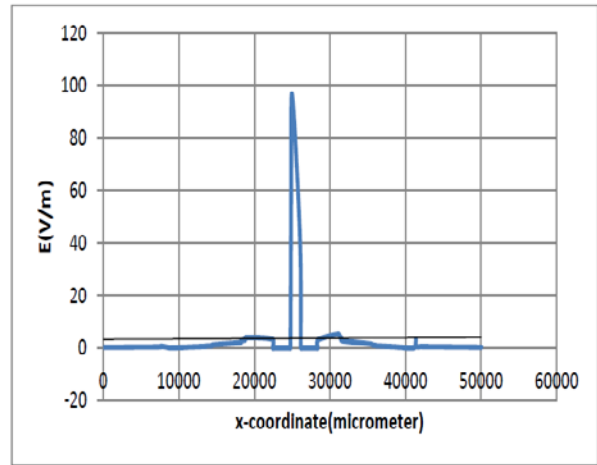


Fig. 7. E field variation along x axis at $y=26045 \mu\text{m}$ and $z=1501 \mu\text{m}$ at $f=100 \text{ kHz}$. $E_{\text{max}}=96 \text{ V/m}$ using needle electrodes as shown in model of Fig. 6(a).

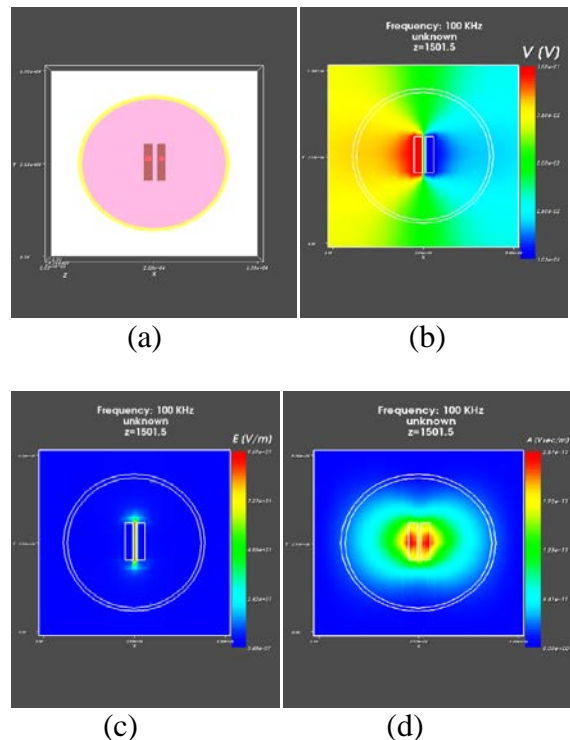


Fig. 8. Simulation model for the HeLa cell using parallel electrodes (a) Cell layer view, (b) potential distribution, (c) spatial E field distribution, and (d) magnetic vector potential.

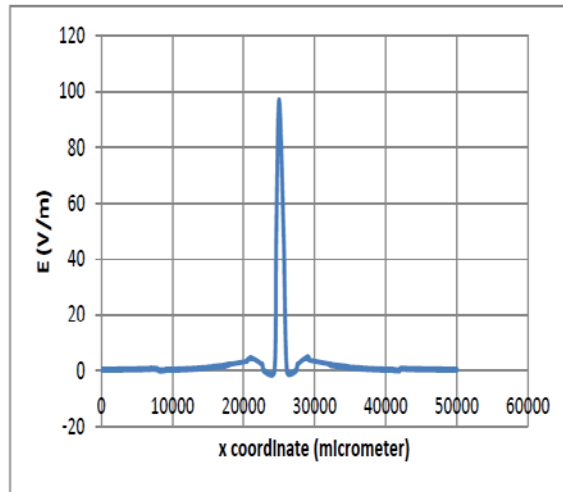


Fig. 9. E field variation along x axis at $y = 20400 \mu\text{m}$ and $z = 1503 \mu\text{m}$ at $f = 100 \text{ kHz}$. $E_{\text{max}} = 96 \text{ V/m}$ using parallel electrodes as shown in model of Fig 8(a).

E. Arc electrodes configuration

The non-smooth electric field distribution is found at the entire gap of electrodes shown in model and their results in Figs. 10(a) and 10(b). Because the field is non-uniform due to the geometry of electrodes and linear discretization is difficult to achieve at the electrodes edges. Figure 11 shows the variation of E field along x axis at $y = 26181 \mu\text{m}$ and $z = 1501 \mu\text{m}$ (cell layer) at $f = 100 \text{ kHz}$. The maximum E field is observed to be 134 V/m .

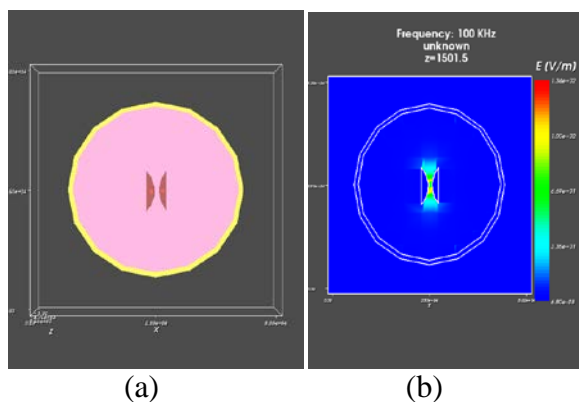


Fig. 10. Simulation model for the HeLa cell using inclined electrodes (a) cell layer view, (b) spatial E field distribution.

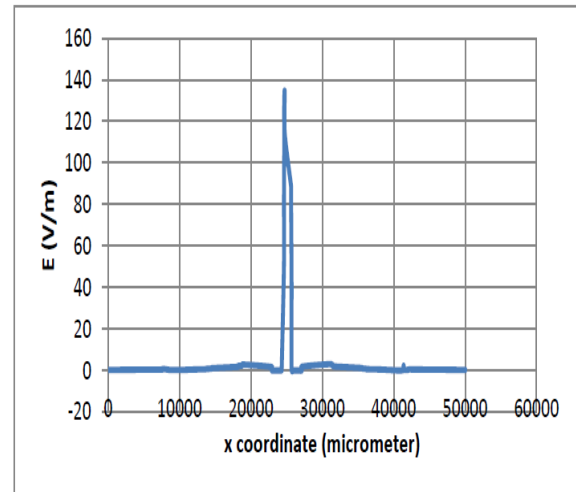


Fig. 11. E field variation along x axis at $y = 26181 \mu\text{m}$ and $z = 1501 \mu\text{m}$ at $f = 100 \text{ kHz}$. $E_{\text{max}} = 134 \text{ V/m}$.

Table 3 summarizes the results of the simulation of the HeLa cell model using different type and shape of the electrodes. The shape of the electrodes characterizes the linearity of the field distribution at the edges. The highest electric field strength due to highly non-uniformity occurs at the area closest to the sharp point. Domain discretization at the structure of interest is also important for the accurate results. The peak electric field exists only at the spacing (gap) of the electrodes. Hence, the location, shape, and orientation of the electrodes influence the overall contribution of the E field to the cell and medium. For the monolayer of the HeLa cell, the localized electric field as obtained from the above field distribution does not affect the entire layer of the cell. Thus, the average electric field should be more pronounced and effective for the polarization of the dielectric properties of the cell. In that case, the array of electrode could be a good choice where the uniform distribution is important. For the manipulation of small dielectric objects (cell), different types of array like interdigitated or polynomial electrodes array can also perform better than single electrode.

Table 3: Comparison of E fields with electrode's type and their orientations

Electrode's types and orientation	Maximum E field (V/m)	Uniformity
Flat and angular	64.5	Non uniform
Triangular	105	Non uniform
Rod (pin)	96	Non uniform
Flat and parallel	96	Uniform
Arc	134	Non uniform

V. CONCLUSION

The simulation of a monolayer of HeLa cell is presented here with the different types, shape, and orientation of electrodes. The electric field distribution for electroporation applications strongly depends on the electrode configurations. Parallel plate electrodes and needle electrodes of various dimensions are most commonly used for preclinical and clinical applications [3, 8-10]. Parallel plate electrodes give the most uniform electric field distribution with the simplest configuration as seen in this simulation and this correlates well with the published data [8]. Needle electrodes need to be used for deeply-seated tumors where parallel plate electrodes cannot be used. Due to the sharp needle point, needle electrodes give non-uniform field distribution with the highest field strength near the tip of the needle as the field homogeneity depends on the shape of the electrodes [19-21]. This point has to be taken into consideration during electroporation applications since the electric field in the tissue will be different for a given area and hence the efficacy of the technique will vary.

The cell and the medium are equivalently characterized by their electrical constants at certain frequency. As the medium is considered to be dispersive, the results are shown to be at certain frequency namely 100 kHz. It was found that up to 100 MHz, the results does not differ significantly as the size of the cell is much less than the wavelength (low frequency problem). The work also demonstrates the proper choice of the electrodes would be significant for the cell manipulation and cell culture.

The presented ideas facilitate the dielectrophoresis as a building block for lab-on-a-chip devices which can be easily fabricated using the existing microelectrode photolithography techniques. The design of the electrodes, the choice of the suspending medium, the applied peak voltage and frequency can be pre-determined to optimize the operation of the device.

REFERENCES

- [1] L. M. Mir, et al., Electrochemotherapy, "A Novel Antitumor Treatment: First Clinical Trial C. R.," *Acad. Sci.*, Paris 313, pp. 613-618, 1991.
- [2] R. H. Heller, "Overview of Electroporation," *Technology in Cancer Research & Treatment*, vol. 1, no. 5, 2002.
- [3] R. Heller, R. Gilbert, and M. J. Jaroszeski, "Clinical Trials for Solid Tumors using Electrochemotherapy," in *Electrochemotherapy, Electrogenotherapy, and Transdermal Delivery*, New Jersey: Humana Press, pp. 137-156, 2000.
- [4] M. P. Rols, et al., "In Vivo Delivery of Drugs and Other Molecules to Cell," in *Electrochemotherapy, Electrogenotherapy, and Transdermal Delivery*, New Jersey: Humana Press, pp. 83-97, 2000.
- [5] L. M. Mir and S. Orlowski, "The Basis of Electrochemotherapy," in *Electrochemotherapy, Electrogenotherapy, and Transdermal Delivery*, Humana Press, pp. 99-117, 2000.
- [6] H. Potter, "Molecular Genetic Applications of Electroporation," in *Electroporation and Electrofusion in Cell Biology*. New York: Plenum Press, pp. 319-341, 1989.
- [7] T. Curd, B. Vernon, C. Pauken, and R. Sundararajan, "Optimization of Electroporation Parameters for Human Ovarian Cancer Cells", *Proceedings of Electrostatics Society of America (ESA) Annual Meet*, University of Alberta, Edmonton, Canada 2005.
- [8] G. A. Hofmann, "Instrumentation and Electrodes for In Vivo Electroporation", in *Electrochemotherapy, Electrogenotherapy, and Transdermal Delivery*, New Jersey: Humana Press, pp. 37-61, 2000.
- [9] R. Gilbert, M. Jaroszeski, and R. Heller, "Novel Electrode Designs for Electrochemotherapy", *Biochimica et Biophysica Acta*, vol. 1334, pp. 9-14, 1997.
- [10] T. Goto et al., "Combination Electro-Gene Therapy Using Herpes Virus Thymidine Kinase and Interleukin-12 Expression Plasmids is Highly Efficient Against Murine Carcinomas In Vivo". *Mol. Therapy*, vol. 10, no. 5, p. 929-937 (2004).
- [11] Y. Yamashita et al., "Electroporation-Mediated Interleukin-12 Gene Therapy for Hepatocellular

- Carcinoma in the Mice Model”, *Cancer Res.*, vol. 61, pp. 1005-1012, 2001.
- [12] W. Mitchell and R. Sundararajan, “Electric Field Distribution in Biological Tissues for Various Electrode Configurations-A FEMLAB Study”, *Proc. of the COMSOL Multiphysics User’s Conf.*, Boston, 2005.
- [13] Magwel, SolvEM User Guide, Version 3.0.0, ©Magwel, <http://www.magwel.com/> Sep 2008.
- [14] Joel Voldman, “Electrical Forces for Microscale Cell Manipulation”, *Annu. Rev. Biomed. Eng.* 8: pp. 425-54, 2006.
- [15] C. F. Chou, J. O. Tegenfeldt, O. Bakajin, S. S. Chan, E. C. Cox, et al. “Electrodeless Dielectrophoresis of Single- and Double-Stranded DNA”, *Biophys. J.*, vol. 83, pp. 2170-79, 2002.
- [16] B. H. Lapizco-Encinas, B. A. Simmons, E. B. Cummings, Y. Fintschenko, “Dielectrophoretic Concentration and Separation of Live and Dead Bacteria in an Array of Insulators”, *Anal. Chem.* vol. 76, pp. 1571-79, 2004.
- [17] M. H. Wang, M. K. Chen, and L. S. Jang, “Electrical Characterization of Single HeLa Cell using 2D Simulation and Spectroscopy Measurement”, *IEEE proceedings*, CIBEC 2008.
- [18] Y. Nikawa and T. Michiyama, “Blood-Sugar Monitoring by Reflection of Millimeter Wave”, *Proceedings of Asia-Pacific Microwave Conf.* 2007.
- [19] J. Suehiro, G. B. Zhou, M. Imamura, and M. Hara, “Dielectrophoretic Filter for Separation and Recovery of Biological Cells in Water”, *IEEE Trans. Indus. Appl.*, vol. 39, pp. 1514-21, 2003.
- [20] Z. Z. Cvetkovic, B. Petkovic, M. Peric, “Systems for Homogeneous Electric Fields Generation and Effects of External Bodies on Field Homogeneity,” *Applied Computational Electromagnetic Society (ACES) Journal*, vol. 26, no. 1, pp. 56-63, Jan. 2011.
- [21] D. M. Velickovic and Z. Z. Cvetkovic, “Homogeneous Electric Field Generation using Biconical Electrodes”, *Proceedings 21st Int’l Conf. on Microelectronics*, vol. 1, pp. 209-212, Sep. 14-17, 1997.

2012 INSTITUTIONAL MEMBERS

DTIC-OCP LIBRARY
8725 John J. Kingman Rd, Ste 0944
Fort Belvoir, VA 22060-6218

AUSTRALIAN DEFENCE LIBRARY
Northcott Drive
Canberra, A.C.T. 2600 Australia

BEIJING BOOK CO, INC
701 E Linden Avenue
Linden, NJ 07036-2495

DARTMOUTH COLLEGE
6025 Baker/Berry Library
Hanover, NH 03755-3560

DSTO EDINBURGH
AU/33851-AP, PO Box 830470
Birmingham, AL 35283

SIMEON J. EARL – BAE SYSTEMS
W432A, Warton Aerodome
Preston, Lancs., UK PR4 1AX

ENGINEERING INFORMATION, INC
PO Box 543
Amsterdam, Netherlands 1000 Am

ETSE TELECOMUNICACION
Biblioteca, Campus Lagoas
Vigo, 36200 Spain

GA INSTITUTE OF TECHNOLOGY
EBS-Lib Mail code 0900
74 Cherry Street
Atlanta, GA 30332

TIMOTHY HOLZHEIMER
Raytheon
PO Box 1044
Rockwall, TX 75087

HRL LABS, RESEARCH LIBRARY
3011 Malibu Canyon
Malibu, CA 90265

IEE INSPEC
Michael Faraday House
6 Hills Way
Stevenage, Herts UK SG1 2AY

INSTITUTE FOR SCIENTIFIC INFO.
Publication Processing Dept.
3501 Market St.
Philadelphia, PA 19104-3302

LIBRARY – DRDC OTTAWA
3701 Carling Avenue
Ottawa, Ontario, Canada K1A OZ4

LIBRARY of CONGRESS
Reg. Of Copyrights
Attn: 407 Deposits
Washington DC, 20559

LINDA HALL LIBRARY
5109 Cherry Street
Kansas City, MO 64110-2498

MISSOURI S&T
400 W 14th Street
Rolla, MO 56409

MIT LINCOLN LABORATORY
Periodicals Library
244 Wood Street
Lexington, MA 02420

NATIONAL CHI NAN UNIVERSITY
Lily Journal & Book Co, Ltd
20920 Glenbrook Drive
Walnut, CA 91789-3809

JOHN NORGARD
UCCS
20340 Pine Shadow Drive
Colorado Springs, CO 80908

OSAMA MOHAMMED
Florida International University
10555 W Flagler Street
Miami, FL 33174

NAVAL POSTGRADUATE SCHOOL
Attn:J. Rozdal/411 Dyer Rd./ Rm 111
Monterey, CA 93943-5101

NDL KAGAKU
C/O KWE-ACCESS
PO Box 300613 (JFK A/P)
Jamaica, NY 11430-0613

OVIEDO LIBRARY
PO BOX 830679
Birmingham, AL 35283

DAVID PAULSEN
E3Compliance
1523 North Joe Wilson Road
Cedr Hill, TX 75104-1437

PENN STATE UNIVERSITY
126 Paterno Library
University Park, PA 16802-1808

DAVID J. PINION
1122 E Pike Street #1217
SEATTLE, WA 98122

KATHERINE SIAKAVARA
Gymnasiou 8
Thessaloniki, Greece 55236

SWETS INFORMATION SERVICES
160 Ninth Avenue, Suite A
Runnemedede, NJ 08078

YUTAKA TANGE
Maizuru Natl College of Technology
234 Shiroya
Maizuru, Kyoto, Japan 625-8511

TIB & UNIV. BIB. HANNOVER
DE/5100/G1/0001
Welfengarten 1B
Hannover, Germany 30167

UEKAE
PO Box 830470
Birmingham, AL 35283

UNIV OF CENTRAL FLORIDA
4000 Central Florida Boulevard
Orlando, FL 32816-8005

UNIVERSITY OF COLORADO
1720 Pleasant Street, 184 UCB
Boulder, CO 80309-0184

UNIVERSITY OF KANSAS –
WATSON
1425 Jayhawk Blvd 210S
Lawrence, KS 66045-7594

UNIVERSITY OF MISSISSIPPI
JD Williams Library
University, MS 38677-1848

UNIVERSITY LIBRARY/HKUST
Clear Water Bay Road
Kowloon, Honk Kong

CHUAN CHENG WANG
8F, No. 31, Lane 546
MingCheng 2nd Road, Zuoying Dist
Kaoshiung City, Taiwan 813

THOMAS WEILAND
TU Darmstadt
Schlossgartenstrasse 8
Darmstadt, Hessen, Germany 64289

STEVEN WEISS
US Army Research Lab
2800 Powder Mill Road
Adelphi, MD 20783

YOSHIHIDE YAMADA
NATIONAL DEFENSE ACADEMY
1-10-20 Hashirimizu
Yokosuka, Kanagawa,
Japan 239-8686

INFORMATION FOR AUTHORS

PUBLICATION CRITERIA

Each paper is required to manifest some relation to applied computational electromagnetics. **Papers may address general issues in applied computational electromagnetics, or they may focus on specific applications, techniques, codes, or computational issues.** While the following list is not exhaustive, each paper will generally relate to at least one of these areas:

- 1. Code validation.** This is done using internal checks or experimental, analytical or other computational data. Measured data of potential utility to code validation efforts will also be considered for publication.
- 2. Code performance analysis.** This usually involves identification of numerical accuracy or other limitations, solution convergence, numerical and physical modeling error, and parameter tradeoffs. However, it is also permissible to address issues such as ease-of-use, set-up time, run time, special outputs, or other special features.
- 3. Computational studies of basic physics.** This involves using a code, algorithm, or computational technique to simulate reality in such a way that better, or new physical insight or understanding, is achieved.
- 4. New computational techniques** or new applications for existing computational techniques or codes.
- 5. “Tricks of the trade”** in selecting and applying codes and techniques.
- 6. New codes, algorithms, code enhancement, and code fixes.** This category is self-explanatory, but includes significant changes to existing codes, such as applicability extensions, algorithm optimization, problem correction, limitation removal, or other performance improvement. **Note: Code (or algorithm) capability descriptions are not acceptable, unless they contain sufficient technical material to justify consideration.**
- 7. Code input/output issues.** This normally involves innovations in input (such as input geometry standardization, automatic mesh generation, or computer-aided design) or in output (whether it be tabular, graphical, statistical, Fourier-transformed, or otherwise signal-processed). Material dealing with input/output database management, output interpretation, or other input/output issues will also be considered for publication.
- 8. Computer hardware issues.** This is the category for analysis of hardware capabilities and limitations of various types of electromagnetics computational requirements. Vector and parallel computational techniques and implementation are of particular interest. Applications of interest include, but are not limited to,

antennas (and their electromagnetic environments), networks, static fields, radar cross section, inverse scattering, shielding, radiation hazards, biological effects, biomedical applications, electromagnetic pulse (EMP), electromagnetic interference (EMI), electromagnetic compatibility (EMC), power transmission, charge transport, dielectric, magnetic and nonlinear materials, microwave components, MEMS, RFID, and MMIC technologies, remote sensing and geometrical and physical optics, radar and communications systems, sensors, fiber optics, plasmas, particle accelerators, generators and motors, electromagnetic wave propagation, non-destructive evaluation, eddy currents, and inverse scattering.

Techniques of interest include but not limited to frequency-domain and time-domain techniques, integral equation and differential equation techniques, diffraction theories, physical and geometrical optics, method of moments, finite differences and finite element techniques, transmission line method, modal expansions, perturbation methods, and hybrid methods.

Where possible and appropriate, authors are required to provide statements of quantitative accuracy for measured and/or computed data. This issue is discussed in “Accuracy & Publication: Requiring, quantitative accuracy statements to accompany data,” by E. K. Miller, *ACES Newsletter*, Vol. 9, No. 3, pp. 23-29, 1994, ISBN 1056-9170.

SUBMITTAL PROCEDURE

All submissions should be uploaded to ACES server through ACES web site (<http://aces.ee.olemiss.edu>) by using the upload button, journal section. Only pdf files are accepted for submission. The file size should not be larger than 5MB, otherwise permission from the Editor-in-Chief should be obtained first. Automated acknowledgment of the electronic submission, after the upload process is successfully completed, will be sent to the corresponding author only. It is the responsibility of the corresponding author to keep the remaining authors, if applicable, informed. Email submission is not accepted and will not be processed.

EDITORIAL REVIEW

In order to ensure an appropriate level of quality control, papers are peer reviewed. They are reviewed both for technical correctness and for adherence to the listed guidelines regarding information content and format.

PAPER FORMAT

Only camera-ready electronic files are accepted for publication. The term **“camera-ready”** means that the material is neat, legible, reproducible, and in accordance with the final version format listed below.

The following requirements are in effect for the final version of an ACES Journal paper:

1. The paper title should not be placed on a separate page.

The title, author(s), abstract, and (space permitting) beginning of the paper itself should all be on the first page. The title, author(s), and author affiliations should be centered (center-justified) on the first page. The title should be of font size 16 and bolded, the author names should be of font size 12 and bolded, and the author affiliation should be of font size 12 (regular font, neither italic nor bolded).

2. An abstract is required. The abstract should be a brief summary of the work described in the paper. It should state the computer codes, computational techniques, and applications discussed in the paper (as applicable) and should otherwise be usable by technical abstracting and indexing services. The word "Abstract" has to be placed at the left margin of the paper, and should be bolded and italic. It also should be followed by a hyphen (–) with the main text of the abstract starting on the same line.
3. All section titles have to be centered and all the title letters should be written in caps. The section titles need to be numbered using roman numbering (I. II.)
4. Either British English or American English spellings may be used, provided that each word is spelled consistently throughout the paper.
5. Internal consistency of references format should be maintained. As a guideline for authors, we recommend that references be given using numerical numbering in the body of the paper (with numerical listing of all references at the end of the paper). The first letter of the authors' first name should be listed followed by a period, which in turn, followed by the authors' complete last name. Use a coma (,) to separate between the authors' names. Titles of papers or articles should be in quotation marks (" "), followed by the title of journal, which should be in italic font. The journal volume (vol.), issue number (no.), page numbering (pp.), month and year of publication should come after the journal title in the sequence listed here.
6. Internal consistency shall also be maintained for other elements of style, such as equation numbering. Equation numbers should be placed in parentheses at the right column margin. All symbols in any equation have to be defined before the equation appears or right immediately following the equation.
7. The use of SI units is strongly encouraged. English units may be used as secondary units (in parentheses).
8. Figures and tables should be formatted appropriately (centered within the column, side-by-side, etc.) on the page such that the presented data appears close to and after it is being referenced in the text. When including figures and tables, all care should be taken so that they will appear appropriately when printed in black and white. For better visibility of paper on computer screen, it is good to make color figures with different line styles for figures with multiple curves. Colors should also be tested to insure their ability to be distinguished after

black and white printing. Avoid the use of large symbols with curves in a figure. It is always better to use different line styles such as solid, dotted, dashed, etc.

9. A figure caption should be located directly beneath the corresponding figure, and should be fully justified.
10. The intent and meaning of all text must be clear. For authors who are not masters of the English language, the ACES Editorial Staff will provide assistance with grammar (subject to clarity of intent and meaning). However, this may delay the scheduled publication date.
11. Unused space should be minimized. Sections and subsections should not normally begin on a new page.

ACES reserves the right to edit any uploaded material, however, this is not generally done. It is the author(s) responsibility to provide acceptable camera-ready files in pdf and MSWord formats. Incompatible or incomplete files will not be processed for publication, and authors will be requested to re-upload a revised acceptable version.

COPYRIGHTS AND RELEASES

Each primary author must execute the online copyright form and obtain a release from his/her organization vesting the copyright with ACES. Both the author(s) and affiliated organization(s) are allowed to use the copyrighted material freely for their own private purposes.

Permission is granted to quote short passages and reproduce figures and tables from and ACES Journal issue provided the source is cited. Copies of ACES Journal articles may be made in accordance with usage permitted by Sections 107 or 108 of the U.S. Copyright Law. This consent does not extend to other kinds of copying, such as for general distribution, for advertising or promotional purposes, for creating new collective works, or for resale. The reproduction of multiple copies and the use of articles or extracts for commercial purposes require the consent of the author and specific permission from ACES. Institutional members are allowed to copy any ACES Journal issue for their internal distribution only.

PUBLICATION CHARGES

All authors are allowed for 8 printed pages per paper without charge. Mandatory page charges of \$75 a page apply to all pages in excess of 8 printed pages. Authors are entitled to one, free of charge, copy of the printed journal issue in which their paper was published. Additional reprints are available for \$ 50. Requests for additional re-prints should be submitted to the managing editor or ACES Secretary.

Corresponding author is required to complete the online form for the over page charge payment right after the initial acceptance of the paper is conveyed to the corresponding author by email.

ACES Journal is abstracted in INSPEC, in Engineering Index, DTIC, Science Citation Index Expanded, the Research Alert, and to Current Contents/Engineering, Computing & Technology.